Integrated Aeroacoustic Study of Owl-inspired Wings for Biomimetic Design of 'Silent' Flights

フクロウ規範翼の統合空力音響的研究と' 静かな' 飛行のバイオミメティックデザイン

February 2023

RONG JIAXIN

Graduate School of Science and Engineering

CHIBA UNIVERSITY

（千葉大学審査学位論文）

Integrated Aeroacoustic Study of Owl-inspired Wings for Biomimetic Design of 'Silent' Flights

フクロウ規範翼の統合空力音響的研究と' 静かな' 飛行のバイオミメティックデザイン

February 2023

RONG JIAXIN

Graduate School of Science and Engineering

CHIBA UNIVERSITY

Abstract

Owls can achieve silent flight, which is attributed to the unique owl-wing morphologies comprising leading-edge (LE) serrations, trailing-edge (TE) fringes, and a velvety upper wing surface. The innovative wings with owl-inspired morphologies (e.g., LE serrations, TE fringes) can provide biomimetic designs for low-noise fluid machinery. While the silent flight of owls has been a long-standing subject of interest, the aeroacoustic mechanisms associated with the unique wing morphologies are not yet well understood. This thesis describes an integrated aeroacoustic study of owl-inspired wings with LE serrations and TE fringes by loosely coupling the large-eddy simulations of unsteady near-field flow structures and the Ffowcs Williams-Hawkings equation for sound radiation. First, the aeroacoustic effects of TE fringes and their interplay with LE serrations are investigated. Using four owl-inspired wings with/without TE fringes and LE serrations, it is verified that TE fringes enable a pronounced high-frequency sound reduction at angles of attack of 5-15° while achieving comparable aerodynamic performance compared to the clean model, hence resolving the trade-off between aerodynamic force production and sound reduction. Furthermore, the combination of TE fringes and LE serrations produces a nonlinear synergetic effect that dramatically reduces far-field sound level, providing a powerful sound reduction tool for the biomimetic design of various fluid machinery. Second, the three-dimensional (3D) aeroacoustic characteristics induced by the TE fringes are examined. One clean wing model and three wing models with TE fringes that are distributed differently spanwise are employed. 3D simulations reveal that the TE fringes enable much more remarkable sound reduction spatially compared to the two-dimensional results. And the TE fringes distributed at midspan have better acoustic performance than those in the vicinity of the wingtip, indicating the importance of a spanwise distribution in enhancing aeroacoustic performance. Third, we studied the aeroacoustic effects of the LE serrations on feather-feather (feather slots) interactions. The aeroacoustic characteristics of tandem wing models with and without LE serrations are resolved. The results demonstrate that the aeroacoustic interaction between fore and hind wings inspired by feathers or

feather slots in owls' flight can be altered remarkably by owl-inspired LE serrations, which is closely associated with the gap distance between the fore and hind wings. The findings of this thesis contribute to the understanding of the silent owl flight mechanisms associated with the unique owl-wing morphologies comprising LE serrations and TE fringes, hence inspiring innovative wings for biomimetic design of 'silent' flights.

Key words: owl, aeroacoustics, biomimetic design, silent flight, leading-edge serrations, trailing-edge fringes

Acknowledgements

I would like to express my sincere gratitude to my supervisor, Prof. Hao Liu. This work could not have been accomplished without his guidance and encouragement.

I would also like to thank the other members of the laboratory. It was a memorable time working with them.

Finally, I am deeply grateful to my parents and sister for their understanding and unconditional support. Special thanks to my girlfriend for her companionship and encouragement during hard times.

This work was partly supported by a Grant-in-Aid for Scientific Research of KAKENHI, JSPS (Grant No. 19H00750). The author acknowledges financial support from the Japanese Government through a MEXT scholarship.

Table of Contents

1 Introduction

1.1 Motivation

Aerodynamic noise control has become an urgent issue for aviation and nautical industries. The noise aerodynamically generated by industrial products (e.g., aircrafts, drones, and propellers) has severely affected the daily life of human beings. As natural hunters, owls are famous for their silent flight. During flight, high-frequency sound ($f > 1$ kHz) is suppressed to an extremely low level [1-3], which is beneficial for capturing prey (e.g., mice and voles). The novel aeroacoustic mechanisms that result in the silent flight of an owl [4, 5] can certainly inspire innovative wings for the biomimetic design of 'silent' flights [6-9].

The silent owl flight is considered to be a consequence of the unique wing morphologies [10-14] comprising leading-edge (LE) serrations [9, 15-19], trailing-edge (TE) fringes [20, 21], and velvety upper wing surfaces [22, 23]. While the owl's silent flight has been a long-standing subject of interest, the aeroacoustic mechanisms of the three wing morphologies are not yet well understood and require more exploration [14].

In this work, we aim to unveil the aeroacoustic mechanisms associated with the unique wing morphologies during owl flight, hence inspiring innovative biomimetic wings for low-noise fluid machinery. The work is focused specifically on the aeroacoustic interaction between TE fringes and LE serrations, the three-dimensional aeroacoustic characteristics induced by TE fringes, and the effects of LE serrations on feather-feather (feather slots) interactions. The results of the work can contribute to a better understanding of the essential aeroacoustic mechanisms associated with the silent flight of owls.

1.2 Unique owl-wing morphologies

In the pioneering work by Graham in 1934 [4], the three unique morphologies observed on owl wings (e.g., LE serrations, TE fringes, and velvety upper wing surface)

were demonstrated to play a curial role in their silent flight. He pointed out that the stiff serration-like structures can slow down the airflow before it interacts with the real LE of an owl wing, and hence alter the flow characteristics in the boundary layer upon the upper wing surface. On the other hand, the flexible fringes observed on the TE of primary feathers [24] were also reported to help reduce the friction between overlapping feathers during flight and suppress noise-producing vortices. Finally, the loose and downy surface of an owl wing was inferred to dampen the rustling noise induced by feather sliding in the up- and return-stroke. The aeroacoustic association between the three wing morphologies and the owl's silent flight was then experimentally investigated by Gruschka *et al*. [1, 2] They measured the flight path, speed, and noise of a trained owl with original or modified (with LE serrations and TE fringes removed) wings at various altitudes, and found that the modified wings produced the same noise level as observed in other birds of similar body mass. Moreover, these wings did not allow the owl to sustain a stable flight, indicating the aeroacoustic importance of these morphologies to the flight stability of owls.

In this section, we systematically review the previous work associated with the unique owl-wing morphologies and point out the issues that remain to be addressed.

1.2.1 Trailing-edge fringes

As one of the fundamental aerodynamic noise mechanisms for fluid machinery [25], TE noise could be induced by the separated laminar/turbulent boundary layer and the flow interaction/instability at TE. The potential of TE fringes observed on owl feathers for TE noise control has caught the attention of designers and researchers over the past few decades. As a typical morphological feature not found on non-silent birds, the TE fringes on the inner vane of owl feathers [20] have been widely investigated with various models and applied as a conceptual biomimetic design for fluid machinery (e.g., airfoils, rotors, and wind turbines) to reduce noise [7]. Howe carried out several pioneering theoretical investigations into sound reductions of a flat plate airfoil with sinusoidal and sawtooth fringes distributed at the TE, finding that the acoustic performance of the fringes is closely associated with the shape of the fringes. The sawtooth fringes had better acoustic performance [26, 27]. Azarpeyvand *et al*. [28] derived theoretical models to predict the noise radiation from TEs with complex fringes, and achieved analytical results that were

consistent with experimental measurements [29] while showing that Howe's formula overpredicts the level of noise reduction. Through direct numerical simulations (DNS), Jones *et al.* [30] studied the aeroacoustic characteristics of a NACA0012 airfoil with sawtooth TE fringes and demonstrated that these fringes can alter TE-induced flow structures and facilitate the formation of horseshoe vortices between the fringes. Gruber *et al.* [29] conducted both a model-based analysis and wind tunnel experiments, reporting that fringes with various geometric characteristics could achieve a reduction of 3–5 dB broadband sound. To reveal the effect of TE fringes on passive flow control and sound reduction, Avallone *et al.* [31-33] and Prigent *et al.* [34] visualized the near-field flow structures induced by TE fringes using particle image velocimetry (PIV) and found that the turbulent structures can be remarkably suppressed well by the fringes. Moreover, the characteristics of the boundary layers and pressure fluctuations were observed to vary along the edge of a fringe, and this was closely associated with sound reduction [32]. Thomareis *et al.* [35] presented the flow characteristics of a NACA0012 airfoil with three different TE shapes and suggested that the intensity of vortex shedding can be remarkably suppressed because of the decorrelation of the spanwise coherence of vortices due to the TE fringes. Zhou *et al.* [36] investigated through wind tunnel experiments the aeroacoustic features of an airfoil with flexible fringes attached to the TE. Such fringes can lead to an additional 2–3 dB reduction in high-frequency sound. Through large-eddy simulations (LESs) of airfoils with TE fringes, Zhu *et al.* [21] observed a sound reduction over a broad range of frequencies, but at a much higher Reynolds number (*Re*), using the geometric parameters of fringes from owl wings. This was further confirmed by Li *et al.* [37] in a parametric study associated with TE fringes at high *Re*s, indicating that TE fringes can suppress the turbulent fluctuations and hence reduce the noise. Direct measurements of the morphologies of barn owl feathers were carried out by Bachmann *et al.* [20, 24], who employed imaging techniques to analyze the geometric characteristics of TE fringes, providing a basis for the modeling of the fringe structures.

Herr *et al.* [38-40] conducted various parametric instigations on the geometric characteristics of TE fringes. They first carried out a series of acoustic and aerodynamic measurements with brush-type fringes and reported that a remarkable sound reduction of 10 dB could be achieved. It was inferred that the brush-type fringes could suppress not

only the narrowband bluntness noise (tonal noise) but also the broadband noise induced by the turbulent boundary layer passing over the TE [38]. They then conducted additional wind tunnel experiments to explore the design criterion of the TE fringes and demonstrated that the geometric parameters of the fringes should be carefully designed to obtain better acoustic performance, particularly the interval between fringes [39]. Oerlemans *et al.* [41] applied the TE fringes to a three-bladed wind turbine and measured the surrounding acoustic fields. They found that the fringed blade produces much less low-frequency noise. However, the high-frequency noise is enhanced due to the increased wingtip noise. Overall, a sound reduction of 3.2 dB could be achieved for the fringed blade, indicating great application prospects for industry. Moreau *et al.* [42] introduced two types of fringes (i.e., fringes with wide and narrow wavelengths, respectively) and carried out a series of experiments. The results demonstrated that the wider fringes could suppress the overall sound reductions of 11 dB, whereas the narrower fringes increase the overall sound pressure levels by 4 dB. With visualizations of the TE flows, they further reported that the narrow fringes could produce plenty of high-intense spanwise vortices, which increase the tonal noise of the model, indicating that the geometric parameters of the fringes (e.g., wavelength to length ratio) should be selected according to the flow conditions. However, they did not give design criteria for the fringes under different conditions. Arce León *et al.* [43] measured the characteristics of the boundary layer of a NACA0018 airfoil coupled with sawtooth TE fringes and pointed out that the fringes exert significant influence on the nearby flows whereas have no impact on the upstream flows, leading to suppression of surface pressure fluctuations and reduction of the far-field noise. Liu *et al.* [44] further measured the wake flow characteristics of symmetric and cambered airfoils with various fringes. They found that the flow characteristics of the tip plane and root plane of the airfoils are definitely different. Benefit from the complex spanwise flow interaction, the fluctuations of the wake flows were suppressed remarkably. However, the fringes were pointed out to damage the aerodynamic performance of the airfoils at a low angle of attack (*AoA*). Talbays *et al.* [45] conducted an investigation on the aeroacoustic characteristics of a NACA0012 airfoil with an array of flexible flaplets attaching on the surfaces in the vicinity of TE. Various wind tunnel experiments were carried out with the treated models at a broad range of *Re*s and *AoA*s. It was found that the flaplets on the pressure surface could

suppress the tone noise induced by the airfoil through passive flow control of the laminar boundary layer. However, the efficiency of the flaplets on the suction surface were much lower. The authors suggested that the flexibility of the TE treatments (e.g., fringes and flaplets) may play an important role in terms of passive flow control. Gelot *et al.* [46] carried out an study of the effects of TE fringes on airfoil tonal noise by numerical methods, in which a significant suppression of tonal noise could be observed. Combining with the flow structures surrounding the airfoil, they inferred that the reduction may be attributed to the weakened aeroacoustic loop by the fringe-like structures. Using a NACA0012 airfoil with various TE fringes, Al Tlua *et al.* [8] analyzed the Reynolds number effects of the fringes by acoustic measurements. It was found that the acoustic characteristics of the airfoil are highly sensitive to the *Re*s and *AoA*s. Interestingly, the tonal noise could be robustly suppressed by the fringes. They also pointed out that the parameter optimization of the fringe geometry could further increase the sound reduction. Celik *et al.* [47] carried out plenty of experiments with a TE-fringed flat plate. The large-scale fringes were confirmed to reduce broadband noise robustly by weakening the surface pressure levels and spanwise coherence. Hasheminasab *et al.* [48] addressed an experimental study of the wake dynamics of a NACA0012 airfoil with sawtooth TEs. The wake flow characteristics induced by the airfoils with and without TE fringes were measured by PIV measurements at a high *Re* of 78 000. In contrast to the previous studies, the cut-in fringes were found to increase the flow fluctuations in the wake. However, the influence of the increased fluctuations on the far-field acoustic characteristics was not investigated. For the purpose of exploring TE treatment with superior acoustic performance, Shi *et al.* [49] constructed an innovative TE configuration by combining the cut-in fringes with the finlet on the surface near the TE. They reported that as the fringes are good at suppressing low-frequency sound whereas the finlet on the surface are good at reducing high-frequency sound, their combination may produce a powerful noise-reducing design for engineering applications. LES-based simulations were performed to resolve the instantaneous flow structures induced by the fringe-finlet configuration and the Ffowcs Williams–Hawkings equation (FW-H) [50, 51] was employed for far-field sound prediction. A remarkable sound reduction of 20 dB and an improved aerodynamic performance was achieved for the novel configuration, indicating its superior aeroacoustic performance and

huge potential for industrial applications. The mechanisms of sound reduction were attributed to the breaking of TE vortices and the suppression of turbulent fluctuations. Wei *et al*. [7] introduced the fringes to a propeller to explore the possibilities of their application in rotating machinery. The aerodynamic noise induced by the propeller under various rotational speeds was measured experimentally in the vertical and horizonal directions. It was found that the three different types of fringes can lead to an aerodynamic noise reduction robustly. Besides, the thrust forces of the fringed propellers were also improved by 10% by the fringes compared to the clean propeller. However, for a gliding wing, TE fringes are normally found to have no pronounced influence on aerodynamic force production. In a recent work, Zhao *et al*. [52] explored the methods of improving the aerodynamic performance of a TE-fringed airfoil. They first optimized the airfoil configuration and then introduced the fringe-like structures on the TE. Consequently, both improved aerodynamic forces and lowered sound levels could be obtained for the optimized airfoil, which were verified experimentally by the authors. Wang *et al*. [53] investigated the aeroacoustic characteristics of an owl-inspired asymmetric oblique TE fringe configuration. With visualizations of the nearby flow fields, they found that the asymmetric oblique fringes could remarkably suppress vortex shedding and hence achieve an additional sound reduction of 3.8 dB compared to the conventional sawtooth fringes.

There are also some investigations on the novel porous TE treatment inspired by the permeable fringes, which is recognized to have the capacity of passively controlling the separated boundary layer characterization. Bae *et al*. [54] applied a porous surface in the vicinity of the TE to investigate their effects on the noise induced by a flat plate model. Through the LES-based simulations for turbulent flows and the linearized perturbed compressible equations (LPCEs) for acoustic fields, they demonstrated that the porous surface could suppress the flow fluctuations near the TE and hence the diploe noise generated by vortex shedding. Kisil *et al*. [55] simulated the aerodynamic noise induced by a gust flow passing a porous TE. The results showed that the porous treatments could suppress low-frequency sound but sustain mid-frequency sound and even increase the sound at high frequencies. Shi *et al*. [56] also added a porous wavy TE to the wing to investigate its sound reduction capacity by numerical methods. The novel TE treatment was reported to significantly reduce TE noise without any damage to aerodynamic

performance. However, in the numerical investigation of the aeroacoustic effects of a porous TE by Teruna *et al*. [57], it was found that the porous treatment at TE will increase the drag forces of the airfoil. The discrepancy between two investigations may be caused due to the different materials of the geometries and a further comparative study is required in terms of the impacts of materials (e.g., density and roughness).

So far, two-dimensional (2D) numerical simulations have mainly been utilized in investigating the aeroacoustic effects of owl-inspired TE fringes based on finite-span models with translational, periodic boundary conditions. In contrast, the three-dimensional (3D) aeroacoustic characteristics associated with TE fringes remain yet poorly studied. Gelot *et al*. [46] investigated the aeroacoustic effects of two different TE-fringed models in which the span lengths were, respectively, 5% and 10% of the chord length. They found for the two models noticeable differences in the acoustic source phases and the far-field tonal noise. Using a numerical model, Turner *et al*. [58] found that using wider wings can provide more accurate far-field acoustic results. However, they neither explored the 3D vortical flow structures in terms of the spanwise and chordwise LE and TE vortices as well as the wingtip vortices nor the 3D aeroacoustic features. Given the evidence that the passive flow control of near-field 3D flow structures induced by TE fringes may benefit sound reduction [30, 35, 37], exploring the effects of TE fringes on the 3D aeroacoustic characteristics is of great importance in revealing the underlying physical mechanisms associated with TE fringes during owl flight.

1.2.2 Leading-edge serrations

As another well-known owl-wing morphologies, LE serrations observed on owl's outermost remiges [11, 15, 24] are recognized to play an important role in the silent owl flight [4, 5, 10-12, 14] through a passive control of the airflows surrounding the wing feathers in terms of boundary layer separation, laminar-turbulent transition, and flow instability [59-61].

The LE serrations are indeed the barb endings of owl feathers. They are stiff so as to maintain the aerodynamic configurations during owl flight. The LE serrations can alter the incoming flows before they interact with the wings. Consequently, the flow characteristics (e.g., flow separation, boundary layer characteristics, and vortex generation) of the owl

wings are totally altered owing to the serrations. Thus, the passive flow control by the LE serrations may not only provide a solution for reducing LE noise but also the TE noise. Geyer *et al*. [62, 63] compared the acoustic characteristics of prepared wings of a barn owl with and without LE serrations in a wind tunnel. They then reported that the LE serrations can reduce noise, particularly during high *AoA* phases of the flight (e.g., a landing phase [63]). Winzen *et al*. [64] manufactured several models of barn owl wings, which had a curved LE with serrations distributed from the midspan to the wingtip. The PIV and force measurements of the artificial models demonstrated that the serrations can lead to suppression of flow separations in the distal part of the wing, thereby stabilizing the surrounding airflows, but at the expense of aerodynamic performance. Narayanan *et al*. [16] measured the sound produced by LE serrations with various geometric shapes and reported that a remarkable sound reduction of 9 dB can be achieved for a flat plate model owing to the presence of LE serrations. They also pointed out that the acoustic performance of the LE serrations is closely associated with their geometric parameters (e.g., length of a serration). Chaitanya *et al*. [65] also measured the sound induced by turbulent flows passing through an airfoil with LE serrations. In their experiments, six serration profiles were introduced, and the induced far-field sound levels were measured in an open-jet wind tunnel. All serration profiles were found to suppress sound robustly, particularly at low frequencies whereas spanwise varying serrations gained more sound reductions than conventional serrations with a constant wavelength. Huang [66] carried out an analytic investigation on the scattering of acoustic waves from a serrated LE. Similarly, they also found that the geometric characteristics of the LE serrations play an important role in sound reduction. They reported that the sawtooth serrations performed better than the sinusoidal serrations at suppressing sound and the wider serrations have better acoustic performance. Besides, they also pointed out that the serrations are more effective in suppressing high-frequency sound according to their theoretical models. Using plate models with LE serrations, Ayton *et al*. [67] also analytically investigate the sound induced by gust-airfoil interaction. Their work was then extended to plate models with spanwise varying LE serrations [17]. Five types of serrations comprising sawtooth, slitted u-root, slitted v-root, square wave and chopped peak were investigated. Obvious sound reductions were observed for models with serrations owing to the interference between flows in tip

planes and root planes. Kamliya Jawahar *et al*. [68] measured the sound generated by a novel serrated slat cusp. The slat serrations were demonstrated to suppress the intensity of vortex shedding, and hence reduce noise in the far-field, although the fluctuations of the surface pressure were increased. On the other hand, the aerodynamic effects of the serrations were insignificant.

The LE serration-induced flow and acoustic characteristics were also investigated through numerical methods. Polacsek *et al*. [9] presented a novel biomimetic design for controlling broadband noise generated by outlet guide vanes by introducing serration-like structures on the outlet. The length and width of the serrations were various along the span. Through simulations and experiments, a sound reduction of 2.5-3.5 dB could be achieved for the serrated vanes. Pérez-Torró *et al*. [69] studied the flow characteristics of a stalled NACA0012 airfoil with an owl-inspired wavy LE by performing LESs. They then demonstrated that the wavy LE can remarkably suppress unsteady aerodynamic fluctuations acting on the airfoil. Wang *et al*. [70] introduced a similar wavy LE into an H-type wind turbine model and found that the wavy LE can effectively suppress flow separations and delay aerodynamic stall, benefit from which more power generation and a higher maximum lift force are gained for the LE wavy model. However, the implementation of large-scale wavy serrations may obscure the essential mechanisms of the owl's silent flight, as the serrations of owl feathers are fine and extremely small in size [15]. In the previous studies by Rao *et al*. [59], 2D models with and without LE serrations were established based on the measured geometric parameters [71] of an owl's single feather, resulting in a fine serration configuration. The flow fields of the serrated and non-serrated models were then resolved by LESs and PIV measurements at a low *Re* of 6000, identical to a typic flight speed during owl's flight [64]. With visualizations of contours of streamwise velocity and Reynolds shear stress, they found that the small-scale serrations lead to passive control of the suction flows in terms of laminar-turbulent transition and flow instability. Through a spectral analysis of the surface pressure time series, the small-scale serrations were found to effectively suppress high-frequency TE self-noise ($f > 2$ kHz). They suggested that the mechanisms of the sound reduction may be attributed to the breaking of LE vortices by serrations. In addition, they reported that the serrations reduce the aerodynamic performance at low *AoA*s (e.g., 5°) whereas maintaining

the aerodynamic forces at high *AoA*s (e.g., 15°), thus providing a solution to the trade-off between aerodynamic force production and sound reduction at high angles of attack. In their subsequent study [60], it was found that the passive flow control by serrations is robust when interacting with fluctuated incoming flows. They introduced two kinds of wind gusts and found that the serrations could suppress the aerodynamic force fluctuations robustly by passively controlling the turbulent flows over the upper surface. The investigation was then extended to 3D and high *Re*s [61]. They respectively added the LE serrations to the midspan and wingtip of a plate model and conducted various LESs to resolve the 3D turbulent flows surrounding the serrations. They then reported that the passive flow control induced by the serrations are robust in 3D models, and the serrations at midspan are more effective that those distributed in the vicinity of wingtip, which is corresponding to the serration distribution of a real owl feather. Kim's group from University of Southampton conducted a series of research with aim to reveal the acoustic mechanisms associated with the serrations, including numerical [18, 46, 58, 69, 72, 73], analytic [67], and experimental [16] investigations, which can help to understand the underlying mechanisms of LE serrations in terms of aerodynamic force production and sound reduction.

As the end part of the barbs, the LE serrations possess complex 3D features. However, the previous investigated serration profiles were usually 2D (e.g., neglect the inclination, bending, and twist angles) for simplicity, even in a 3D model. Bachmann *et al.* [15] pointed out that the serrations have complex 3D shapes and angles. Their geometric parameters comprising length, width, and density were various in the spanwise direction. Based on the measurements by Bachmann *et al.* [15], Muthuramalingam *et al.* [74] constructed a model with 3D serrations inspired by owls by taking the 3D shapes and angles into consideration. The serrations were closer to real serrations observed on owl feathers in shape and had a various diameter distribution from root to tip. Through LESs, they found that the 3D serrations could passively control the direction of the spanwise flows, and hence attenuate the crossflow instabilities. Wang *et al.* [75] introduced the LE serrations to a mixed flow fans to investigate their rotational characteristics (i.e., aerodynamic force production and sound reduction). Through experimental measurements and LESs, they reported that the LE serrations could reduce noise while sustaining

aerodynamic performance of the fans. The morphological effects of LE serrations on the acoustic signatures of the mixed flow fan were also investigated numerically [76]. After that, they developed a novel aproach for visualizing the surface noise strength by means of the FW-H analogy and LESs, by which the discrepancy of distributions of acoustic sources between serrated and non-serrated fans could be presented intuitively. They then pointed out that the aeroacoustic characteristics of LE serrations are remarkably distinguished under different inclination angles in terms of serration-induced tip vortices and acoustic frequency characteristics.

As aforementioned, the aeroacoustic characteristics of LE serrations have been widely investigated with single feathers/airfoils. However, owl wings are composed of multiple feathers, and during flight there are strong interactions between the feathers, which could be one of the dominant wing acoustic mechanisms during owl flight [77-79]. How the serrations affect the feather-feather (feather slots) interactions during an owl's flight remains an open question. Given that the LE serrations are normally observed on the outermost feathers of an owl wing [24, 80], the serration structures may exert remarkable influence on the overall flow fields surrounding the wing [63, 64], and hence markedly alter the aeroacoustic characteristics of the downstream feathers and passively control the noise induced by the interactions of feathers.

1.2.3 Velvety upper wing surfaces

There have been relatively few studies on the aeroacoustic features associated with the velvety surface of an owl's wing [22, 23, 81, 82]. In an experimental study of the aerodynamic and acoustic performance for an airfoil with a specific surface coating, Vad *et al.* [22] reported that the surface coating can reduce the sound pressure levels, but also lower the aerodynamic force production due to the surface roughness. PIV-based wind tunnel experiments using an airfoil with a realistic velvet-inspired surface [81] indicated that the velvet-surface roughness can alter the features of the separated boundary layers.

Showkat Ali *et al.* [83] addressed an integrated analysis of the aeroacoustic characteristics of a plate with novel porous surface at TE by wind tunnel experiments. The results demonstrated that the porous surface could suppress vortex shedding and flow instabilities effectively. Besides, the porous treatment also found to destroy spanwise

coherence of the turbulent flows. They then expanded the porous structures to nearly the whole upper and lower surfaces [84]. Their effects on the characteristics of the boundary layer were then analyzed experimentally. Moreover, the effects of the material properties of the porous surface were also studied. Zhou *et al*. [23] tested the noise induced by an owl-inspired velvety surface in an anechoic wind tunnel. They then demonstrated that the velvet surface could significantly alter the far-field acoustic spectral characteristics: reducing low-frequency noise whereas increasing noise at high frequencies. The mechanisms were suggested to be association with the altered boundary layer thickness and velocity fluctuations by the velvety structures. They also developed an analytic model for predicting sound radiation of the model with velvety surface based on the mean and fluctuating streamwise velocity time series in the near wake, by which the acoustic results matching experimental data could be obtained. More experiments on the wings of different species are required to further reveal the mechanisms associated with the velvety surfaces.

1.2.4 Interactive effects between the wing morphologies

While the specific morphological effect of the three morphologies on aerodynamic force production and sound reduction has been widely investigated, the aeroacoustic interaction between morphologies (e.g., TE fringes and LE serrations) remains an open question. Wang *et al*. [19] carried out an integrated study of the aeroacoustic characteristics of an NACA0012 airfoil with both LE serrations and surface ridges. The combination of the two morphologies was found to remarkedly reduce aerodynamic noise by suppressing spanwise flow coherence of the airfoil. Fink *et al*. [85] conducted a systematically investigation on the concepts of airfoil noise reduction. Various treatments of the LE and/or TE of wings were introduced and investigated. In their case, however, the TE fringes were reported to increase noise. Liu *et al*. [86] presented an integrated study of the aeroacoustic characteristics of a novel blade with both wavy LE serrations and sawtooth TE fringes. The flow structures of the blade were resolved by LESs. They found that the surface pressure fluctuations and vortex shedding frequencies are suppressed remarkedly for the bionic blade, benefit from which a sound reduction of 2.1 dB could be observed. However, the underlying mechanisms of sound reduction were not extensively analyzed. Wang *et al*. [87] introduced a similar bionic design for an airfoil (i.e., wavy LE serrations and sawtooth TE

fringes) and carried out various LESs. They found that the bionic airfoil even possesses a better aerodynamic performance compared to the base airfoil over a broad range of *AoA*s (5–15°), indicating that the wavy serrations may increase the pressure difference in the vicinity of LE. Besides, it was observed that the turbulent eddies surrounding the bionic airfoil are much smaller in size, so that the surface pressure fluctuations were suppressed.

The silent flight of owls is induced by various features or morphologies [10]. The interactive effects between these features are compound but are of curial importance to fully understand the physical mechanisms of the owl's silent flight. So far, the associated investigations are still rare and may be an important topic for future research.

1.2.5 Other factors

There are some other factors contributing to the owl's silent flight [88], such as the high-cambered airfoils [89], wing flexibility [90], large aspect ratio wings [91, 92], and so on [93-95].

Kondo *et al.* [89, 96-98] carried out integrated numerical tests of the aeroacoustic characteristics of the owl-inspired high-cambered airfoils. Not like a plate model used in previous studies, the high-cambered airfoils were found to possess flow separations both on the suction and pressure sides. The characteristics of the near-wall flows were hence highly sensitive to the *AoA*s. Specifically, when the *AoA*s were low, the flow separation occurred in the pressure surface. Whereas when the *AoA*s were high, a separation bubble of suction flows could be observed. They then compared the aerodynamic characteristics of the owl-inspired wings with other well-known airfoils at a *Re* of 23,000 and reported that the owl-inspired wings have a better aerodynamic performance [97, 98]. Further acoustic characteristics of the owl-inspired wings were presented by Li *et al.* [99] and compared with wing airfoils of other birds. By the means of LES-based simulations and FW-H analogy, they demonstrated that the owl-inspired airfoil could remarkedly suppress far-field sound pressure levels. Liu *et al.* [100] also numerically investigated the aeroacoustic performance of the owl-inspired high-cambered airfoil at a low *Re* of 12,300. They reported that the owl-inspired airfoil achieves better aerodynamic performance compared to a NACA0006 airfoil. There are also some experimental investigations. Anyoji *et al.* [101] manufactured an airfoil following the work by Liu *et al.* [102] and measured

the flow characteristics in a wind tunnel. An obvious separation bubble is observed on the pressure surface of the high-cambered airfoil, which leads to a pronounced increase in lift force production. Sunada *et al*. [103, 104] also tested the effects of airfoil configurations on aerodynamic forces, in which various airfoil configurations were tested.

Using a flat plate model with bionic surface treatment (i.e., finlets on the surface), Afshari *et al*. [93] conducted experiments to reveal the finlet-induced boundary layer characteristics. They reported that the spacing between finlets exert significant influence on the downstream flows, and hence lead to a reduction of mid- and high-frequency noise. They further pointed out that the spacing between finlets is a key parameter to obtain an optimal sound reduction. Gao *et al*. [94] presented a study of the aerodynamic performance of a novel herringbone groove structure. The novel structure was added on the surface of a bionic blade. Furthermore, the airfoil section of the blade was optimized by an owl-inspired high-cambered airfoil. Through simulations, they reported that the groove structure could enhance the power coefficient of a wind turbine rotor by increasing the pressure difference between the two surfaces of the blade.

The LE alula observed on a wing of bird is recognized to enhance aerodynamic force. Bao *et al*. [95] added an alula-like structures to a 3D flapping wing and resolved the surrounding transient flow fields by solving the Reynolds Average Navier-Stokes (RANS) equations. They reported that there are two effects (i.e., slot effect and vortex generator effect) induced by the alula contributing to the enhancement of aerodynamic forces. They further point out that the two effects play different roles during the upstroke and downstroke of the flapping wing. However, the acoustic effects of the alula have never been addressed.

1.3 Research contents and significance

This thesis describes an integrated study of the aeroacoustic characteristics of the wings with owl-inspired LE serrations and TE fringes. The analysis is focused specifically on the aeroacoustic interaction between the two morphologies, the 3D aeroacoustic characteristics induced by TE fringes, and the LE serration-induced feather-feather (feather slots) interactions, by combining LESs of unsteady near-field flow structures with the

FW-H equation for sound radiation. Using the models based on the real parameters of the owl feather, various aeroacoustic simulations were performed at a low *Re* of 6000, which is identical to the typical speed of an owl's forward flight. The results of the thesis can hence reveal the essential mechanisms utilized by owls during their flight and inspire innovative wings for biomimetic designs. The main contents of this thesis include:

(1) Chapter 2 presents an integrated study of the aeroacoustic interaction between TE fringes and LE serrations. Using the owl-inspired wing models with/without LE serrations and TE fringes, the effects of TE fringes on aerodynamic force production and sound reduction are studied. With visualizations of near-field flow structures, vortex dynamics, and flow fluctuations, the underlying mechanisms associated with TE fringes are revealed. Then the interaction between TE fringes and LE serrations in terms of flow stabilization and sound reduction is investigated.

(2) In chapter 3, the 3D aeroacoustic characteristics induced by owl-inspired TE fringes are examined. Four 3D single-feather models were constructed: one clean wing model and three wing models with fringes distributed differently spanwise. The aerodynamic forces and 3D acoustic characteristics are compared between the fringed and clean models so as to reveal the 3D aeroacoustic effects of the TE fringes. Then, the aeroacoustic mechanisms associated with the 3D TE fringes are investigated by visualizing the near-field 3D flow structures, vortex dynamics, and flow fluctuations. Furthermore, the spanwise distribution effect of the fringes is analyzed by comparing the aeroacoustic results of the partial fringed models.

(3) Next, the effects of owl-inspired LE serrations on the feather-feather (feather slots) interactions in terms of aerodynamic force production and sound reduction are investigated in chapter 4, by constructing tandem wing models with owl-inspired LE serrations on the LEs of the fore and hind wings. The aeroacoustic analysis is focused on the effects of the gap distance between fore and hind wings on the tandem wing aeroacoustics.

(4) Finally, the contributions of the thesis are summarized in chapter 5, as well as the future plans.

2 Aeroacoustic interaction between owl-inspired trailing-edge fringes and leading-edge serrations

2.1 Introduction

The silent flight achieved by owls is attributed to the unique owl-wing morphologies, characterized by LE serrations, TE fringes, and a velvety upper wing surface [10]. As a typical morphological feature of owl wing, the TE fringes on the inner vane of owl feathers [20] have been widely investigated and applied as a conceptual biomimetic design for various fluid machinery (e.g., airfoils, rotors, and wind turbines) to reduce aerodynamic noise [7, 48]. Additionally, the LE serrations observed on owl's outermost remiges [11, 15, 24] are also recognized to play an important role in owl's silent flight [4, 5, 10-12, 14] through a passive control of the airflows surrounding the wing feathers in terms of boundary layer separation, laminar-turbulent transition, and flow instability [59-61]. While the specific morphological effect of either LE serrations or TE fringes on aeroacoustic force production and sound reduction has been widely studied separately, the interactive effect (i.e., LE-TE aeroacoustic interaction) remains poorly understood.

In this section, we aim to unveil the integrated aeroacoustic characteristics produced by LE serrations and TE fringes. Four owl-inspired models of single feather with/without fringed TE and serrated LE were constructed. The flow and acoustic fields surrounding the owl-inspired models were then resolved by combining the LES modeling of unsteady near-field flow structures and the solution to the FW-H equation for sound radiation. By comparing the aerodynamic forces and acoustic results between the clean and fringed models, the effects of TE fringes on aerodynamic force production and sound reduction are investigated. The associated aeroacoustic mechanisms are then revealed by visualizing the near-field flow structures, vortex dynamics, and flow fluctuations. Furthermore, the aeroacoustic interaction between the TE fringes and LE serrations are examined to show how these two morphologies complement each other during owl's silent flight.

2.2 Owl-inspired single-feather models with fringed TE and serrated LE

2.2.1 2D single-feather models

Following our previous studies [59-61, 71], we employed four single-feather wing models to mimic the LE serrations and TE fringes observed at the outmost feathers (10th primary feathers) of an owl wing [Fig. 2-1(a)]. As illustrated in Fig. 2-1(b), given a rectangular shape and dimensions of 150 mm × 30 mm [71], a clean wing model (CW model), a wing model with fringed TE (TE model), a wing model with serrated LE (LE model), and a wing model with both TE fringes and LE serrations [LE-serrated and TE fringed model (LT model)] were constructed, in which the camber and thickness distributions of the remex were neglected. For the sake of simplicity, both fringe- and serration-like structures [Figs. 2-1(c), 2-1(d)] are distributed uniformly and aligned with the incoming flow, while the owl-inspired TE fringes have a much higher density (triple) than the LE serrations [Fig. 2-1(a)] [24].

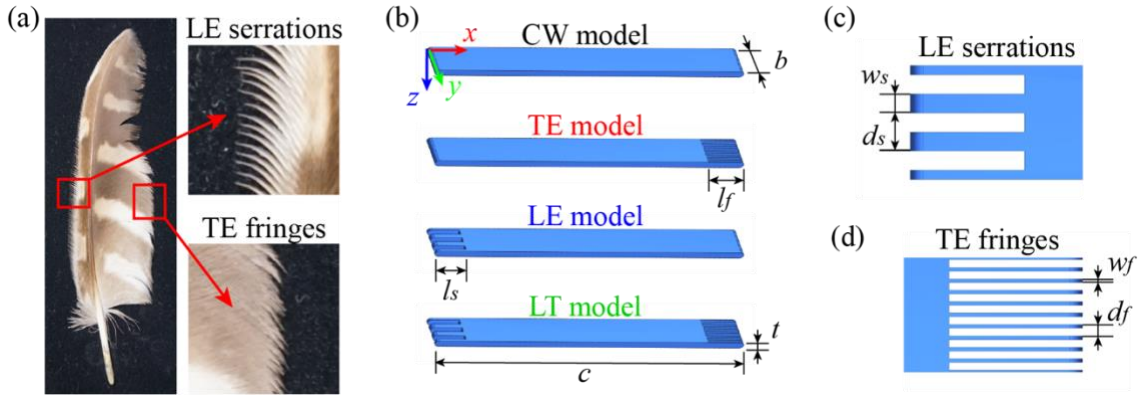

Fig. 2-1. (a) LE serrations and TE fringes of an owl's 10th primary feather. (b) Four owl-inspired wing models (CW model: clean wing model; TE model: TE-fringed wing model; LE model: LE-serrated wing model; and LT model: wing model with serrated LE and fringed TE). (c) LE with serration-like structures. (d) TE with fringe-like structures.

Note that the computational fluid dynamics (CFD) modeling was conducted with 2D infinite models with translational periodic boundary conditions applied on two sides; as verified in our previous studies [59-61, 71], this significantly reduces the computational cost while enabling the essential 2D mechanisms associated with both TE fringes and LE

serrations to be investigated. Table 2-1 summarized the basic geometric characteristics of the models, which were determined by the measured values of a real owl feather from Ikeda *et al.* [71] and Bachmann *et al.* [20, 24] Moreover, as defined in Fig. 2-1(b), the origin of the coordinate system was located at the LE of the wing models. The *x*, *y*, and *z* axes respectively correspond to chordwise, spanwise, and negative vertical (wall-normal) directions.

Table 2-1. Basic geometric parameters of the computational models.

Parameter	Symbol	Size (mm)
Chord	c	30.0
Span	b	3.0
Thickness	t	0.67
Length of fringes	l_f	3.5
Width of fringes	w_f	0.1
Interval between fringes	d_f	0.3
Length of serrations	l_s	3.0
Width of serrations	w_s	0.5
Interval between serrations	d_s	1.0

To resolve the large-scale separated flows around the serrated LE and fringed TE wing models, a multi-block, structured grid system was employed, consisting of an H-type global grid [Fig. 2-2(a)] and an O-type local grid [Fig. 2-2(b)]. The inlet and outlet boundaries and the far-field were placed at a distance of 20 chord lengths (20c) from the wing surface. The grids were made to be denser around the wing surface, particularly at the LE and TE, to ensure the high resolution of the vortical and separated flows and the boundary layers on the wing surface [Figs. 2-2(c), 2-2(d)]. The height of the first layer is defined by the formula $\delta = 0.05c/\sqrt{Re}$, where *Re* denotes the chord length-based Reynolds number. Given the freestream velocity (U_∞) of 3 m/s, which is a typical velocity in an owl's forward flight (2.5–7.5 m/s) [64], *Re* was calculated to be 6000 (air density $\rho = 1.185\ kg \cdot m^{-3}$; air viscosity $\mu = 1.834 \times 10^{-5}\ kg \cdot m^{-1} \cdot s^{-1}$). Furthermore, the *AoA*s were varied over a broad range of 5–15°, as normally observed in an owl's silent flight [59].

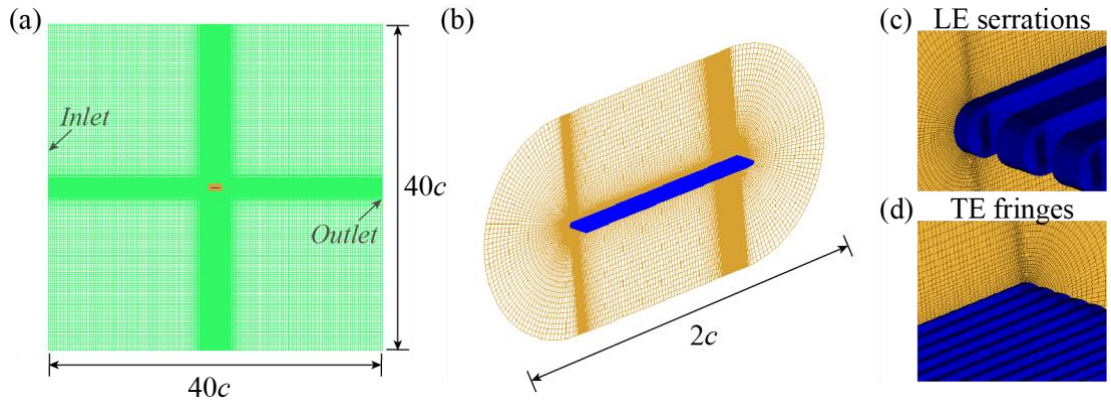

Fig. 2-2. (a) Multiblock, structured grid system around wing models with an H-type global domain (green) and an O-type local domain (brown). (b) O-type near-field domain grid. Clustered grid distributions at (c) serrated LE and (d) fringed TE.

2.2.2 Loose coupling of LES and FW-H analogy

Following our previous studies [59-61], we employed LES-based CFD modeling to resolve the large-scale eddies, comprising the laminar–turbulent transition, vortical and laminar boundary layers, rather than combining the Reynolds-averaged Navier–Stokes approach with turbulent models. The eddies smaller than grid size were filtered out and processed by a subgrid model of the wall-adapted local eddy-viscosity (WALE) [105] so as to save the computational cost.

Given the low freestream velocity, the governing equations for incompressible flows can be written as

$$\frac{\partial \bar{U}_i}{\partial x_i} = 0, \tag{2-1}$$

$$\frac{\partial \bar{U}_i}{\partial t} + \frac{\partial}{\partial x_j}\left(\bar{U}_i \bar{U}_j\right) = -\frac{1}{\rho}\frac{\partial \bar{p}}{\partial x_i} + \frac{\partial}{\partial x_j}\left[\nu\left(\frac{\partial \bar{U}_i}{\partial x_j} + \frac{\partial \bar{U}_j}{\partial x_i}\right)\right] - \frac{\partial \tau_{ij}}{\partial x_j}, \tag{2-2}$$

where τ_{ij} denotes the subgrid-scale stress tensor, expressed as

$$\tau_{ij} = \overline{U_i U_j} - \bar{U}_i \bar{U}_j. \tag{2-3}$$

The eddy-viscosity assumption is adopted to close the τ_{ij} term, modeled as

$$\tau_{ij} - \frac{\delta_{ij}}{3}\tau_{kk} = -2\nu_t \overline{S_{ij}}, \tag{2-4}$$

where δ_{ij} is Kronecker's delta and v_t is the subgrid-scale turbulent viscosity; $\overline{S_{ij}}$ is the rate-of-strain tensor of the resolved field, which is defined as

$$\overline{S_{ij}} = \frac{1}{2}\left(\frac{\partial \bar{U}_i}{\partial x_j} + \frac{\partial \bar{U}_j}{\partial x_i}\right). \quad (2-5)$$

With the WALE subgrid-scale model, the eddy viscosity v_t is given by

$$v_t = (C_w\Delta)^2 \frac{\left(S_{ij}^d S_{ij}^d\right)^{3/2}}{\left(\bar{S}_{ij}\bar{S}_{ij}\right)^{5/2} + \left(S_{ij}^d S_{ij}^d\right)^{5/4}}, \quad (2-6)$$

where S_{ij}^d denotes the traceless symmetric part of the square of the velocity gradient tensor, defined as

$$S_{ij}^d = \frac{1}{2}\left(\bar{g}_{ij}^2 + \bar{g}_{ji}^2\right) - \frac{1}{3}\delta_{ij}\bar{g}_{kk}^2. \quad (2-7)$$

Here, $\bar{g}_{ij}^2 = \bar{g}_{ik}\bar{g}_{kj}$ and $\bar{g}_{ij} = \partial \bar{U}_i / \partial x_j$ represent the velocity gradient tensors. The value of the subgrid-scale model constant (C_w) is 0.325.

The simulations were performed with the commercial software ANSYS Fluent 16.0 (ANSYS, Inc.) with a time step of $\Delta t = 5 \times 10^{-5}$ s and up to 20,000 steps, which is identical to a physical time of 1.0 s. The flow fields generally converged to a stable state after 15,000 time steps, whereupon post-processing was applied for both aerodynamic and acoustic analyses.

While both the large-scale eddy flow fields and the acoustic fields around the wing models may be solved directly in a tightly coupled manner, there is a need for high numerical resolution, and hence a high computational cost, because of the large differences in the length scale between the acoustic and flow variables [59]. Thus, we utilized a widely recognized approach to resolve the flow and acoustic fields in a loosely coupled form: the transient flow fields were resolved first by the LES method, and then the FW-H equation was solved to ensure a quick and accurate estimation of the acoustical propagation [50, 51, 106-108].

The FW-H equation is a derivative from the general form of Lighthill's acoustic analogy [106, 107] and Curle's extended version [108], which can predict the sound induced by the interaction between moving objects and fluids accurately. The FW-H equation [50, 51] can normally be written in the form

$$\frac{1}{{a_0}^2}\frac{\partial^2 p'}{\partial t^2} - \nabla^2 p' = \frac{\partial^2}{\partial x_i \partial x_j}\{T_{ij}H(f)\} - \frac{\partial}{\partial x_i}\{[P_{ij}n_j + \rho u_i(u_n - v_n)]\delta(f)\} + \frac{\partial}{\partial t}\{[\rho_0 v_n + \rho(u_n - v_n)]\delta(f)\}, \quad (2-8)$$

where a_0 and p' denote the sound speed and the sound pressure at the far field, ρ_0 is the static density, u_i, v_i are the fluid velocity component and the surface velocity component in the x_i direction, respectively, and u_n, v_n are the fluid velocity component and the surface velocity component normal to the surface, respectively. $\delta(f)$ is the Dirac delta function and $H(f)$ is the Heaviside function. T_{ij} is the Lighthill stress tensor, defined as

$$T_{ij} = \rho u_i u_j + P_{ij} - {a_0}^2(\rho - \rho_0)\delta_{ij}, \quad (2-9)$$

where P_{ij} denotes the compressive stress tensor.

The complete solution to the FW-H equation includes surface integrals and volume integrals. The surface integrals are mainly attributable to dipole and monopole acoustic sources, corresponding to the second and the third terms on the right-hand side in Eq. (2-8), whereas the volume integrals (quadrupole sources) represent turbulent noise, corresponding to the first term on the right-hand side. Considering the low freestream velocity in owl flight (2.5–7.5 m/s) [64], the dipole sources, which are mainly caused by the unsteady pressure fluctuations on the wing surface, can be regarded as the dominant sources for sound and the volume integrals can be neglected [14]. Thus, we have

$$p'(\vec{x}, t) = {p_T}'(\vec{x}, t) + {p_L}'(\vec{x}, t), \quad (2-10)$$

where ${p_T}'(\vec{x}, t)$ and ${p_L}'(\vec{x}, t)$ denote thickness and loading terms, respectively, which can be expressed as

$$4\pi {p_T}'(\vec{x}, t) = \int_{f=0}\left[\frac{\rho_0(\dot{U}_n + U_{\dot{n}})}{r(1-M_r)^2}\right]dS + \int_{f=0}\left[\frac{\rho_0 U_n\{r\dot{M}_r + a_0(M_r - M^2)\}}{r^2(1-M_r)^3}\right]dS, \quad (2-11)$$

$$4\pi p_L'(\vec{x},t) = \frac{1}{a_0}\int_{f=0}\left[\frac{\dot{L}_r}{r(1-M_r)^2}\right]dS + \int_{f=0}\left[\frac{L_r - L_M}{r^2(1-M_r)^2}\right]dS + \frac{1}{a_0}\int_{f=0}\left[\frac{L_r\{r\dot{M}_r + a_0(M_r - M^2)\}}{r^2(1-M_r)^3}\right]dS, \quad (2-12)$$

where

$$U_i = v_i + \frac{\rho}{\rho_0}(u_i - v_i), \quad (2-13)$$

$$L_i = P_{ij}\hat{n}_j + \rho u_i(u_n - v_n). \quad (2-14)$$

Note that the subscript $f = 0$ stand for the source (emission) surface.

To ensure accurate prediction of the sound radiation via the FW-H equation, the converged stable LES-based flow fields during a period of 4,000 time steps after the 15,000th time step were used for the acoustic analysis. All surfaces of the wing models were regarded as acoustic sources; with the time step of $\Delta t = 5 \times 10^{-5}$ s in the LES simulations, the upper limit of the frequency in the sound spectrum analysis will be $f = 1/(2\Delta t) = 10$ kHz.

2.2.3 Verification and validation

Systematic verification and validation of the LES simulations associated with wing models containing LE serrations were conducted in our previous studies [59-61], by comparing CFD data with PIV measurements. The results were well consistent over a broad range of *AoA*s (0–20°) including velocity and Reynolds stress distributions, and aerodynamic forces.

In this study, a grid independence was first confirmed with three grids, as compared in Table 2-2, at an *AoA* of 10° and *Re* of 6000. The grid density was adjusted to keep the height of the first grid layer unchanged while satisfying the requirement of the dimensionless wall distance, $y^+ = u^* y/\nu < 1$, where u^* denotes the friction velocity, y is the distance to the wall surface, and ν is the local kinematic viscosity of the fluid.

The aerodynamic force coefficients are compared in terms of the time-averaged lift coefficient (C_l), drag coefficient (C_d), and lift-to-drag ratio (*L/D*), which are defined as

$$C_l = \frac{L}{0.5\rho {U_\infty}^2 S} \quad (2-15)$$

$$C_d = \frac{D}{0.5\rho {U_\infty}^2 S} \qquad (2-16)$$

where L and D represent the lift and drag forces, respectively; the reference wing area S points to the projected area of the model on the xy plane, which is model-dependent because of the serrations and fringes. A marginal difference (1.95%) in the lift-to-drag ratio (Table 2-2) can be observed between the medium and fine grids, which is further confirmed in a comparison of the pressure coefficient (C_p) and the friction coefficient (C_f) on the wing surface, as depicted in Fig. 2-3. Thus, considering the balance between numerical accuracy and computing time, the medium grid was adopted in all the LES simulations.

Table 2-2. Comparison of aerodynamic force coefficients between three grid systems (TE model, *AoA* = 10°, *Re* = 5800).

Parameter	Coarse	Medium (Adopted)	Fine
Mesh number	1.84×10^6	2.9×10^6	3.55×10^6
Time averaged C_l	0.9061	0.9568	0.9621
Time averaged C_d	0.2044	0.2122	0.2088
Time averaged L/D	4.433	4.518	4.608
$\lvert Error_{L/D} \rvert$	3.80%	1.95%	—

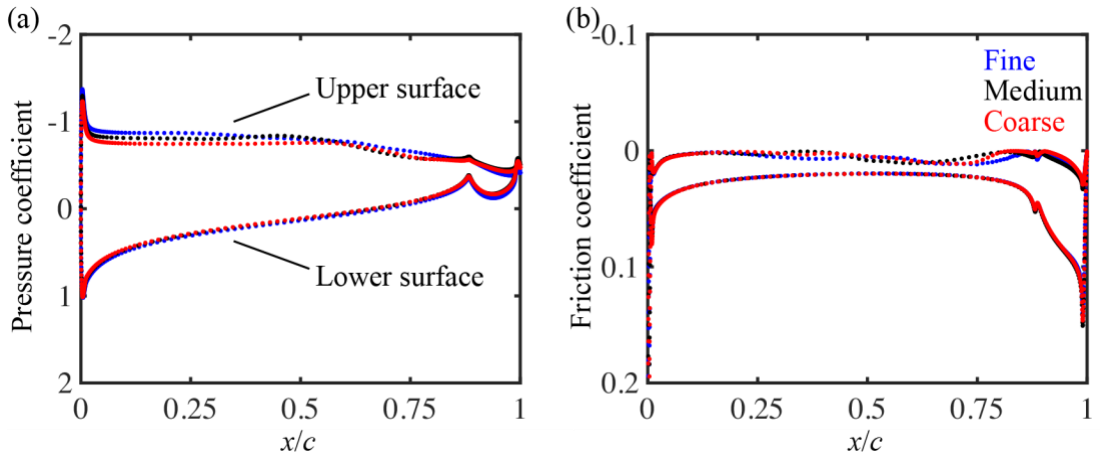

Fig. 2-3. Comparison of (a) pressure coefficients and (b) friction coefficients on wing surface among three grid systems (TE model, *AoA* = 10°, *Re* = 6000).

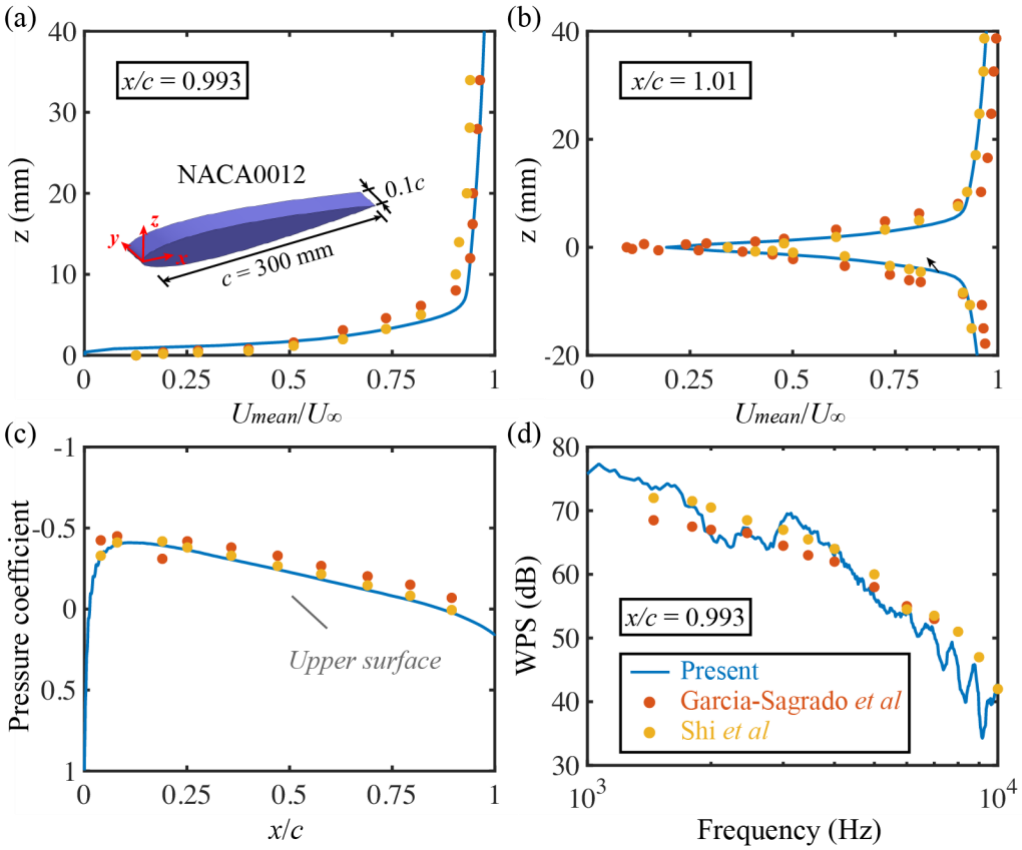

Fig. 2-4. Comparison of mean velocity (U_{mean}) distributions at (a) *x/c* = 0.993 and (b) *x/c* = 1.01, (c) pressure coefficients on the upper surface, and (d) wall pressure spectra at *x/c* = 0.993 for the NACA0012 airfoil (*AoA* = 0°, *Re* = 400,000).

An additional simulation was undertaken of a well-known case (i.e., a NACA0012 airfoil) under the same numerical frame at *Re* = 400,000 and *AoA* = 0° where reliable experimental data are available. The resolved flow characteristics of the airfoil were then compared with experimental measurements by Garcia-Sagrado *et al.* [109] and numerical results (using the open-source CFD software OpenFOAM) by Shi *et al* [49]. As seen in Fig. 2-4, the mean velocity (U_{mean}) distributions in the boundary layer (*x/c* = 0.993) [Fig. 2-4(a)] and wake (*x/c* = 1.01) [Fig. 2-4(b)] and the pressure coefficients on the upper surface [Fig. 2-4(c)] are closely consistent with the experimental (red dots) and numerical (yellow dots) data. In addition, the wall pressure spectrum (WPS) calculated through a fast Fourier transform (FFT) of the pressure time series at *x/c* = 0.993 also matches well the

experimental data [Fig. 2-4(d)], thus verifying that the transient flows can be well captured with the current methods. Note that the WPS is closely associated with the accuracy of far-field acoustic prediction. Moreover, using the same solver (ANSYS Fluent) and spatial discretization schemes, the numerical methods (LES & FW-H) were also verified by Wang *et al.* [19, 53] and Li *et al.* [37] to accurately capture the aeroacoustic characteristics of owl-inspired wing models.

2.3 Effects of TE fringes on aeroacoustic performance

2.3.1 Aerodynamic performance

First, we examine the effect of TE fringes on aerodynamic force production and performance. In Fig. 2-5, the time-averaged aerodynamic coefficients comprising lift coefficients, drag coefficients, and lift-to-drag ratios of the four owl-inspired wing models (CW, TE, LE, and LT models) are compared at various *AoA*s. Both the lift and drag coefficients [Figs. 2-5(a), 2-5(b)] increase monotonously with increasing *AoA* (0–15°), whereas the lift-to-drag ratios [Fig. 2-5(c)] decrease when the *AoA* is greater than 5°. Noticeable differences are observed among the four wing models: the TE model gives similar results to the CW model, but the lift and drag force production is significantly lower in both the LE and LT models, implying that TE fringes have a much smaller impact (side effect) on aerodynamic force production than LE serrations. At low *AoA*s (< 10°), the TE fringe effect results in a slight reduction in the lift coefficient, and hence the lift-to-drag ratio, in the TE and LT models compared with the CW and LE models without TE fringes [Fig. 2-5(c)]. At high *AoA*s (> 10°) noticeable lift reductions are observed in the TE and LT models [see the purple dashed circle in Fig. 2-5(a)]. Because the drag coefficients also exhibit a significant reduction at high *AoA*s (> 10°), the lift-to-drag ratios of the four owl-inspired models reach some convergent value at the highest *AoA* of 15°. Note that the flat plate models are investigated in this study at a relatively low *Re* identical to owl flight, the TE fringes were also found capable of sustaining comparable [37] or even improved [52] aerodynamic performance at high *Re*s [$o(10^5)$~$o(10^6)$].

In addition, as illustrated in Fig. 2-5(c), validation of the LES-based simulations was

further confirmed for the CW and LE models over a range of *AoA*s (0–15°) by comparing the lift-to-drag ratios with the measurements from our previous study [59] [dots in Fig. 2-5(c)]. The results are in good agreement, particularly at relatively high *AoA*s, even though a slight difference in wing thickness exists in the wing models of the experiments (0.5 mm) and the CFD modeling (0.67 mm).

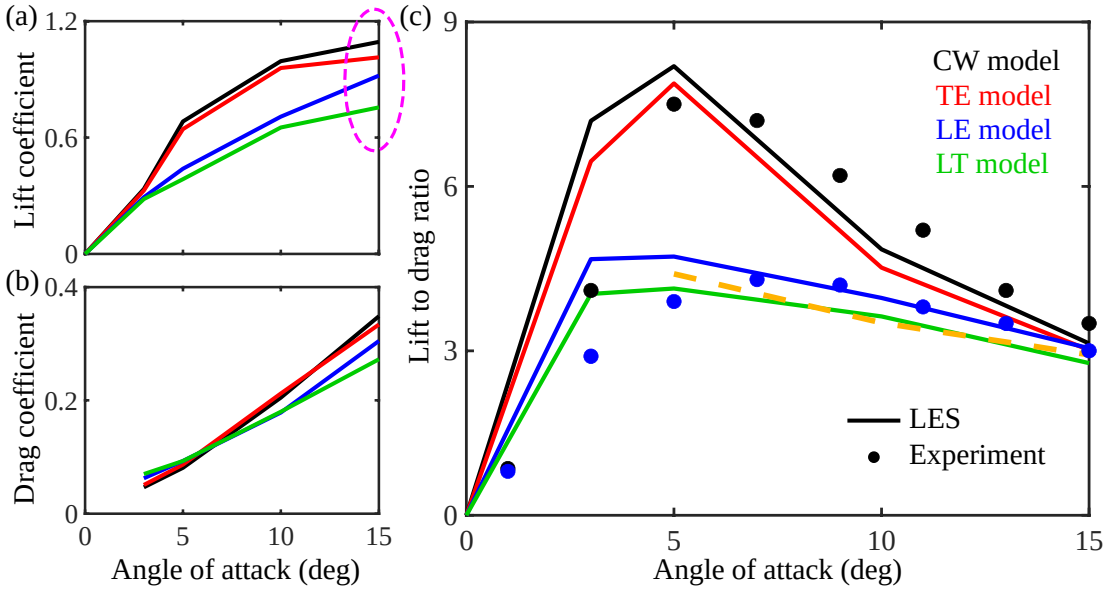

Fig. 2-5. Comparison of (a) lift coefficients, (b) drag coefficients, and (c) lift-to-drag ratios vs *AoA*s among CW model, TE model, LE model, and LT model. The yellow dashed line is based on the formula $L/D_{CW} - (L/D_{CW} - L/D_{LE}) - (L/D_{CW} - L/D_{TE})$. The filled circles denote previous experimental results [59].

To elucidate the aerodynamic mechanisms associated with the TE fringe effect, we further investigate the distribution of pressure coefficients on the wing surface at *AoA*s of 5° [Fig. 2-6(a)] and 15° [Fig. 2-6(b)]. At the 5° *AoA*, there is only a marginal difference between the TE-fringed and non-TE-fringed models, corresponding to the slight reduction in lift coefficient [Fig. 2-5(a)], whereas at the high *AoA* of 15°, a remarkable discrepancy is observed in the middle and downstream of the upper suction surfaces, indicating that the flow structures near the TE are altered by the fringes. As almost the same pressure coefficients are distributed over the lower pressure surfaces, the negative pressures on the upper suction surface, particularly near the TE, is largely reduced, resulting in a lift

reduction [see the purple dashed circle in Fig. 2-5(a)]. The TE fringe effect on aerodynamic force production will be discussed extensively in Sec. 2.4 in combination with visualized vortex structures.

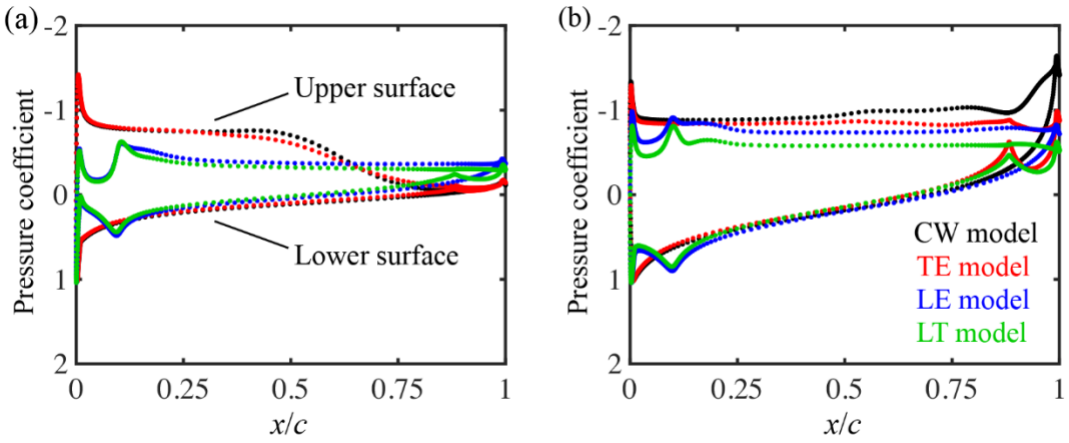

Fig. 2-6. Pressure coefficient distributions on upper and lower wing surfaces of CW model, TE model, LE model, and LT model at *AoA*s of (a) 5° and (b) 15°.

For comparison, the LE serration effect on aerodynamic performance is reconfirmed here. As reported by Rao *et al.* [59], the lift-to-drag ratios of the wing models with and without LE serrations are comparable at *AoA*s above 15°, but are significantly different at low *AoA*s, particularly less than 5° [Fig. 2-5(c)]. This is supported by the pressure distributions shown in Fig. 2-6: the LE serrations obviously reduce the negative pressure peaks, i.e., the LE suction at a low *AoA* of 5°, resulting in a large reduction in lift coefficients, whereas at a high *AoA* of 15°, large pressure differences between the upper and lower surfaces are observed at the LE in all of the wing models. Additionally, the LT model with both LE serrations and TE fringes seems to share the aerodynamic effects of both TE fringes and LE serrations in terms of lift and drag coefficients and the lift-to-drag ratio over a range of 0°~15° (Fig. 2-5): lowering the low-*AoA* aerodynamic performance (LE serration effect) while sustaining comparable aerodynamic performance compared to non-fringed model (TE fringe effect).

2.3.2 Acoustic characteristics

The far-field acoustic characteristics of the four wing models and the effect of TE

fringes on the acoustics are now analyzed through an extensive investigation of the overall sound pressure level (OASPL) distributions and sound spectra. Based on the transient sound pressure fields of the owl-inspired wing models predicted by the FW-H analogy, the sound pressure spectrum at an acoustic receiver can be calculated by performing an FFT on the sound pressure time series of the receiver with a reference sound pressure of 2×10^{-5} Pa. The upper frequency of the sound spectrum, determined by the data sampling interval, is 10 kHz. Substantially, the OASPL at the receiver can be calculated through integrating over the entire frequency range of the sound spectrum (i.e., 0~10 kHz).

We defined 12 acoustic receivers, as depicted in Fig. 2-7, which are distributed evenly in the *xz*-plane at a distance of 10*c* away from the center of the owl-inspired wing model. Receiver 1 (R1) is aligned with the *x*-axis (chordwise direction) and receiver 4 (R4) points in the negative direction of the *z*-axis, perpendicular to the wing wall.

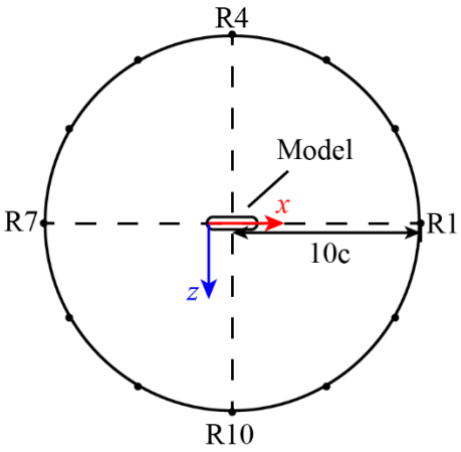

Fig. 2-7. Illustration of 12 acoustic receivers in *xz*-plane.

The OASPL distributions of the four wing models are compared in Fig. 2-8 at three *AoA*s and visualized in an intuitive way to quantify the far-field acoustic characteristics. Given that the pressure fluctuations are regarded as the dominant sound source, the OASPL-based sound source directivity of all models obviously exhibits a dipole feature: the OASPLs have maxima at receivers R4 and R10, indicating that the sound tends to propagate upward and downward; the OASPLs increase with increasing *AoA*, as reported by Zhu *et al.* [21] Compared with the CW model, the TE model presents lower OASPLs at all *AoA*s (e.g., 2.6 dB on average at *AoA* = 15°), which are supported by the experimental

results by Celik *et al*. [47] (2-4 dB) and Gruber *et al*. [29] (2 dB) even given the difference in geometric characteristics and Reynolds numbers; while the LE model exhibits lower OASPLs, particularly at *AoA*s above 10° [Figs. 2-8(b), 2-8(c)], but a slight increase at the low *AoA* of 5° [Fig. 2-8(a)]; the LT model benefits largely from the interplay between TE fringes and LE serrations, achieving a remarkable reduction in OASPLs at all *AoA*s. This indicates that the TE fringes are a robust device capable of achieving sound reduction over a broad range of *AoA*s, independent of clean or serrated LEs, and the combination of TE fringes and LE serrations observed in owl wings may provide a robust and powerful sound suppression design. The effect of the fringe density is also examined through a comparison of acoustic characteristics among the TE model and additional TEn3 (red dotted line) and TEn5 (red dashed line) models. The TEn3 model includes just three fringes with a width of 0.5 mm, a fringe-to-fringe interval of 1 mm, and the same fringe length as in the TE model, while the TEn5 model includes five fringes with a width of 0.3 mm, a fringe-to-fringe interval of 0.6 mm, and also the same fringe length. As shown in Fig. 2-8(c), the fringe density effect is marginal, with only a slight discrepancy adjacent to receivers R1 and R7, again indicating the acoustic robustness of the TE fringes.

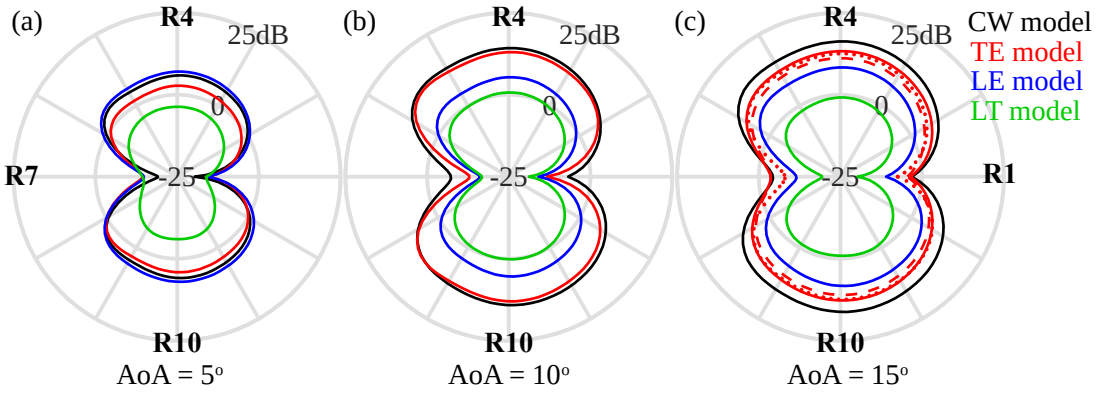

Fig. 2-8. Comparison of OASPL distributions among CW model, TE model, LE model, and LT model at *AoA*s of (a) 5°, (b) 10°, and (c) 15°. The red dotted line and red dashed line represent the results of models TEn3 (with three TE fringes) and TEn5 (with five TE fringes), respectively.

The TE fringe effect is further investigated through sound spectrum analysis, which is conducted by applying an FFT to the sound pressure time series. Given that receivers R4

and R10 display more significant sound reductions, we focus on the sound spectra at R4, as illustrated in Fig. 2-9. The spectra at low and high *AoA*s exhibit noticeably different characteristics particularly at high frequencies, for instance, the sound spectrum at *AoA* of 5° is much flatter than that at high *AoA*s. This may be attributed to the comparatively complex flow interaction at high *AoA*s (see Fig. 2-15), which can induce plenty of small eddies with various scales. At all *AoA*s, however, a remarkable sound reduction is detected at relatively high frequencies ($f > 1$ kHz) for the TE model. This is well consistent with the results of flyover measurements in association with real owls by Sarradj *et al.* [3] and Gruschka *et al.* [1], and the wind tunnel experiments with artificial fringed models by Celik *et al.* [47] and Zhou *et al.* [36] Because high-frequency sound sources normally correspond to large-scale shedding vortices [59], it is reasonable to consider that the TE fringes could work as a flow control device in suppressing the large-scale vortex shedding and flow separation in the vicinity of the TE (see Figs. 2-10, 2-11, and 2-12). It is worth noting that a strong tonal noise is observed in TE model, particularly at *AoA* of 15°. As also reported by Moreau *et al.* [42] in a wing model with narrow fringes, the tonal noise may be owing to the trailing-edge bluntness [25] and the fringe-induced acoustic feedback loop [46].

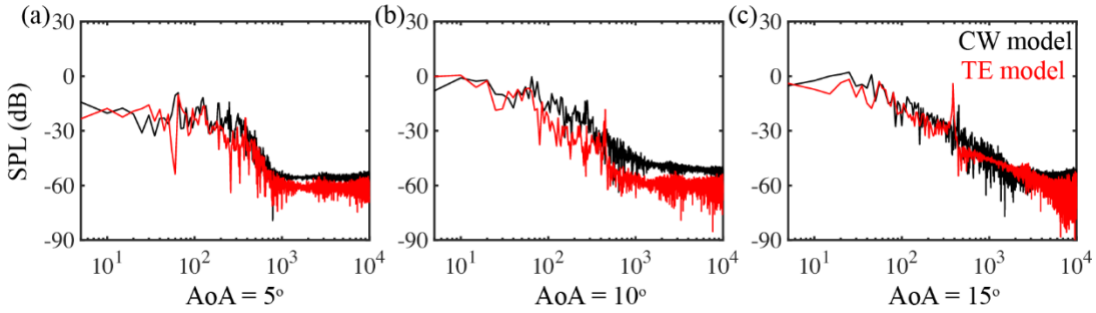

Fig. 2-9. Sound spectra at R4 of CW model and TE model at *AoA*s of (a) 5°, (b) 10°, and (c) 15°.

2.4 Aeroacoustic mechanisms of owl-inspired TE fringes

To elucidate the aeroacoustic mechanisms of the owl-inspired TE fringes on sound reduction, an integrated analysis is now undertaken regarding the near-field flow structures in terms of their velocity and vorticity distributions and the velocity spectra. In Fig. 2-10,

the streamwise flow structures are visualized in terms of the LES-based, normalized time-averaged chordwise velocity contours of the four wing models at low and high *AoA*s. As aeroacoustic noise is closely associated with turbulent fluctuations [25], the fluctuations of the streamwise and wall-normal velocities are further plotted in Figs. 2-11 and 2-12. Here, the streamwise and wall-normal velocity fluctuations (T_u and T_w) are defined as

$$T_u = \frac{1}{U_\infty}\mathrm{RMSE}(u), \qquad (2-17)$$

$$T_w = \frac{1}{U_\infty}\mathrm{RMSE}(w), \qquad (2-18)$$

where U_∞ is the freestream velocity and u, w are the streamwise and wall-normal velocity components, respectively. The root mean squared error (RMSE) of the velocities is employed to estimate the fluctuation characteristics, where the velocities are based on the LES results.

As reported by Rao *et al.* [59], the LE serrations are found to play a crucial role in altering the near-field chordwise flow structures from the LE to the downstream suction surface [Figs. 2-10(c), 2-10(g), 2-10(k)], while achieving passive control of the laminar–turbulent transition through the mitigation of flow fluctuations in terms of streamwise and wall-normal velocity fluctuations [Figs. 2-11(c), 2-11(g), 2-11(k); Figs. 2-12(c), 2-12(g), 2-12(k)]. Consequently, the LE model also exhibits distinguished flow structures from the CW model [Figs. 2-10(a), 2-10(e), 2-10(i)] in the vicinity of the TE in terms of flow separation (Fig. 2-10), velocity fluctuations (Figs. 2-11, 2-12), and near-field flow structures at all *AoA*s. As the far-field sound levels are closely associated with near-field flow fields, this leads to significant sound suppression (Fig. 2-8), particularly at high *AoA*s, whereas a tradeoff is also observed between aerodynamic force production and sound reduction (Fig. 2-5). However, as illustrated in Fig. 2-8(a), the LE serrations cause a slight increase in OASPL at the low *AoA* of 5°. This is probably because the fluctuations at the TE and in the wake turn out to be enhanced [Fig. 2-12(c)], even though the turbulent fluctuations from the LE to the downstream suction surface are suppressed.

Comparatively, the TE fringes seem to alter the flow structures from the TE to the upstream mid-suction surface at all *AoA*s, resulting in marginal variations of the chordwise velocities at the LE [Figs. 2-10(b), 2-10(f), 2-10(j)], while significantly suppressing the streamwise and wall-normal velocity fluctuations at the TE [Figs. 2-11(b), 2-11(f), 2-11(j);

Figs. 2-12(b), 2-12(f), 2-12(j)]. Thus, as depicted in Figs. 2-5 and 2-6, the TE model enables an equivalent pressure distribution, and hence lift and drag coefficients and lift-to-drag ratio, compared with the CW model. Additionally, the TE fringes significantly adjust the local flow structures in the vicinity of the TE, suppressing both streamwise [Figs. 2-11(b), 2-11(f), 2-11(j)] and wall-normal [Figs. 2-12(b), 2-12(f), 2-12(j)] velocity fluctuations and hence lowering the far-field OASPL (Fig. 2-8). This indicates that the TE fringes do not lower aerodynamic performance while achieving sound reduction (Fig. 2-8), and thus the tradeoff associated with LE serrations does not exist here.

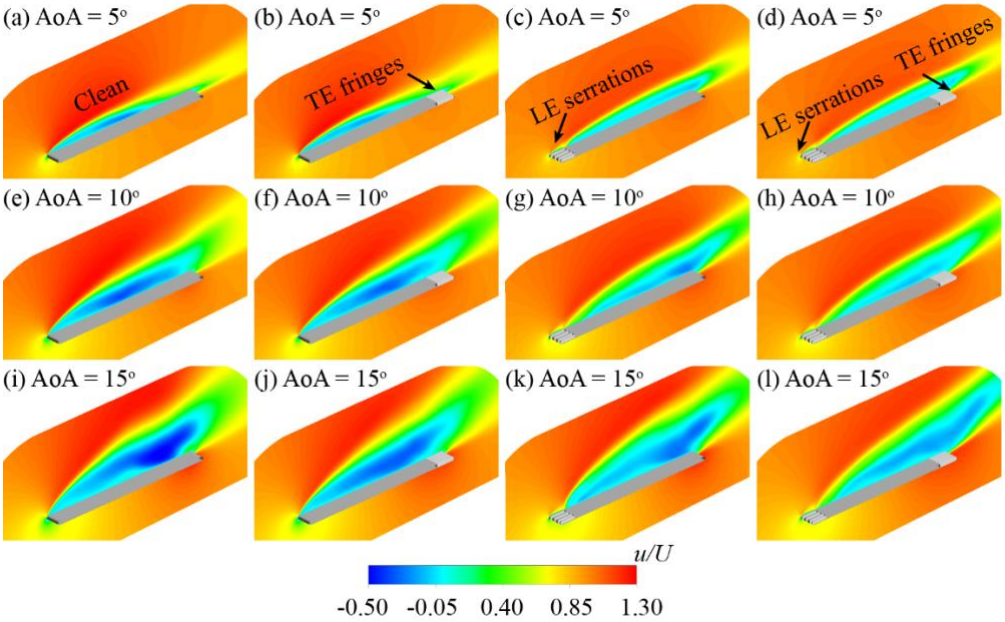

Fig. 2-10. Contours of time-averaged chordwise velocity normalized by freestream velocity U_∞ around (a, e, i) CW model, (b, f, j) TE model, (c, g, k) LE model, and (d, h, l) LT model at *AoA*s of 5°, 10°, and 15°, respectively.

Moreover, it is interesting to observe that the combination of LE serrations and TE fringes produces a synergetic effect on stabilizing the chordwise velocities [Figs. 2-10(d), 2-10(h), 2-10(l)] as well as the streamwise and wall-normal velocity fluctuations [Figs. 2-11(d), 2-11(h), 2-11(l); Figs. 2-12(d), 2-12(h), 2-12(l)] over the entire suction surface while achieving remarkable sound reduction at all *AoA*s (Fig. 2-8). While the LE serrations-based tradeoff is still observed between aerodynamic performance and sound

reduction, the interplay between LE serrations and TE fringes effectively enhances the aeroacoustic noise suppression over a broad range of *AoA*s. Such a phenomenon was also reported by Wang *et al.* [87], where a wavy LE and a cogged TE (Re = 2.88×10^6) were combined.

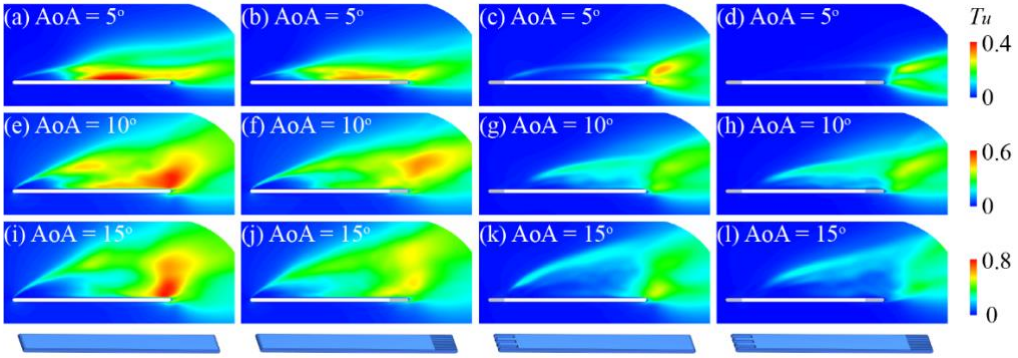

Fig. 2-11. Contours of streamwise velocity fluctuations T_u around (a, e, i) CW model, (b, f, j) TE model, (c, g, k) LE model, and (d, h, l) LT model at *AoA*s of 5°, 10°, and 15°, respectively.

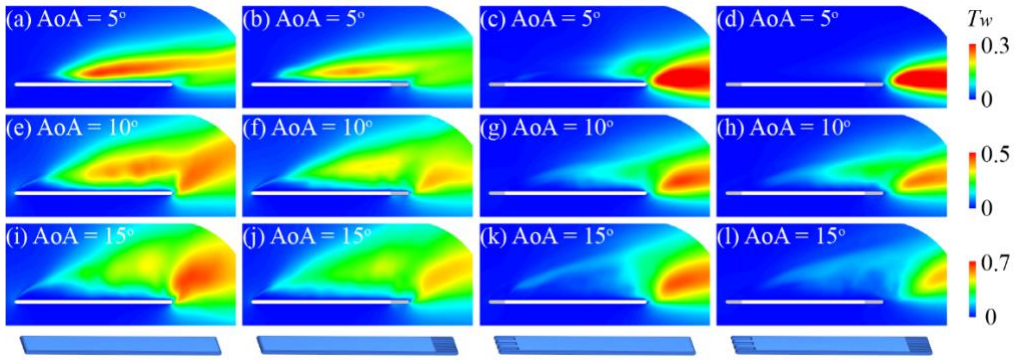

Fig. 2-12. Contours of wall-normal velocity fluctuations T_w around (a, e, i) CW model, (b, f, j) TE model, (c, g, k) LE model, and (d, h, l) LT model at *AoA*s of 5°, 10°, and 15°, respectively.

We further visualize the near-field vortex flow structures at the high *AoA* of 15° by plotting the instantaneous iso-surface of the Q criterion (Fig. 2-13) to identify the swirling features of laminar–turbulent transition while investigating the shear layer-induced flow instability. Here, the Q criterion is normalized by the chord length (c) and freestream velocity (U_∞) as

$$\text{Normalized } Q = \frac{Qc^2}{{U_\infty}^2}, \qquad (2-19)$$

and is highlighted in Fig. 2-13 in terms of the normalized helicity of streamwise vorticity ($(\omega_x c)/U_\infty$).

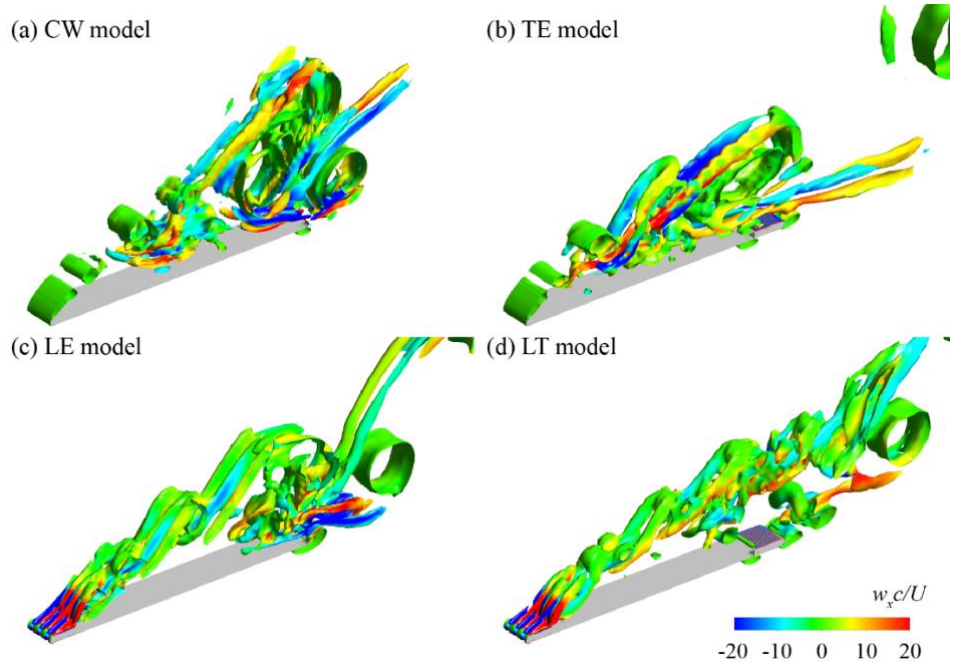

Fig. 2-13. Instantaneous iso-surfaces of normalized swirling strength, Q = 25, highlighted by normalized helicity density of chordwise vorticity at *AoA* = 15°: (a) CW model, (b) TE model, (c) LE model, and (d) LT model.

For the TE and CW models, intense vortex shedding can be observed at the mid-wing chord due to the Kelvin–Helmholtz instability [110] [Figs. 2-13(a), 2-13(b)], which results in intense flow fluctuations at the TE. The shedding vortices then interact with TE vortices, rolling away into the wake. The LE serrations, however, result in the LE vortex breaking up into relatively small eddies [Figs. 2-13(c), 2-13(d)], substantially scattering and mitigating the Kelvin–Helmholtz instability and enhancing the stability of the suction flow [19]. The TE fringes effectively suppress the flow separation and vortex shedding at the TE while passively adjusting the interaction between the LE-induced vortex, the separated shear layer, and the TE vortex [Figs. 2-13(b), 2-13(d)]. This leads to a remarkable reduction in vortex shedding [34, 35], and thus velocity fluctuations in the wake, while significantly suppressing the OASPL (Fig. 2-8) and the high-frequency noise (Fig. 2-9). Furthermore, the nonlinear aeroacoustic interplay between LE serrations and TE fringes, as

observed in the LT model [Fig. 2-13(d)] likely facilitates and stabilizes the interaction between the shed vortices and the TE vortices (Figs. 2-11, 2-12).

To clarify how the local flow structures induced by the TE fringes produce reductions in the velocity fluctuations and suppress the sound, we further investigate the velocity spectra at a specific point at the TE [point 1 in Fig. 2-14(a)]. The velocity spectra are obtained based on FFT analysis of the LES-based time-varying velocities and are compared between the CW model and TE model [Fig. 2-14(b)] and between the LE model and LT model [Fig. 2-14(c)]. Apparently, the TE fringes largely reduce the magnitude of the dominant frequency, which is then remarkedly enhanced in the LT model, where the interplay between LE serrations and TE fringes substantially suppresses the dominant frequencies to a much lower level over a broad range.

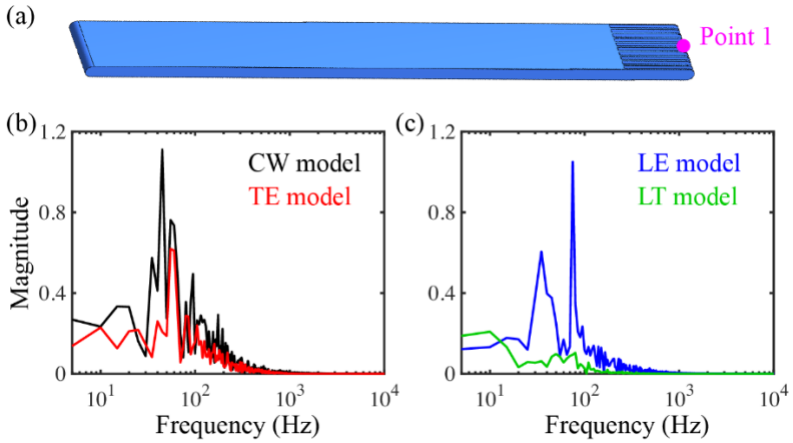

Fig. 2-14. Velocity spectra at (a) observation point 1 for (b) CW model and TE model and for (c) LE model and LT model at AoA of 15°.

The three-dimensional features of the local velocity fields at the TE are now analyzed by comparing the contours of normalized time-averaged wall-normal (Fig. 2-15) and spanwise (Fig. 2-16) velocities between the CW model and TE model at *AoA*s of 5°, 10°, and 15°. Note that the velocity component $-w$ in Fig. 2-15 represents the positive normal velocity from lower to upper surface. At the low *AoA* of 5°, very limited and low-speed flows [Figs. 2-15(a), 2-15(b)] pass through the fringes, whereas at high *AoA*s of 10° and 15°, the large momentum of high-speed flows [Figs. 2-15(c), 2-15(d), 2-15(e), and 2-15(f)] penetrates the fringes from the pressure surface, interacting with the shed LE and TE

vortices while significantly suppressing the local flow fluctuations (Fig. 2-13). Thus, the TE fringes are much more effective in terms of aeroacoustic sound reduction at high *AoA*s (Fig. 2-8). The flow-penetration, as also observed by Avallone *et al*. [33] in a TE-serrated airfoil even at zero *AoA* with a much larger fringe-to-fringe interval, can lead to altering the separated shear layer at TE [31] and hence the TE flow characteristics significantly (Figs. 2-10, 2-11, 2-12).

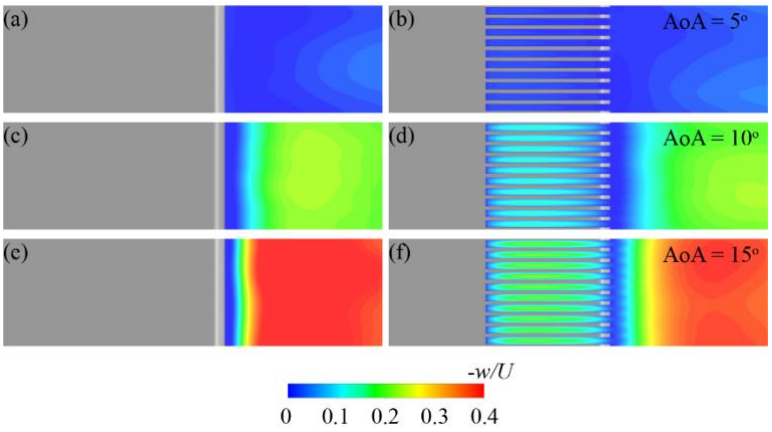

Fig. 2-15. Contours of normalized wall-normal velocity (time-averaged) in (a, c, e) CW model and (b, d, f) TE model in the vicinity of the TE at *AoA*s of (a, b) 5°, (c, d) 10°, and (e, f) 15°.

The TE fringes also influence the spanwise flow structures (velocity component *v* and vorticity), as illustrated in Fig. 2-16, particularly at high *AoA*s of 10° and 15°. For the CW model, the flow instability-induced spanwise vortices lead to alternating spanwise velocities [Figs. 2-16(a), 2-16(c), 2-16(e)] near the TE. For the TE model, the spanwise velocities in the wake are largely suppressed by the TE fringes and alternate substantially at the adjacent fringes [Figs. 2-16(b), 2-16(d), 2-16(f)]. We can infer that this is mainly responsible for breaking up the large-scale TE vortices [37] and hence reducing the sound in association with the TE fringes [30]. This phenomenon is further confirmed by examining the time-averaged streamwise vorticities [Fig. 2-16(h)] along edge line 1 of the TE [Fig. 2-16(g)], implying that the TE fringes are capable of passively facilitating the flow control and stabilization in both the streamwise and spanwise directions.

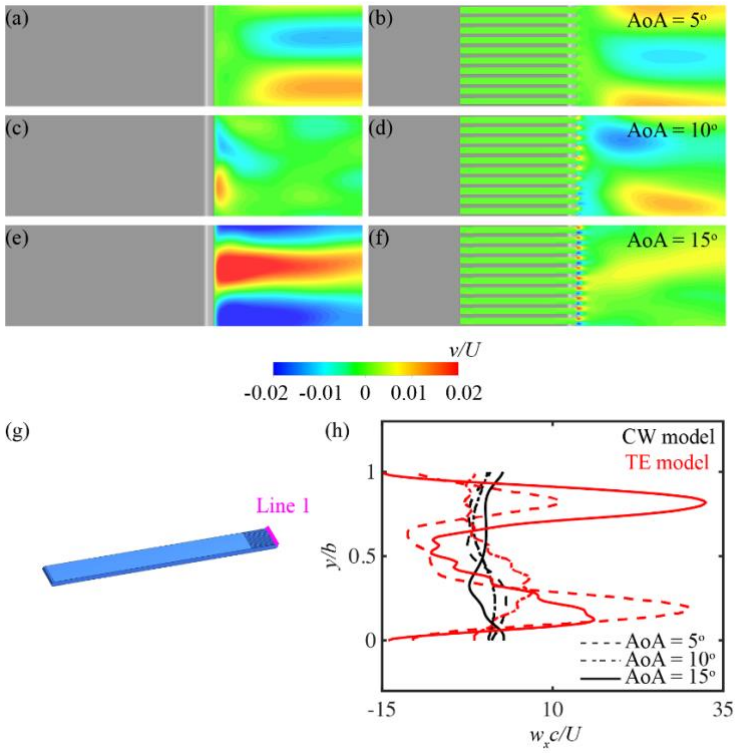

Fig. 2-16. Contours of normalized spanwise velocity (time-averaged) of (a, c, e) CW model and (b, d, f) TE model in the vicinity of the TE at *AoA*s of (a, b) 5°, (c, d) 10°, and (e, f) 15°. (g) Line 1 at the TE. (h) Normalized streamwise vorticity (time-averaged) of CW model and TE model along line 1 at *AoA*s of 5°, 10°, and 15°.

In summary, the possible aeroacoustic mechanisms of owl-inspired TE fringes may be summarized as follows: (1) the fringes bypass and filter the pressure surface flow and facilitate the interaction with the LE-induced vortices on the suction surface, resulting in suppression of the local flow fluctuations and hence the far-field OASPL; (2) the TE fringes alter the spanwise flow characteristics, thus suppressing the large-scale TE vortices. Note that infinite-span models with translational periodic boundary conditions have been utilized in the present study, and thus the spanwise flow structures may not be predicted precisely. This will be extensively investigated and discussed in chapter 3.

2.5 Aeroacoustic interaction between TE fringes and LE serrations

As discussed above, the TE fringes achieve pronounced aeroacoustic sound suppression at all *AoA*s (e.g., 2.6 dB at *AoA* = 15°) with almost no penalty in aerodynamic performance; the LE serrations produce remarkable sound reduction, particularly at high *AoA*s (e.g., 7.9 dB at *AoA* = 15°), but with a cost in terms of the tradeoff between sound reduction and aerodynamic performance. The combination of TE fringes and LE serrations exhibits a nonlinear synergetic effect, dramatically reducing the aeroacoustic levels at all *AoA*s [e.g., 16.7 dB at *AoA* = 15°; Fig. 2-8(c)]. Here, we further examine the underlying mechanisms associated with the aeroacoustic interplay between TE fringes and LE serrations.

The aerodynamic interaction between LE serrations and TE fringes is first investigated by comparing a linear summation of the separated differences between the CW-LE model and CW-TE model with the lift-to-drag ratios of the LT model, as shown in Fig. 2-5(c) [yellow dashed line defined by $(L/D_{CW} - (L/D_{CW} - L/D_{LE}) - (L/D_{CW} - L/D_{TE})$]. Over *AoA*s of 5°–15°, the aerodynamic interaction is marginal, as can be verified by comparing the pressure distributions of the four models in Fig. 2-6.

Next, we examine the acoustic interaction between LE serrations and TE fringes by analyzing the surface pressure (SP) spectra of the four wing models at an *AoA* of 15° (Fig. 2-17). The SP spectra are calculated with a reference pressure of 2×10^{-5} Pa through FFT analysis of the time-varying pressures on the surface. The SP levels can be employed to evaluate the intensity of pressure fluctuations on the wall surface, which are closely associated with the sound generation [50, 51]. In Fig. 2-17, note that the yellow dashed line represents the results of a linear summation of the separated differences between the CW-LE model and CW-TE model. Overall, this displays a pronounced high SP level compared with the LT model, indicating that, unlike the aerodynamic interaction, the acoustic interaction benefits significantly from the interplay between LE serrations and TE fringes, substantially suppressing both low-frequency sound ($f < 63$ Hz) and high-frequency sound ($f > 1$ kHz).

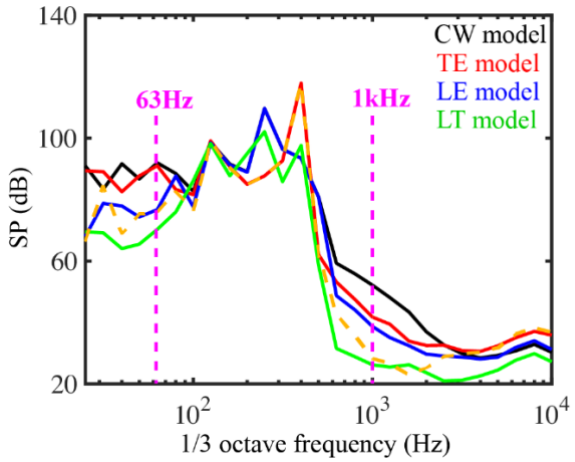

Fig. 2-17. Comparison of SP spectra among four wing models (AoA = 15°). The yellow dashed line is based on the formula $SP_{CW} - (SP_{CW} - SP_{LE}) - (SP_{CW} - SP_{TE})$.

Fig. 2-18 visualizes the SP distributions on the wing surface to describe surface pressure fluctuations at a low frequency (63 Hz) and a high frequency (1 kHz). Interestingly, the SPs at the low frequency share very similar distributions over the entire suction surface for the CW model, TE model, and LE model, whereas the SP levels are significantly reduced in the LT model [Figs. 2-18(a), 2-18(c), 2-18(e), 2-18(g)]. The reason may be that the strong interaction of the shedding and TE vortices is further facilitated in the LT model, and this substantially suppresses the vorticity strength over the suction surface [Fig. 2-13(d)]. Consequently, the vortex-induced suction flow fluctuations are significantly reduced [Figs. 2-11(l), 2-12(l)]. At the high frequency [Figs. 2-18(b), 2-18(d), 2-18(f), 2-18(h)], high-intensity pressure fluctuations appear near the TE in the CW model due to the large-scale vortex shedding [59] [Fig. 2-13(a)]; the TE model noticeably suppresses the fluctuations at the TE [Fig. 2-18(d)]; the LE model provides a large reduction in the high-intensity fluctuations over most portions of the suction surface [Fig. 2-18(f)]; and in the LT model, the high-strength, high-frequency fluctuations dramatically disappear throughout the suction surface.

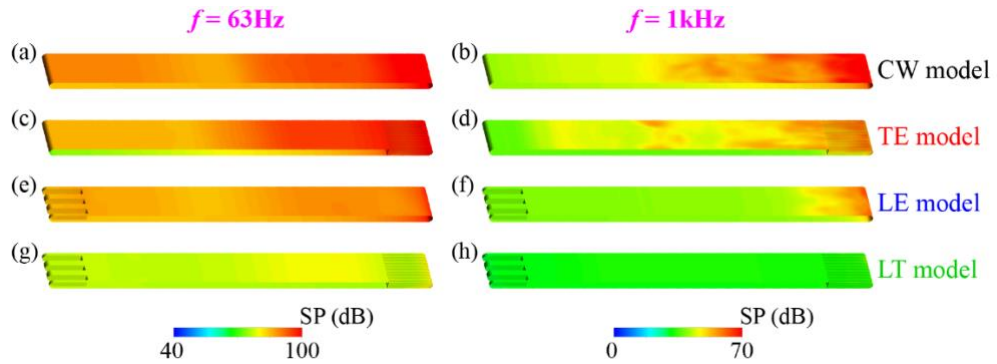

Fig. 2-18. Comparison of SP distributions among four wing models (*AoA* = 15°) at (a, c, e, g) a low frequency of 63 Hz and (b, d, f, h) a high frequency of 1 kHz.

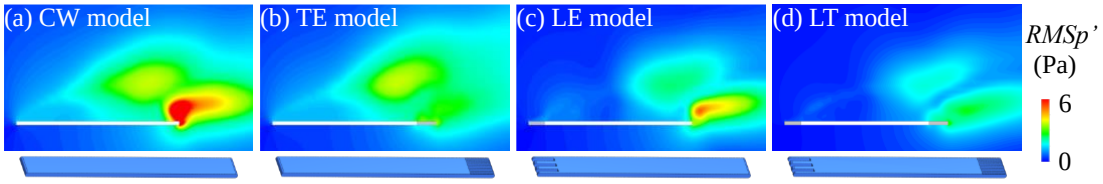

Fig. 2-19. Illustration of pressure fluctuations around (a) CW model, (b) TE model, (c) LE model, and (d) LT model at *AoA* of 15°.

The near-field pressure fluctuations induced by four models are further depicted in Fig. 2-19, which are characterized by the root mean square (RMS) of fluctuated pressures (p') and employed to clarify the impact of the owl-inspired models on sound source fields [19]. The results show that the pressure fluctuations of near-field flows are mitigated by TE fringes [Fig. 2-19(b)] and LE serrations [Fig. 2-19(c)], which turns out to be much more pronounced in the LT model owing to the interplay between LE serrations and TE fringes.

Thus, the aeroacoustic interplay between LE serrations and TE fringes is verified to be capable of effectively suppressing both low- and high-frequency sound without any negative effect on aerodynamic performance. Note that the underlying mechanisms may be affected by 3D flow structures on the upper suction surface, which simultaneously exert some influence on the velocity and pressure fluctuations in both the chordwise and spanwise directions, substantially altering the aeroacoustic characteristics. In this section, infinite models with translational periodic boundary conditions were employed for the sake

of simplicity. More analyses based on 3D simulations are required to further reveal the underlying mechanisms associated with the serrations and fringes.

2.6 Summary

In this section, we describe a numerical study of passive flow control mechanisms and aeroacoustic characteristics in association with four owl-inspired single-feather models, with a special focus on the aeroacoustic interaction between LE serrations and TE fringes. Various aeroacoustic simulations were undertaken by integrating solutions to the LES-based transient flows and the FW-H equation at a low *Re* of 6000. The main findings are summarized as follows:

(1) Owl-inspired TE fringes can achieve pronounced aeroacoustic sound suppression over a range of *AoA*s (5°–15°), e.g., 2.6 dB at *AoA* = 15° at high frequencies of $f > 1$ kHz, with almost no penalty in terms of aerodynamic performance. It has been verified that TE fringes are a more robust sound-reduction device than LE serrations—the latter normally produce remarkable sound reduction at high *AoA*s, e.g., 7.9 dB at *AoA* = 15°, but with a tradeoff in terms of aerodynamic performance [59].

(2) The aeroacoustic mechanism associated with TE fringes involves the fringes effectively bypassing and filtering the flow from the pressure surface. This suppresses the local velocity fluctuations while facilitating the interaction with the LE-induced vortices on the suction surface, significantly reducing the far-field OASPLs. The fringes alter the spanwise flow characteristics at the TE, suppressing the large-scale TE vortices, particularly at high *AoA*s.

(3) The combination of TE fringes and LE serrations produces a nonlinear synergetic effect that dramatically reduces aeroacoustic levels over a range of *AoA*s (5°–15°), e.g., 16.7 dB at *AoA* = 15°. Distinct from the aerodynamic interaction, the acoustic interplay between the LE serrations and TE fringes is capable of suppressing both low-frequency ($f < 63$ Hz) and high-frequency ($f > 1$ kHz) sound.

The results indicate that the TE fringes are a robust sound reduction device for resolving the tradeoff between aerodynamic force production and sound reduction. The owl-inspired wing containing both LE serrations and TE fringes provides a powerful sound

reduction tool for the biomimetic design of various flow machinery, including multirotor drones, helicopters, and wind turbines.

3 Three-dimensional aeroacoustic characteristics of owl-inspired trailing-edge fringes

3.1 Introduction

As natural hunters, owls can achieve silent flight. During flight, high-frequency sound ($f > 1$ kHz) is suppressed to an extremely low level [1-3], which is considered to be a consequence [5, 11, 12, 14] of the unique wing morphologies comprising LE serrations [9, 15-19], TE fringes [20, 21], and a velvety surface [22, 23, 82]. The novel aeroacoustic mechanisms that result in the silent flight of an owl [4, 10, 24] have been explored to provide inspiration for industrial applications [6].

As a typical morphological feature not found on non-silent birds, the TE fringes on the inner vane of owl feathers [20] have been widely investigated with various 2D models and applied as a conceptual biomimetic design for fluid machinery (e.g., airfoils, rotors, and wind turbines) to reduce noise [7, 47, 48]. So far, 2D numerical simulations have mainly been utilized in investigating the aeroacoustic effects of owl-inspired TE fringes based on finite-span models with translational, periodic boundary conditions. In contrast, the 3D aeroacoustic characteristics associated with TE fringes remain yet poorly studied.

This section describes an integrated study of the 3D aeroacoustic characteristics induced by the owl-inspired TE fringes in which we combined LES with the FW-H analogy. We constructed a clean wing model and three wing models with TE fringes that were distributed differently spanwise. The aerodynamic forces and 3D acoustic characteristics are compared between the fringed and clean models so as to reveal the 3D aeroacoustic effects of the TE fringes. Then, the aeroacoustic mechanisms associated with the 3D TE fringes are investigated by visualizing the near-field 3D flow structures, vortex dynamics, and flow fluctuations.

3.2 3D single-feather models with owl-inspired TE fringes

3.2.1 3D single-feather models

Motivated by the meticulous fringes at the TE of a single owl feather [Fig. 3-1(a)], we constructed four 3D models of wings [Fig. 3-1(b)]: a clean wing model (CW plate), a TE-fringed wing model (TE plate), and two wing models with a partially fringed TE (TE-tip plate and TE-mid plate). The models were rectangular and had dimensions of 150 mm × 30 mm. They were selected identical to those used in our previous research [71] with consideration of the consistency in modeling and comparable investigation of the fundamental underlying aeroacoustic characteristics. For simplicity, the camber and thickness variations of the feather were neglected in the owl-inspired 3D wing models. The TE fringe-like structures were distributed uniformly and aligned with the incoming flow with a density close to that of real fringes [Fig. 3-1(c)] [20]. Thus, TE plate had 150 fringes. TE-tip plate and TE-mid plate each had 50 TE fringes, distributed near the wingtip or midspan, respectively. The aim was to assess the effect of TE fringes on the spanwise flows. The basic geometric parameters of the 3D wing models are given in Table 3-1. Additionally, as defined in Fig. 3-1(b), the origin of the coordinate system is at the intersection of the LE and wing root. The *x*- and *y*-axes point in the chordwise and spanwise directions of the models, respectively. The *z*-axis was determined by the right-hand rule and was perpendicular to the upper wing surface.

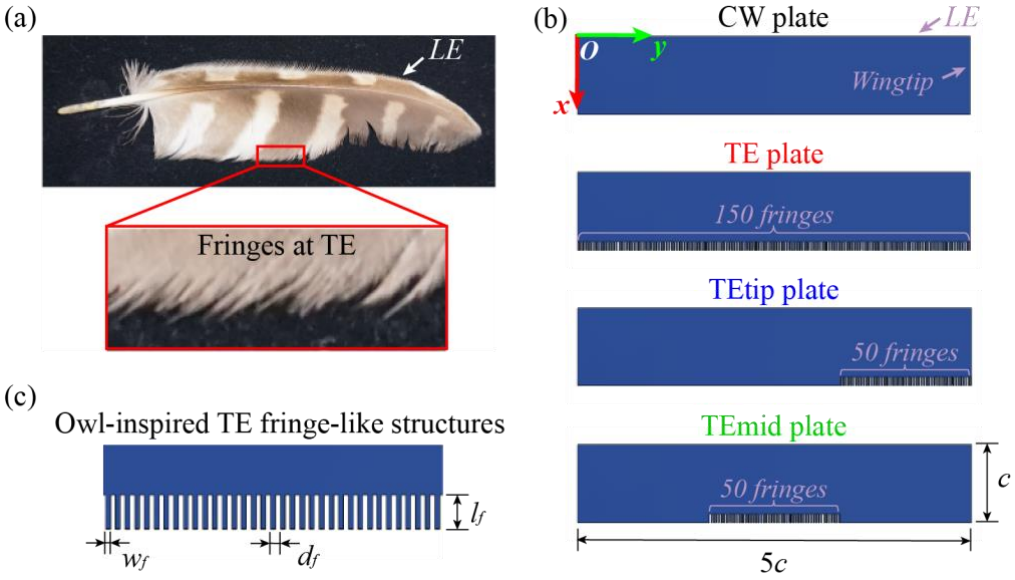

Fig. 3-1. (a) An owl's 10th primary feather showing the fringes on the TE. (b) Four owl-inspired 3D wing models (CW plate: 3D clean wing model; TE plate: 3D TE-fringed wing model; TE-tip plate: 3D wing model with 50 TE fringes near the tip; TE-mid plate: 3D wing model with 50 TE fringes around the midspan). (c) Owl-inspired TE fringe-like structures

Table 3-1. Basic geometric parameters of the 3D computational models.

Parameter	Symbol	Size (mm)
Chord	c	30.0
Span	b	150.0
Thickness	t	0.67
Length of fringes	l_f	3.5
Width of fringes	w_f	0.5
Interval between fringes	d_f	1.0

To resolve the large-scale separated flows and turbulent vortices surrounding the 3D wing models, a hybrid grid system was established with a large number and high density of fringes, as illustrated in Fig. 3-2. High-resolution structured grid elements were employed between the fringes to ensure the accuracy of the near-wall flows around the fringes whereas unstructured elements were generated in other areas. The near-field elements were clustered at the wing surface, especially the TE, to ensure the resolution was high for the separated boundary layers and 3D turbulent vortices (e.g., LE, TE, and wingtip vortices) over the wing surface [Figs. 3-2(b) and 3-2(c)], which are extremely sensitive for the acoustic prediction.

The height of the first layer of the grid adjacent to the surface was given by $\delta = 0.1c/\sqrt{Re}$ [59, 111], where Re denotes the chord length-based Reynolds number, to ensure the dimensionless wall-normal distance was less than 1 (y plus < 1). Because of the low speed of an owl's forward flight (2.5–7.5 m/s) [64], the freestream velocity (U_∞) was taken to be 3 m/s, resulting in Re = 6000 (air density $\rho = 1.225$ kg m^{-3} and air viscosity $\mu = 1.7894 \times 10^{-5}$ kg m^{-1} s^{-1}). The velocity-inlet boundary and the far-field were 10c from the wing surface whereas the pressure-outlet boundary was 20c away to avoid the effects of backflow [Fig. 3-2(a)]. In the spanwise direction, the computational domain extended 10c from the wingtip surface to ensure the reliability of the simulations

[Fig. 3-2(b)]. A symmetric boundary condition was imposed on the surface of the wing root (plane $y = 0$). Furthermore, the *AoA*s were varied from 5° to 15°.

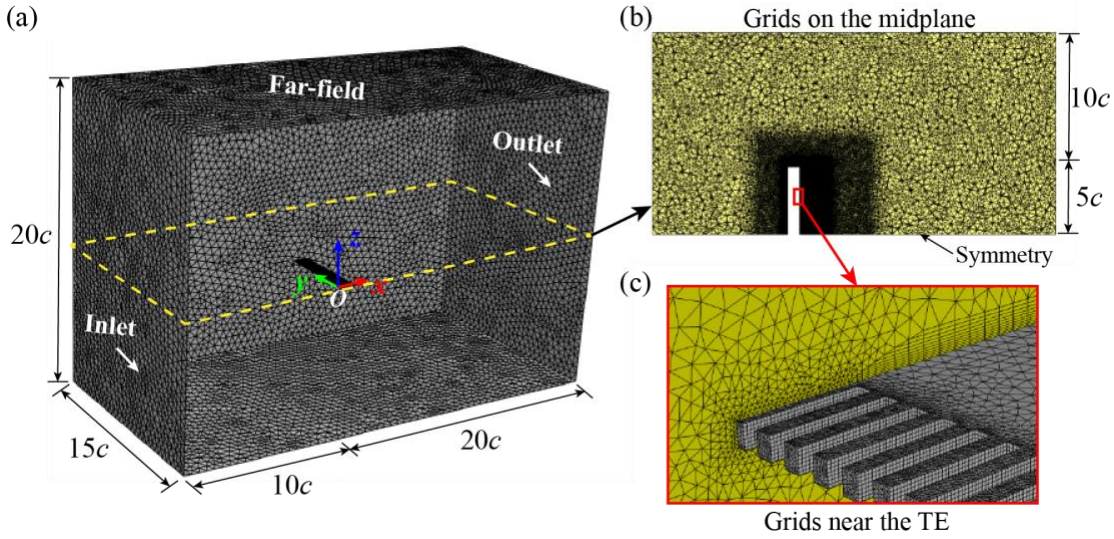

Fig. 3-2 (a) Computational domain and hybrid grid system (structured grid between the fringes and unstructured grid in other domains). (b) Grid elements in the midplane. (c) Grid elements near the fringed TE (from the back)

3.2.2 Numerical settings

Here the 3D flow and acoustic fields induced by the 3D wing models with TE fringes were resolved separately with a loosely coupled approach [112] as described in Sec. 2.2.2. First, the transient flow was computed by the LES method for the wing models. This includes the generation, shedding, and breaking of 3D vortices; separation of the boundary layer; and pressure pulsations. Second, acoustic propagation was predicted with the FW-H equation.

The large eddies induced by the wing models were resolved directly in the LES method by solving the Navier–Stokes (N–S) equations. The eddies with a size smaller than the grid size, which are particularly computationally expensive, were filtered out and processed in a subgrid model of the WALE approach [105], which has been verified to be reliable in the computation of complex turbulent flows [59-61].

The incompressible N–S equations were solved by the pressure-velocity coupling (SIMPLE) algorithm [113]. The least squares cell based scheme was adopted to solve the gradients of variables. The bounded central difference and bounded second-order implicit

schemes were employed respectively to discretize the momentum and transient formulations to enhance simulation stability and reduce numerical dissipation. The value of the subgrid-scale model constant (C_w) was taken to be 0.325. The time step $\Delta t = 5 \times 10^{-5}$ s, which has been verified to satisfy the requirement of the Courant–Friedrichs–Lewy condition (CFL < 1) for the accurate resolution of transient flow fields. The simulations were run for up to 18,000 steps to ensure the flow fields became statistically stable. The instantaneous values from the last 6000 steps of the LES simulations were utilized in post-processing the flow fields and were also input into the acoustic calculations.

With the instantaneous flow information (e.g., pressure pulsations on the wing surface) from the LES, the transient acoustic fields around the 3D wing models were then calculated with the FW-H equation [50, 51]. In the FW-H analogy, the far-field sound is attributed to the superposition of quadrupole, dipole, and monopole acoustic sources. The quadrupole sources are essentially turbulent noise, which is negligible at a low freestream velocity. The dipole and monopole acoustic sources (surface integrals) are induced by transient pressure fluctuations (unsteady aerodynamic forces) and mass movements, respectively. The monopole sources are also ignored here. Thus, the dipole sources (induced by pressure fluctuations) are the dominant sources in this study, and all the wing surfaces are regarded as emission surfaces.

3.2.3 Verification and validation

In Sec. 2.2.3 and our previous studies, LESs of 2D wing models [59, 60, 112] and 3D wing models [61] with LE serrations were verified and validated by systematically comparing the results with data from PIV and force measurements [71]. There was reasonable consistency over a broad range of *AoA*s (0–20°) in terms of time-averaged aerodynamic forces, distributions of time-averaged streamwise velocities and Reynolds stresses. The numerical methods were also verified to be capable of accurately capturing the aeroacoustic features of wing models by running a well-known case of NACA0012 airfoil (Fig. 2-4). Here the simulations of 3D wing models with TE fringes were further

verified with a grid independence analysis and a comparison of aerodynamic forces. Three grid systems with different grid densities were generated for the TE plate, and the time-averaged aerodynamic force coefficients were compared for each grid (Table 3-2).

Table 3-2. Comparison of time-averaged aerodynamic force coefficients for three grid systems (TE plate, *AoA* = 5°, and *Re* = 6000).

Parameter	Coarse	Medium (adopted)	Fine
Number of nodes	1.32×10^7	1.56×10^7	1.93×10^7
Time-averaged C_l	0.4790	0.4782	0.4792
Time-averaged C_d	0.0772	0.0770	0.0769
Time-averaged L/D	6.2028	6.2126	6.2290
$\lvert Error_{L/D} \rvert$	0.42%	0.26%	—

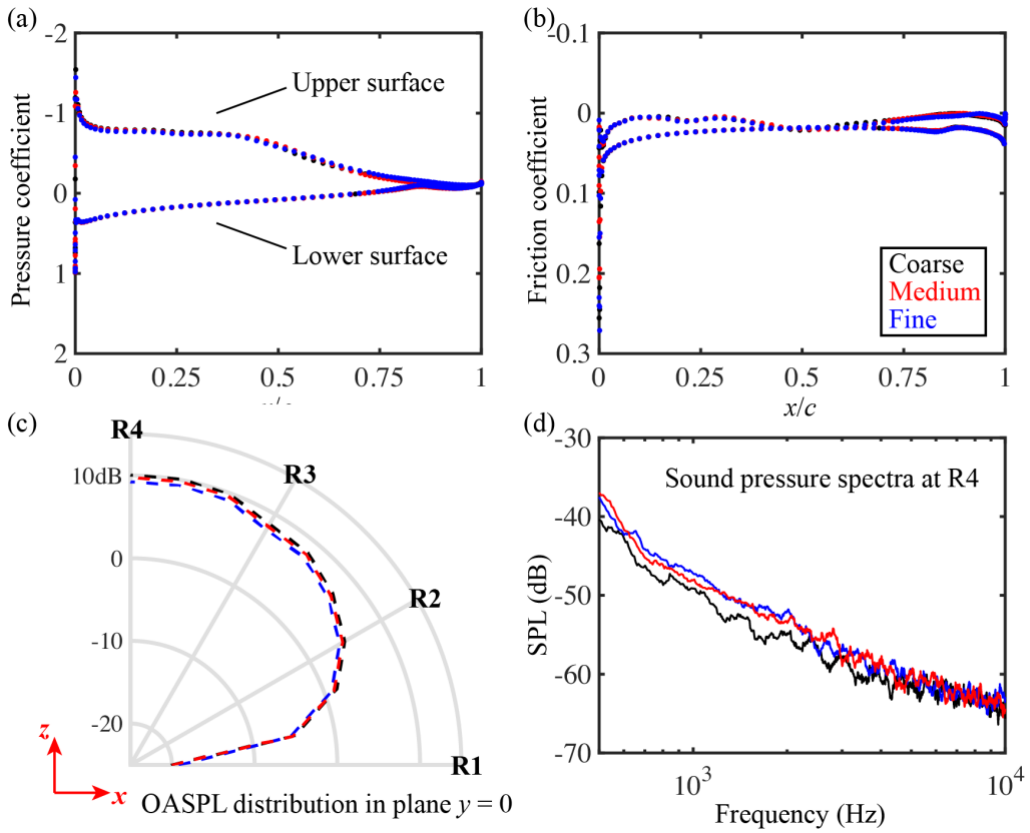

Fig. 3-3. Comparison of time-averaged (a) pressure coefficients and (b) friction coefficients on the wing surface, far-field (c) OASPLs in plane y = 0 and (d) sound pressure spectra at R4 for the three grids (TE plate, *AoA* = 5°, and *Re* = 6000).

As compared in Table 3-2, the difference in L/D between the medium and fine grids is marginal, less than 0.26%. Moreover, there are also marginal differences among the three grids for the time-averaged C_p and C_f on the wing surface, as compared in Figs. 3-3(a) and 3-3(b). The predicted far-field OASPL distributions in the plane y = 0 [Fig. 3-3(c)] and the sound pressure spectra at an acoustic receiver R4 [Fig. 3-3(d)] were also compared among the three grids. Note that the definitions of the OASPL and acoustic receivers (e.g., R1–R4) are described later in Sec. 3.3.2. Thus, the medium grid was chosen for all the aeroacoustic simulations as a compromise between numerical accuracy and computing time.

Furthermore, the computed time-averaged aerodynamic coefficients (C_l, C_d, and L/D) of the CW plate model were compared with the experimental results [59, 71] to validate the 3D LES simulations. As illustrated in Fig. 3-4, both the trends and magnitudes of the simulation results are very consistent with the measurements from 5–15°. Note that the geometric parameters and flow conditions for the LES model and the experimental wing were the same except for the thickness (t).

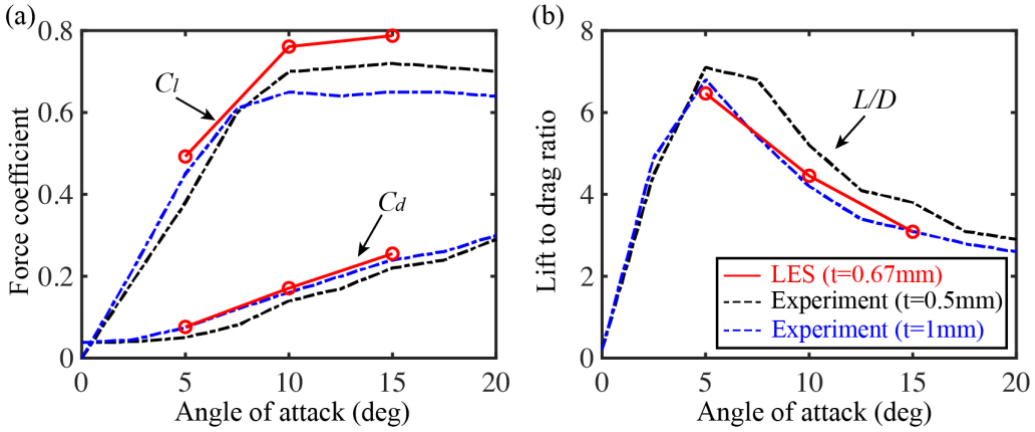

Fig. 3-4. Comparison between LES and experimental results of the time-averaged (a) C_l and C_d and (b) L/D for the CW plate (Re = 6000).

3.3 3D aeroacoustic characteristics induced by TE fringes

3.3.1 Aerodynamic performance

The effect of 3D TE fringes on aerodynamic performance was first examined by

comparing the time-averaged lift and drag force coefficients (C_l and C_d) and lift-to-drag ratios (L/D) of the four owl-inspired 3D models at a high *AoA* of 15°, as depicted in Table 3-3. Overall, the clean wing model (CW plate) and three TE-fringed wing models (TE, TE-tip, and TE-mid plates) had similar aerodynamic performance, which is consistent with our 2D results [112]. There are noticeable differences for the lift coefficients for the four wing models whereas the drag coefficients are nearly the same. Compared to the CW plate, the models with TE fringes have relatively lower lift coefficients and hence, lift-to-drag ratios. The fully fringed model (TE plate) has the lowest lift-to-drag ratio (lower by 7.6% and 0.23 in magnitude compared to the CW plate). Comparatively, the decline in aerodynamic performance is obviously less for the partially fringed models (TE-tip plate: 0.9% and TE-mid plate: 2.2%). In comparison with the low *AoA* of 5° (Table 3-2), the L/D had already fallen for the TE plate model, by 4.2% (0.27 in magnitude). In general, the 3D TE fringes do not distinctly reduce the aerodynamic performance at *AoA*s of 5–15°, regardless of the spanwise distribution. Interestingly, compared to a previous study of a 3D wing model with large TE fringes [44], the measured aerodynamic forces (e.g., the lift coefficients) were much lower, by 10–20%. Thus, we infer that the aerodynamic force production of the present TE wing models very likely benefits from the compact and subtle fringes based on the realistic fringe density at such a moderate Reynolds number.

Table 3-3. Comparison for the CW plate, TE plate, TE-tip plate, and TE-mid plate of the time-averaged C_l, C_d, and L/D (*AoA* = 15°).

3D wing model	C_l	C_d	L/D
CW plate	0.7875	0.2551	3.086
TE plate	0.7234	0.2537	2.852
TE-tip plate	0.7804	0.2552	3.058
TE-mid plate	0.7788	0.2580	3.019

To explore the underlying mechanisms for the effects of TE fringes on the aerodynamic forces in 3D, the time-averaged surface-pressure coefficient (C_p) is plotted for three planes for the four wing models (Fig. 3-5). The C_p distributions were measured along the lines where the upper and lower surfaces of the models intersect three planes at *y*

= 0.25*b* (proximal to the wing root), 0.5*b* (midspan), and 0.75*b* (proximal to the wingtip) [Fig. 3-5(a)]. In the TE-fringed models, planes 1 and 3 are between two fringes whereas plane 2 passes through a fringe.

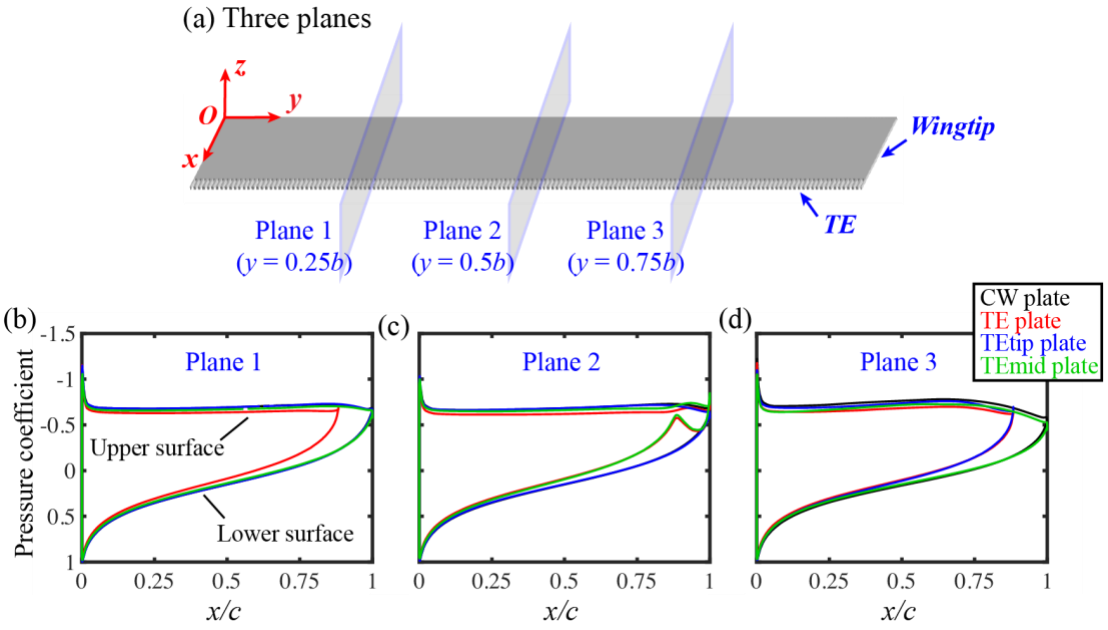

Fig. 3-5. (a) Three planes: plane 1 (y = 0.25b), plane 2 (y = 0.5b), and plane 3 (y = 0.75b). (b)–(d) Surface-pressure coefficients (C_p) for the CW plate, TE plate, TE-tip plate, and TE-mid plate for the three planes (AoA = 15°).

Figures 3-5(b), 3-5(c), and 3-5(d) show that the four wing models have similar C_p distributions from the LE to mid-chord whereas there are noticeable differences from mid-chord to the TE, particularly on the lower surface. Obviously, the TE fringes can significantly affect the near-field flow structures in the vicinity of the TE but exert less impact on the upstream flows. As the aerodynamic performance is mostly dominated by the pressures in the vicinity of LE, the aerodynamic performance of the TE-fringed models is similar with that of the clean model (Table 3-3). In particular, for plane 1 [Fig. 3-5(b)], which is proximal to the wing root, there are marginal differences in C_p for the CW plate, TE-tip plate, and TE-mid plate. In contrast, there is a remarkable reduction near the TE for the TE plate because the plane is in the gap between two fringes and so it has a slightly shorter chord length, which decreases the lift force. The same trends are also observed for

the C_p distributions for plane 3 [Fig. 3-5(d)], which is proximal to the wingtip. For plane 2 [Fig. 3-5(c)], although the four wing models extend for the whole chord length, the fringes also lowered the C_p on the lower surface in the region from mid-chord to the TE and hence, reduced the lift force produced. This indicates that the effect of TE fringes on the near-field flow is essentially 3D. The fringes affect both the local spanwise and chordwise flow structures, as observed in previous studies [30, 49]. We infer that the marginal lift reduction caused by TE fringes is mainly attributed to: (1) the decrease of the chord length and (2) the pressure loss on the lower surface near the TE.

Note that from our previous 2D results [112], the loss of lift is inferred owing to the decrease in the negative pressure on the suction side, whereas here the 3D results indicate that it is mainly attributed to the pressure loss over the lower surface [Figs. 3-5(b), 3-5(c), and 3–5(d)]. Such a noticeable difference between the 2D and 3D simulation results can be attributed to the accurate resolution of the 3D flow structures such as large spanwise vortices. This is discussed in detail in Sec. 3.4, which includes visualizations of the local 3D vortex structures surrounding the fringes.

3.3.2 Acoustic characteristics

Next, we investigate the far-field acoustic characteristics of the owl-inspired 3D wing models with and without TE fringes. The wings are compared in terms of the far-field OASPLs, sound reduction maps, and sound pressure spectra. The transient sound pressure fields around the wing models were resolved with the FW-H equation. Then the sound pressure spectrum at an acoustic receiver could be calculated through an FFT of the sound pressure time series at the receiver. The upper limit frequency for spectral analysis is 10 kHz, and the OASPL at the receiver was computed by integrating over the entire frequency range of 0~10 kHz. The reference sound pressure was taken to be 2×10^{-5} Pa.

To capture the 3D acoustic fields of the wing models, 72 acoustic receivers were defined on a sphere (radius = 15*c*) centered at the origin of the coordinate system. As shown in Fig. 3-6, 12 acoustic receivers were distributed evenly in the plane y = 0 mm, numbered in counterclockwise order (i.e., R1–R12). This circle was then rotated about the *z*-axis by 30° to form six circles in total, each with 12 receivers.

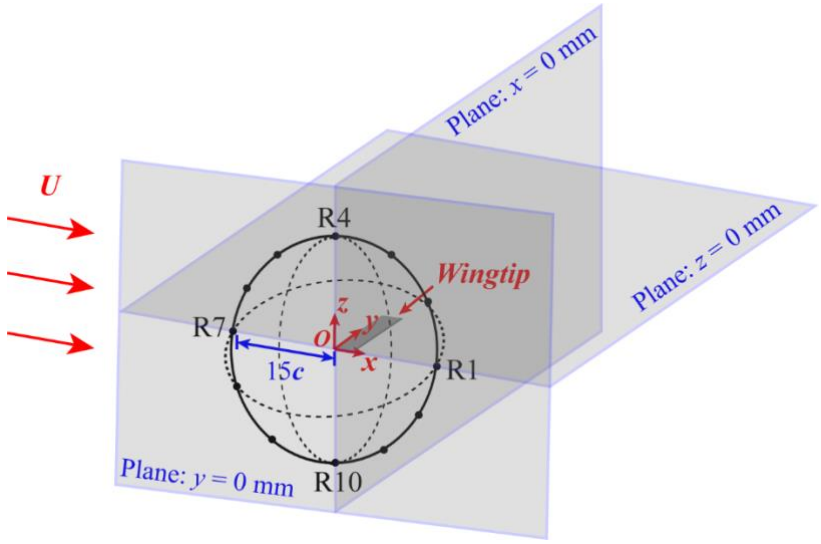

Fig. 3-6. Positions of 72 acoustic receivers on a spherical surface (radius = 15*c*).

The far-field OASPLs were then calculated at the 72 acoustic receivers for the CW plate [Fig. 3-7(a)] and the TE plate [Fig. 3-7(b)] for an *AoA* of 15°. For simplicity, only OASPLs on a hemisphere with positive *y*-coordinates are depicted. The sound pressures induced by the 3D wing models obviously vary in 3D. They tend to propagate upward and downward while exhibiting dipole characteristics. In addition, the OASPLs are distributed approximately symmetrically about the midplane of the wing (*xy*-plane), but have lower values there compared to other places. Compared to the CW plate, the OASPLs were suppressed drastically for the TE plate in most directions, displaying remarkable sound reduction, i.e., the acoustic performance expected for TE fringes.

Figure 3-7(c) is a sound reduction map surrounding the TE plate for an *AoA* of 15° to visualize the ΔOASPL distributions, which were obtained by subtracting the OASPLs of the TE plate from those of the CW plate. Obviously, the reduction in OASPLs throughout the surrounding space is due to the TE fringes, particularly beyond and beneath the wing models, where a remarkable reduction of 5–6 dB can be achieved. The sound reduction map is symmetrical about the *xy*-plane.

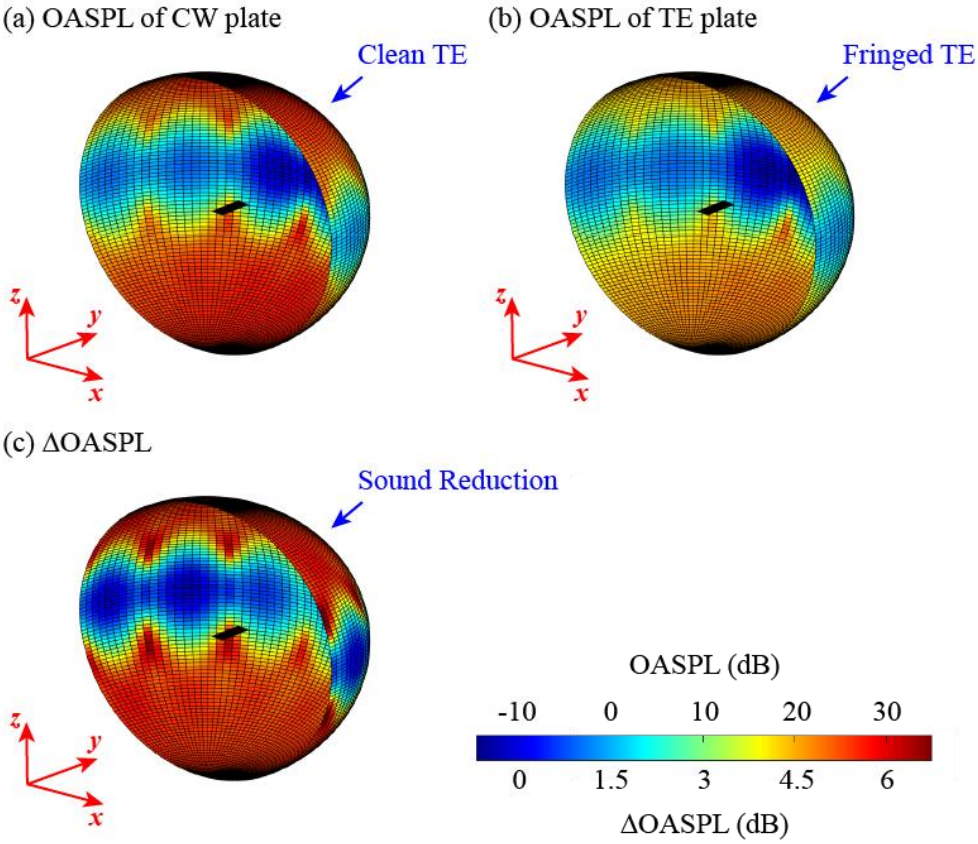

Fig. 3-7. Isocontours of OASPLs for (a) the CW plate and (b) the TE plate. (c) Sound reduction map for the TE plate (*AoA* = 15°).

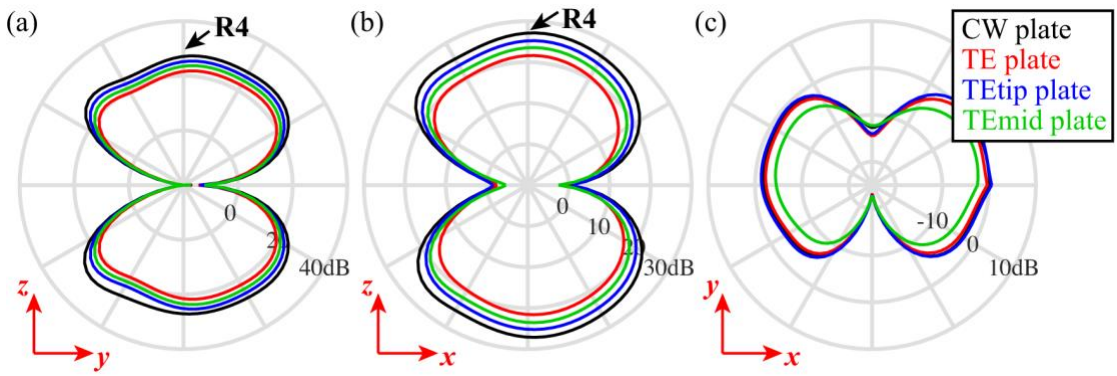

Fig. 3-8. Comparison of OASPL distributions for the CW plate, TE plate, TE-tip plate, and TE-mid plate in three planes: (a) $x = 0$, (b) $y = 0$, and (c) $z = 0$ (*AoA* = 15°).

To visualize the directional characteristics of the sound reduction for the TE plate,

TE-tip plate, and TE-mid plate compared to the CW plate, the OASPL distributions are also plotted in three representative planes: x = 0 mm, y = 0 mm, and z = 0 mm (Fig. 3-8). Together with the iso-contours in Fig. 3-7, we can see that the OASPLs in the three planes have a distinct dipole feature, which is consistent with the results of our previous 2D study [112], indicating that the dominant acoustic sources are caused by near-field pressure fluctuations [50, 51]. For the four wing models, the OASPLs have the same trend and reach a maximum at R4 in the z-direction [Figs. 3-8(a) and 3-8(b)]. All three TE-fringed models achieved a distinct reduction in OASPL and hence, a robust decrease in the sound. The fully fringed TE model (TE plate) had the lowest OASPLs with a reduction of 5.5 dB at R4 compared to that of the CW plate. The sound reduction of this 3D model is remarkable compared to that in our previous 2D results, where a reduction of 2.6 dB was observed for an *AoA* of 15° [112]. This is probably because the near-field 3D flow structures induced by the TE, which have both large spanwise and chordwise vortices, may exert a significant influence on the aeroacoustic characteristics. Comparatively, the TE-tip plate and the TE-mid plate, which have the same number of fringes, have lower reductions in OASPL—1.9 dB and 3.6 dB, respectively—indicating that the acoustic performance may be sensitive to the spanwise distribution of fringes. The midspan fringes obviously achieved better acoustic performance than those proximal to the wingtip.

Given that the OASPL reductions are maxima at R4 (Figs. 3-7 and 3-8), the sound pressure spectra of the four wing models were compared at the receiver. As depicted in Fig. 3-9, over the low-frequency range (purple solid ellipse in Fig. 3-9), there are marginal differences among the four wing models. In contrast, for the high-frequency range (purple dashed ellipse in Fig. 3-9), remarkable sound reduction is observed for all three TE-fringed models. The TE plate was best at suppressing high-frequency sound whereas the TE-tip plate was the worst. These results indicate that as a robust sound reduction device, 3D TE fringes are limited to suppressing high-frequency sound ($f > 1$ kHz), which is consistent with the frequency characteristics of an owl's flyover noise measured by Gruschka *et al.* [1] and Sarradj *et al.* [3] and our 2D numerical results [112]. In addition, an obvious tonal noise is observed for all wing models, which may be the instability noise or the noise induced by the bluntness of the TE of the wing models [25].

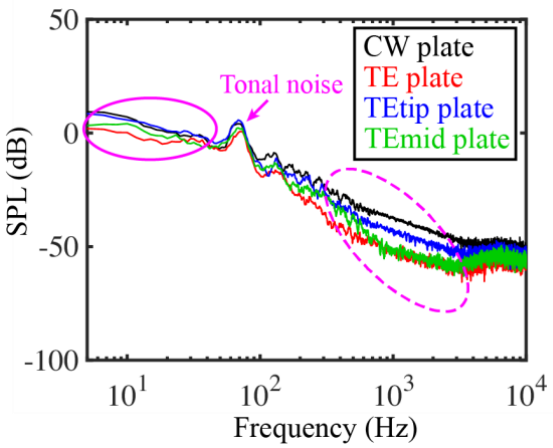

Fig. 3-9. Comparison of sound pressure spectra at R4 for the CW plate, TE plate, TE-tip plate, and TE-mid plate (*AoA* = 15°).

3.4 3D aeroacoustic mechanisms associated with TE fringes

3.4.1 Overview of near-field 3D flow structures

Next, we extensively investigated the aeroacoustic mechanisms of the owl-inspired TE fringes on the aerodynamic force produced and the sound reduction by visualizing the near-field flow structures, 3D turbulent vortices (e.g., LE, TE, and wingtip vortices), and flow fluctuations [e.g., turbulence kinetic energy (TKE) distributions].

Figure 3-10 visualizes the contours of the time-averaged chordwise velocity around the CW plate and TE plate in three planes [Fig. 3-10(a)] for an *AoA* of 15°. The planes show the main flow features surrounding the 3D models. Note that the three planes are the same as in Fig. 3-5(a). Planes 1 and 3 pass between two fringes. Thus, the black dashed rectangles in the insets of Figs. 3-10(c) and 3-10(g) indicate this gap in the TE plate compared to the CW plate, highlighting the differences in the flow structures because of the shorter chord length.

The upstream flow structures (from the LE to mid-chord) for the CW and TE plates apparently have very similar feature at the three planes, as reported by Jones *et al.* [30] and Rong *et al.* [112], whereas the downstream flows (from mid-chord to the TE) are drastically altered due to the TE fringes. In planes 1 [Figs. 3-10(f) and 3-10(g)] and 3 [Figs.

3-10(b) and 3-10(c)], which pass between two fringes, there is a large flow in this gap [black dashed rectangles in Figs. 3-10(c) and 3-10(g)], which lowers the pressure difference at the TE [Figs. 3-5(b) and 3-5(d)] and hence, the lift coefficients (Table 3-3). In plane 2, which passes through a fringe, there are differences in the flow structures for the CW and TE plates at the TE [Figs. 3-10(d) and 3-10(e)]. The TE fringes alter the separated flows and TE vortices, both spanwise and chordwise, leading to a pressure reduction on the lower surface [Fig. 3-5(c)]. These 3D features of the near-field flow structures distinctly depend on the spanwise location of the cross section.

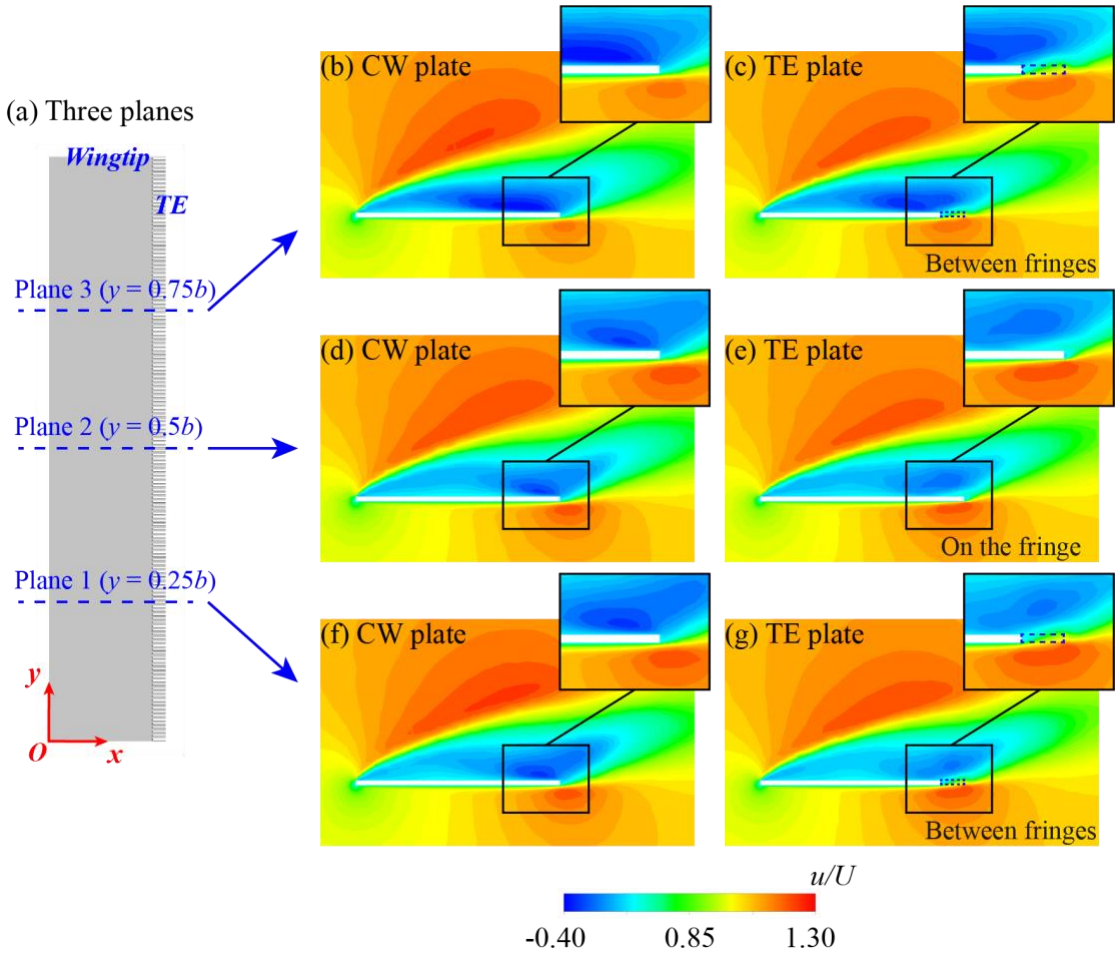

Fig. 3-10. (a) Three planes. (b)–(g) Contours of the time-averaged chordwise velocity normalized by the freestream velocity U_∞ around the CW plate (middle) and the TE plate (right) for plane 3 (top), plane 2 (middle), and plane 1 (bottom) (*AoA* = 15°).

To provide an overall picture of the 3D flows and wake topology around the

owl-inspired models, we visualized the vortical structures around the CW and TE plates for *AoA*s of 5° and 15° (Fig. 3-11). We then investigated the effects of TE fringes on the generation, shedding, and break-up of 3D turbulent vortices, including the LE, TE, and wingtip vortices as well as spanwise flows. The figure shows the instantaneous iso-surfaces of the Q criterion, which is normalized by the chord length (c) and freestream velocity (U_∞). The chordwise vorticity (ω_x) is further employed to characterize the swirling features of the turbulent vortices.

As illustrated in Fig. 3-11, for the low *AoA* of 5° [Figs. 3-11(a), 3-11(b)], owing to the adverse pressure gradient, shear layer separation occurs immediately in the vicinity of the LE. Its features are very similar for the CW and TE plates. The flow separation and vortex dynamics are characterized by multiple slender tube-shaped vortices in the spanwise direction. These develop and are then substantially shed over the upper surface at mid-chord due to the Kelvin–Helmholtz instability, producing the laminar–turbulent transition. The tube-shaped vortices then break up downstream of the mid-chord into horseshoe-shaped vortices and eventually shed into the wake. The close-up bottom view of the CW plate [Fig. 3-11(b)] shows large TE vortices, which merge with the shed vortices over the upper surface, causing highly intensive flow fluctuations near the TE. Comparatively, the fringes on the TE plate break down the TE vortices into many small eddies, which mitigate the energy dissipated by vortex shedding [35] and help suppress the flow instabilities.

For the high *AoA* of 15° [Figs. 3-11(c), 3-11(d)], the shed vortices are more intense due to the larger separated shear layer. They roll up over the mid-chord and generally merge with the TE vortices. Again, the large TE vortices of the TE plate break down due to the TE fringes, leaving the small eddies attached to the fringe tips while the large vortices [i.e., the partial-slip (advance) TE vortices] become distributed at the fringe roots. The breaking of large-scale TE vortices decreases negative pressures on the lower surface near the TE (Fig. 3-5) and hence aerodynamic forces (Table 3-3). Moreover, the close-up bottom view [Fig. 3-11(d)] shows that the TE vortices are more complex than those for the low *AoA*. In addition, the small vortices also have distinct 3D features in the spanwise direction. There is intense vorticity on the fringe edges and alternately positive and negative vortex helicity at adjacent edges, which may further facilitate the dissipation of

energy by the eddy shedding [37].

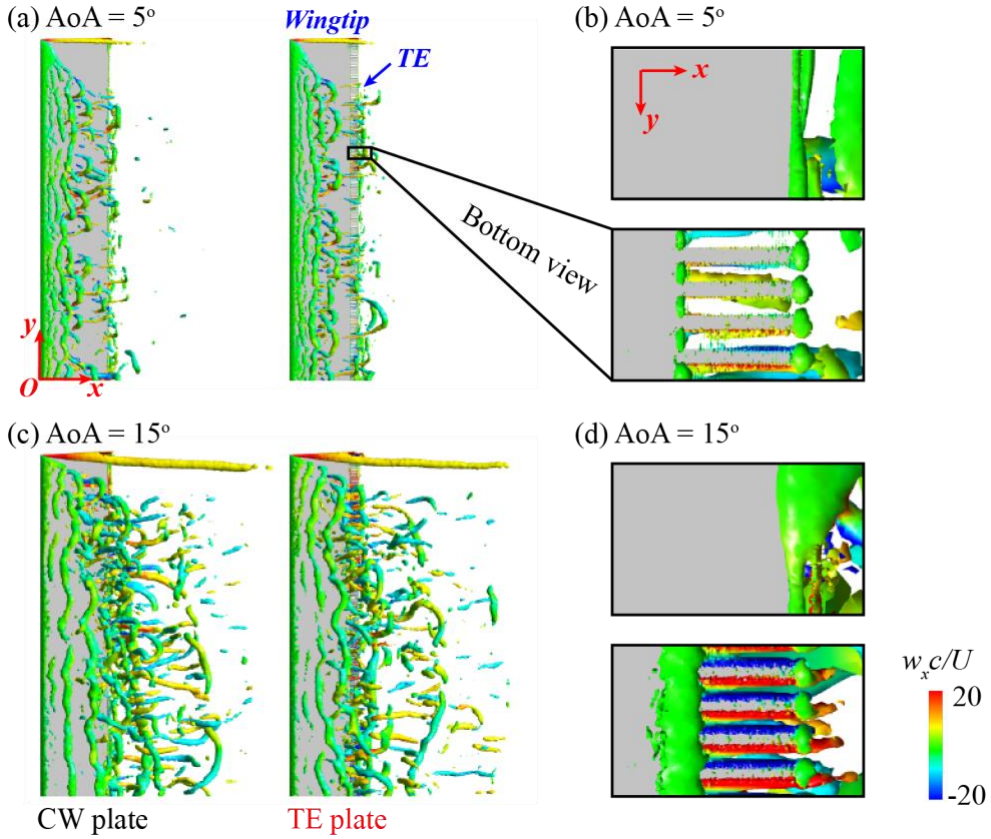

Fig. 3-11. Instantaneous iso-surfaces of the normalized *Q* criterion for the CW plate and TE plate for *AoA*s of 5° (top) and 15° (bottom), characterized by the normalized chordwise vorticity (normalized *Q* = 50): (a) perspective (b) and bottom view at *AoA*=5°, and (c) perspective and (d) bottom view at *AoA*=15°.

Overall, the vortical structures (e.g., wingtip vortices) surrounding the 3D models have obvious 3D features not seen in the 2D results [112]. The large 3D vortices, which significantly affect the aeroacoustic characteristics induced by the TE fringes, can be better recognized with 3D models. Consequently, 3D models provide a more comprehensive perspective for analyzing the 3D mechanisms of TE fringes associated with aerodynamic force production and sound reduction. Note that the broken TE vortices trend to be distributed along the fringe edges and tips, implying that the degree of vortex breaking (and hence, the sound reduction) may strongly depend on the geometrical characteristics of

the fringes [28, 34]. Compared to the large sawtooth fringes usually employed in previous studies [30, 31], the compact and fine fringes in this study can break vortices into extremely small eddies.

As the far-field acoustic fields are closely associated with the near-field flow fluctuations, we further visualized the TKE for the CW plate model and the three TE fringed models for an *AoA* of 15° for the two planes defined in Fig. 3-12(a). The aim was to illustrate the 3D relation between the near-field vortical flows (Fig. 3-11) and the suppression of flow fluctuations by the TE fringes (Fig. 3-12). The TKE is often utilized to characterize the 3D turbulent fluctuations associated with the development and breaking of turbulent eddies. It is defined as

$$\mathrm{TKE} = \frac{(\overline{u'u'} + \overline{v'v'} + \overline{w'w'})}{2}, \qquad (3-1)$$

where, $\overline{u'u'}$, $\overline{v'v'}$, and $\overline{w'w'}$ denote the Reynolds shear stress components in the chordwise, spanwise, and wall-normal directions, respectively. These are calculated using the time-varying velocity fields based on the LES simulations.

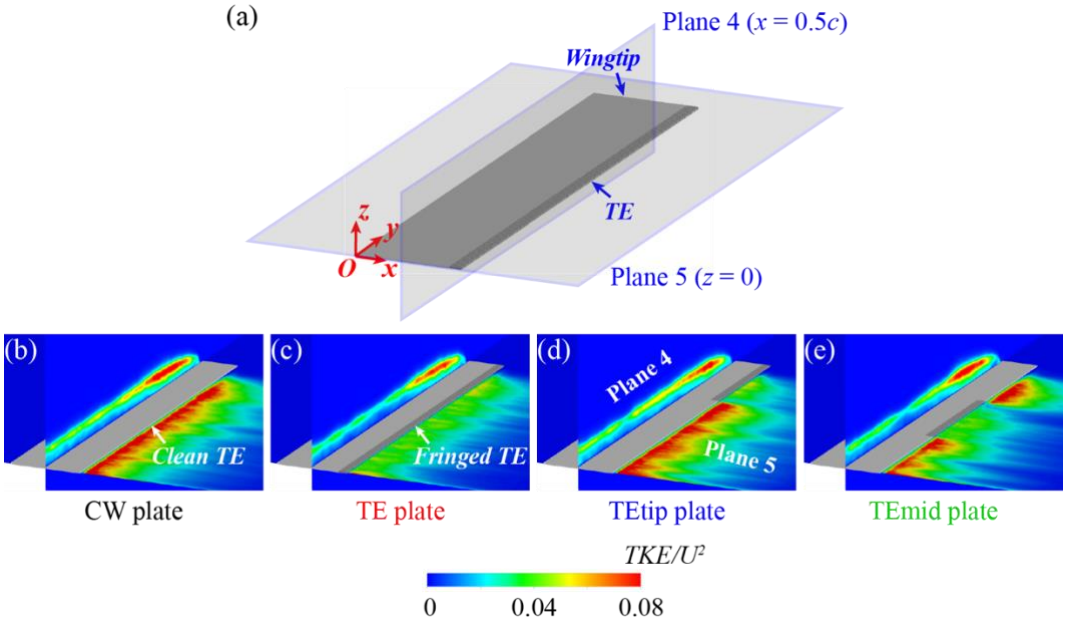

Fig. 3-12. (a) Planes 4 and 5. Contours of normalized TKEs of (b) the CW plate, (c) the TE plate, (d) the TE-tip plate, and (e) the TE-mid plate (*AoA* = 15°).

For the CW plate [Fig. 3-12(b)], the flow fluctuations with high TKE are observed

over the upper surface due to the wingtip vortices [Fig. 3-11(c)]. In the vicinity of the TE, they are attributed to the interaction between shed vortices and TE vortices [Figs. 3-11(c), 3-11(d)]. Comparatively, for the TE plate [Fig. 3-12(c)], the flows induced by the TE fringes are stable. There are much lower TKEs across the wingspan, obviously due to the break-up of the TE vortices [Fig. 3-11(d)]. The much lower level of the TKEs corresponds to a remarkable reduction in the OASPLs (Figs. 3-7, 3-8, and 3-9). On the other hand, the TKEs over the upper surface are apparently less affected by the fringes, indicating that their effects on the wingtip vortices are relatively limited.

Furthermore, the partially fringed TEs of the TE-tip plate and TE-mid plate can also stabilize the local TE flow fluctuations [Figs. 3-12(d) and 3-12(e)]. In the region with the TE fringes, the fringes can directly suppress the flow fluctuations and lower the TKEs but they have less impact in the non-fringed region, demonstrating that the TE fringes, as robust [112] but moderate flow control devices, are useful in altering the local vortical flows in both the chordwise and spanwise directions. These results demonstrate that the owl-inspired TE fringes are effective and versatile. They can be applied specifically to targeted portions of a wing or blade to achieve sound reductions spatially without affecting the aerodynamic performance.

3.4.2 TE fringe-induced aerodynamic characteristics

Based on the preceding discussion about the near-field 3D flow structures associated with TE fringes, here we investigate the aeroacoustic characteristics of the TE fringes to reveal the underlying 3D mechanisms of sound reduction by the fringes.

We first compare for the four wings the spatial distributions of the velocity and the velocity fluctuations in the chordwise and spanwise directions. The contours of the chordwise (i.e., streamwise) velocity components (u) of the CW plate, TE plate, TE-tip plate, and TE-mid plate are plotted for the midplane (z = 0) in Fig. 3-13. The three velocity components (u, v, w) together with their fluctuations are plotted in Fig. 3-14 along a line at the TE (line 1 in Fig. 3-13). It is worth noting that the fluctuations of the three velocity components (T_u, T_v, and T_w) are employed to estimate the features induced by the TE fringes in the 3D flow fluctuations, which are defined by the RMSE of the instantaneous velocity components. For instance, the streamwise (x-axis) velocity fluctuation is

expressed as

$$T_u = \frac{1}{U_\infty}\sqrt{\frac{\sum_{i=1}^{n}(u-\bar{u})^2}{n}}, \qquad (3-2)$$

where $\bar{u}$ denotes the time-averaged chordwise velocity. The spanwise (y-axis) and vertical (z-axis) velocity fluctuations (T_v and T_w) are defined similarly.

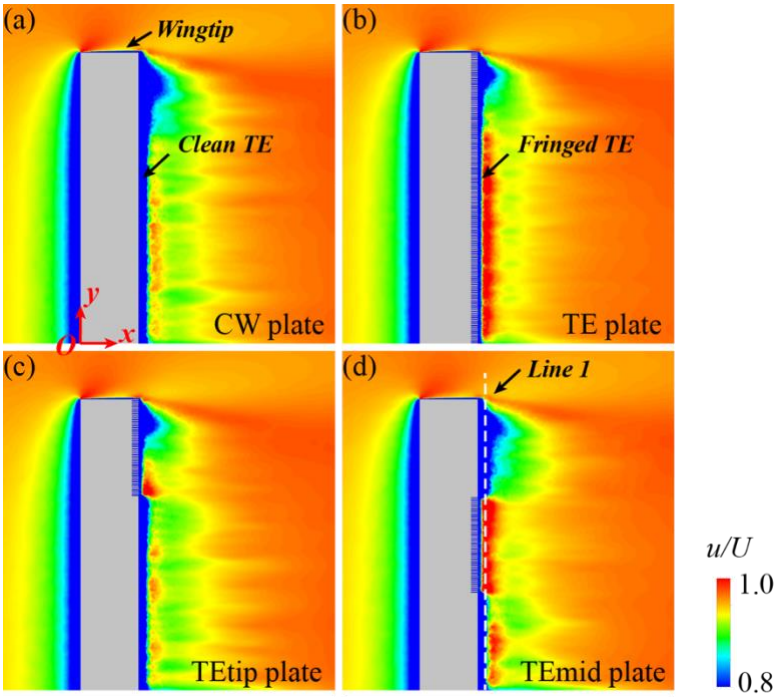

Fig. 3-13. Contours of the time-averaged normalized chordwise (i.e., streamwise) velocities of (a) the CW plate, (b) the TE plate, (c) the TE-tip plate, and (d) the TE-mid plate (*AoA* = 15°).

In Fig. 3-13, for the three TE-fringed models, in the wake immediately downstream of the TE fringes there is a region where the streamwise (chordwise) velocity components are highly enhanced. This is the region where the TKE is remarkably suppressed (Fig. 3-12). This implies that the velocity-enhanced features could indicate where the TE fringes work effectively. This is confirmed in detail in Fig. 3-14. For the CW plate, the streamwise velocity [black line in Fig. 3-14(a)] is less than 0.7 along the wingspan. It gradually decreases, with a steeper drop at 0.7b and then increases at 0.9b until it reaches the freestream velocity. For the fully fringed TE plate, the chordwise velocities [red line in Fig. 3-14(a)], however, remain high and very close to the freestream velocity from the

wing root up to 0.7*b* wingspan. Then, there is a similar drop and rise, as for the CW plate, because of the wingtip vortex, indicating that the effect of the TE fringes disappears in this region. Because of the higher chordwise velocities due to the fringes, the fluctuations are remarkably lower over much of the wingspan [black and red lines in Fig. 3-14(b)], indicating that the TE fringes can enhance the flow stabilization (Fig. 3-12) [112]. Similar results are observed for the vertical direction (along the *z*-axis). That is, the vertical velocities are significantly enhanced by the TE fringes [Fig. 3-14(e)] whereas the fluctuations are largely suppressed [Fig. 3-14(f)]. In proximity to the wingtip, however, the wingtip vortex obviously dominates the local flow structures and hence, negates the effects of the TE fringes [Fig. 3-11(c)].

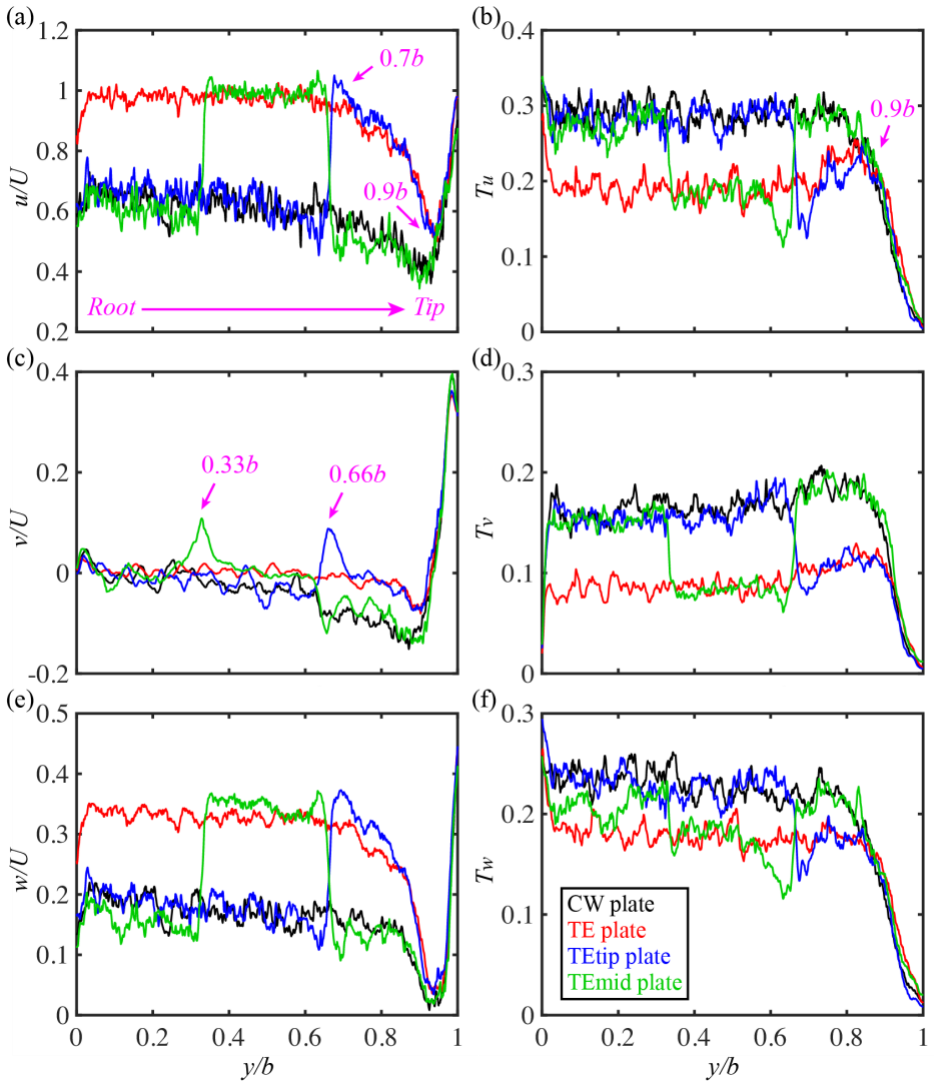

Fig. 3-14. The three velocity components (left) and their fluctuations (right) for the CW plate, TE plate,

TE-tip plate, and TE-mid plate along line 1 in Fig. 3-13 (*AoA* = 15°).

Unlike the streamwise and vertical flows, for both the fringed and non-fringed models, the spanwise velocity components [Fig. 3-14(c)], which are in the *y*-direction, are small, fluctuating around zero from the wing root to the midspan. They have distinctive features near the wingtip. There are peaks in the spanwise velocities at 0.33*b* and 0.66*b* for the TE-mid and TE-tip plates, respectively, [Fig. 3-14(c)], which correspond to the edges of the line of partially distributed fringes. However, the fluctuations are remarkably suppressed [Fig. 3-14(d)]. T_v is suppressed by 0.1 from the wing root to 0.9*b*, as also observed for the chordwise velocity fluctuations [Fig. 3-14(b)]. Our results indicate that the impact of the TE fringes on the near-field flow structures in the vicinity of the TE is highly 3D, indicating the importance of the spanwise flows induced by the fringes, which were not modeled in the 2D study [112]. The control of the spanwise flows is crucial in terms of sound reduction.

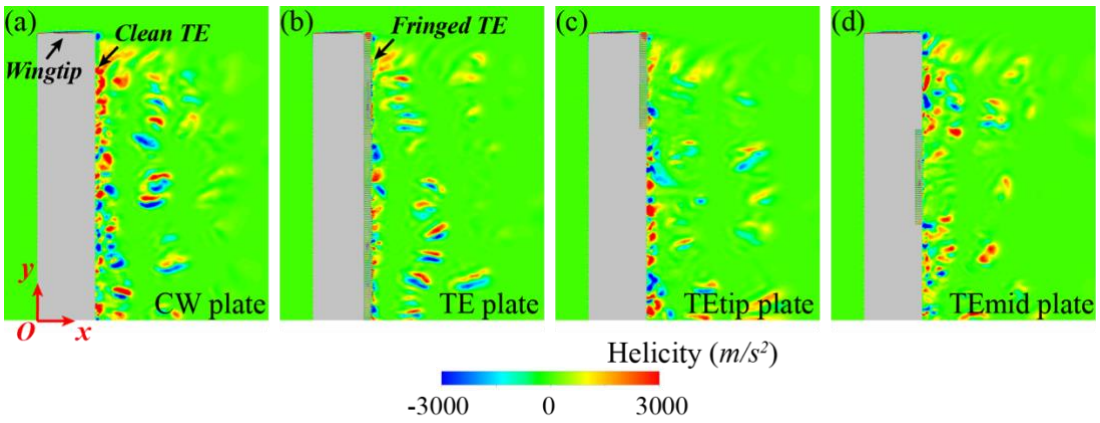

Fig. 3-15. Helicity distributions of (a) the CW plate, (b) the TE plate, (c) the TE-tip plate, and (d) the TE-mid plate (*AoA* = 15°).

Figure 3-15 shows the helical characteristics of the TE-induced flows in the midplane of the CW plate model and TE-fringed models. The helicity is the dot product of the velocity vector ($\vec{U}$) and the vortical vector ($\vec{\omega}$). It is positive if the vectors are in the same direction and negative otherwise. The CW plate has chaotic and intensively helical vortical flows [Fig. 3-15(a)], due to the violent interaction between the shed and TE vortices. For

the TE plate [Fig. 3-15(b)], in contrast, the helical characteristics are remarkably suppressed. The TE vortices have broken into small eddies and the shed vortices are largely reduced [Figs. 3-11(c), 3-11(d)], thus leading to a reduction in sound. In the wake, some shedding of vortex pairs with alternating positive and negative helicity can be observed, corresponding to the small eddies induced by the TE fringes [Fig. 3-11(d)]. The helicity is also suppressed for the TE-tip and TE-mid plates, especially for the fringes at the midspan.

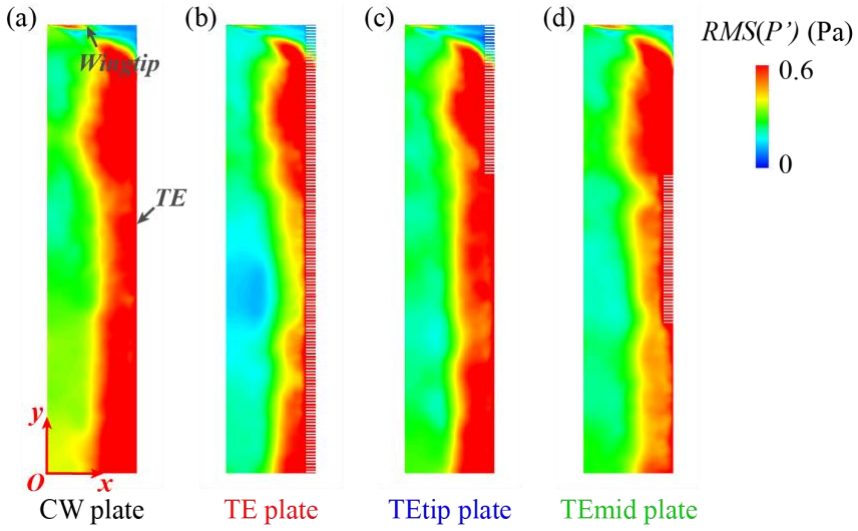

Fig. 3-16. Surface-pressure fluctuations for (a) the CW plate, (b) the TE plate, (c) the TE-tip plate, and (d) the TE-mid plate (*AoA* = 15°).

As the far-field acoustic pressures are highly dependent on the near-field unsteady pressure fluctuations [50, 51], to assess the strength and propagation of sound sources, we further visualized the pressure fluctuations on the upper wing surfaces (Fig. 3-16) and in the wake (Fig. 3-17). The pressure fluctuations usually scatter at a sharp TE and propagate acoustic energy to the far field [114], which are estimated by the RMS of the fluctuating pressures P':

$$P' = P - \bar{P}, \qquad (3-3)$$

where P and $\bar{P}$ are the instantaneous pressure and the average pressure, respectively.

The pressure fluctuations have an intense distribution [Fig. 3-16(a)] near the TE for the CW plate owing to the intense interaction between turbulent vortices and wing surfaces,

and these fluctuations are clearly suppressed by the TE fringes [Figs. 3-16(b), 3-16(c), and 3–16(d)] due to the passive flow control of the TE fringes [Figs. 3-11(c), 3-11(d)] [114]. Again, because the wingtip vortex dominates the flow structures in the vicinity of the wingtip, the fringes in the TE-tip plate cannot reduce the local pressure fluctuations. In contrast, the fringes on the TE-mid plate obviously suppress the pressure fluctuations, not only near the midspan, as they also have a synergetic effect on the non-fringed region toward the wing root.

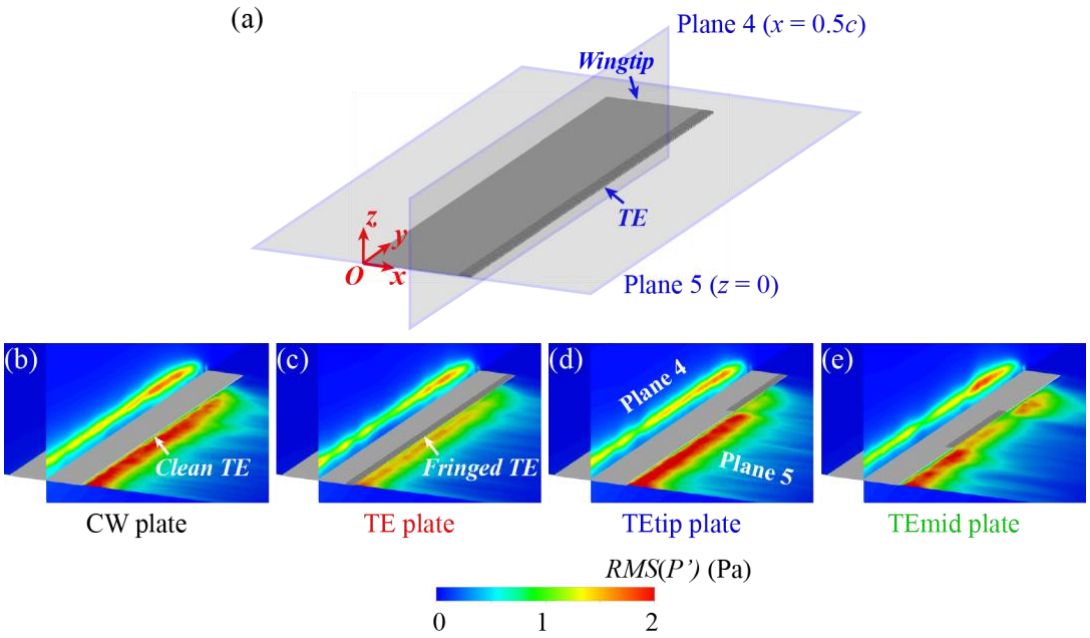

Fig. 3-17. (a) Planes 4 and 5. Pressure fluctuations around (b) the CW plate, (c) the TE plate, (d) the TE-tip plate, and (e) the TE-mid plate (*AoA* = 15°).

The pressure fluctuations in the near wake at the TE (Fig. 3-17) have a trend like that of the TKE distributions (Fig. 3-12), indicating that the flow instability is mainly induced by the shedding vortices and their interaction with the TE vortices. For the CW plate, intense flow instability can be observed near the TE and wingtip [Fig. 3-17(b)]. Whereas for the TE-fringed models, the pressure fluctuations are remarkably suppressed in the wake downstream of the fringes [Figs. 3-17(c), 3-17(d), and 3–17(e)], which is likely the immediate reason for the far-field sound reductions (Figs. 3-7, 3-8).

Note that these results verify that TE fringes are inefficient in suppressing the intense

flow and pressure fluctuations induced by the wingtip vortices in all the 3D wing models. Instead of the rectangular wing configuration utilized here, the 3D geometry of a real feather, which normally has a curved LE, a sharp wingtip, complex thickness and camber variations, and more importantly, high flexibility [36, 45, 90], may significantly alter the characteristics of the wingtip vortex and, thus, in facilitating the passive flow control by the TE fringes, even in the vicinity of the wingtip. In our future studies, we will model the fluid–structure interactions of real owl feathers, taking into consideration the complex 3D geometric features.

3.5 Summary

This section presents a numerical study of the 3D aeroacoustic characteristics induced by TE fringes by integrating LES modeling with FW-H analogy. One CW model and three wing models with realistic fringe-like structures were utilized based on the measured values of a single owl feather. LES simulations were carried out at a low *Re* of 6000, corresponding to the typical flight speed of an owl (3 m/s). Our main findings are summarized as follows:

(1) The owl-inspired TE fringes, which are compact and fine, enable passive control of the near-field 3D flow structures. They achieve remarkable sound reduction, as measured by the OASPLs, throughout the space (e.g., by 5.5 dB in the vertical or *z*-direction for the TE plate model for *AoA* = 15°) while having comparable aerodynamic performance as the non-fringed model. We verified the conclusions of our previous 2D study [112] that 3D TE fringes can be a robust sound-reduction device and solution to the trade-off between the aerodynamic force produced and sound reduction.

(2) The 3D acoustic mechanisms for the reductions in the OASPLs by the TE fringes was clarified. Large spanwise TE vortices are broken up into very small eddies along the fringe edges, which remarkably reduces the 3D flow fluctuations, as observed from the three velocity components and their fluctuations. The impact of the TE fringes on the near-field flow structures in the vicinity of the TE is highly 3D. In particular, the fringe-effects on the spanwise flows, which were not modeled in 2D simulations, are found to passively stabilize the chordwise (streamwise), spanwise and vertical flows.

Consequently, benefiting from the passive control of the 3D vortical flow structures, more sound reductions are achieved for the 3D TE-fringed wing model (5–6 dB) compared to the 2D results (2–3 dB) [112].

(3) The acoustic sources of the 3D wing models are mainly associated with wingtip vortices and the interaction between shed and TE vortices. We proved that the passive flow control by the TE fringes can effectively reduce the sound produced at the TE but not at the wingtip because the large wingtip vortices dominate the local flow fields and negate the effect of the TE fringes. As a result, the TE fringes at the midspan have much better acoustic performance throughout the wingspan than those at the wingtip, indicating that there may be an optimal distribution of fringes that maximizes sound reduction.

Our results demonstrate that the aeroacoustic characteristics of the TE fringes are highly 3D in terms of the near-field flow and vortical structures, far-field acoustic fields, TKE distributions, and flow stabilization. The owl-inspired TE fringes may serve as a robust and versatile device for reducing the sound produced at specific parts of a wing through optimizing their spatial distribution.

4 Effects of owl-inspired leading-edge serrations on feather slots interaction

4.1 Introduction

Leading-edge (LE) serrations observed on the owls' outermost remiges [11, 15, 24] are recognized to play an important role in owl's silent flight [4, 5, 10, 12, 14]. These serrations passively control airflow around the wing feathers in terms of boundary layer separation, laminar-turbulent transition, and flow instability [59-61], hence altering the wing aeroacoustic characteristics. The underlying mechanisms of LE serrations associated with aerodynamic force production and sound reduction can inspire innovative biomimetic designs for low-noise fluid machinery (e.g., airfoils [19, 69], wind turbines [70], and flow fans [9, 75, 76]).

While the aeroacoustic characteristics of LE serrations have been widely studied using single feathers/airfoils, how they affect feather-feather (feather slots) interactions during flight remains unclear. Owl wings are composed of multiple feathers, and during flight there are strong interactions between the feathers, i.e., the feather slots, particularly at wingtips where the feathers do not overlap [Fig. 4-1(a)] [63]. The feather-feather interactions can dramatically alter wing aeroacoustics and become one of the dominant wing acoustic mechanisms during flight [77-79], making them a key issue in revealing the aeroacoustic mechanisms of LE serrations in the silent flight of owls. Given that LE serrations are typically observed on the outermost remiges of the owl wing [24, 80], they assuredly have a significant effect on feather-feather (feather slots) interactions and hence alter the aeroacoustic characteristics of the downstream feathers and the entire wing [63, 64].

Here we conduct a numerical study of the effects of LE serrations on feather-feather (feather slots) interactions in terms of aerodynamic force production and sound reduction by constructing a tandem wing model with LE serrations dsitributed on the LEs of the fore

and hind wings. The aeroacoustic characteristics of the serrated tandem wing model with various gap distances (the distance between the fore and hind wings in the tandem wing model) were resolved in a loosely coupled manner by combining the LES modeling of near-field flow structures and the FW-H analogy for far-field acoustic prediction.

4.2 Tandem wing models with owl-inspired LE serrations

4.2.1 Tandem wing models

Given the observation that LE serrations are typically distributed on the LE of owls' outermost remiges [e.g., the 10th primary feathers (P10), see Figs. 4-1(a), 4-1(b) and 4-1(c)] [15, 24, 64], inspired by the primary feather slots at wingtip of owls in flight [Fig. 4-1(a)], we constructed a serrated tandem wing model in which LE serrations are distributed on the LE of the fore wing [Fig. 4-1(d)] to unravel the effects of LE serrations on feather-feather (feather slots) interactions in terms of aerodynamic force production and sound reduction associated with owl flight. A clean tandem wing model with clean (non-serrated) LEs for both the fore and hind wings was employed as the base/reference model.

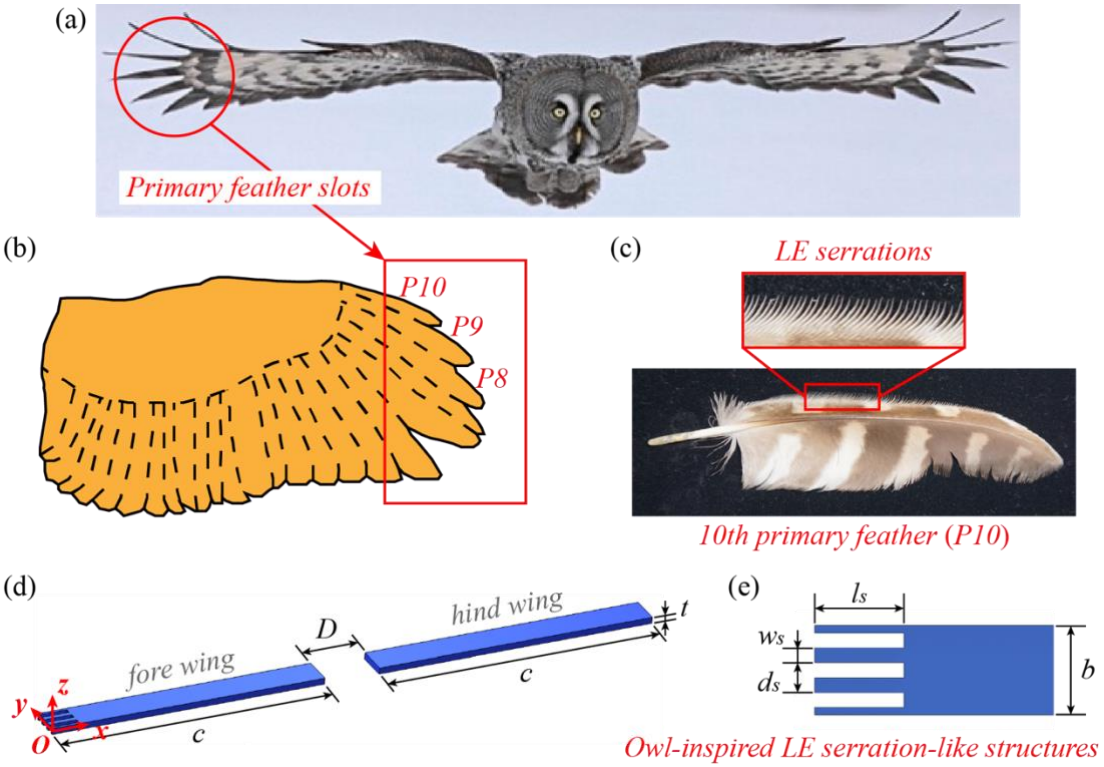

Fig. 4-1. (a) Primary feather slots at wingtip of owl in flight. (b) Illustration of right owl wing. (c) Owl's 10th primary feather showing serrations on LE. (d) Serrated tandem wing model comprising fore and hind wings. (e) Owl-inspired serration-like structures on LE of fore wing.

As illustrated in Fig. 4-1(d), the fore and hind wings in the tandem wing model were flat plate models of single owl feathers. They had the same geometric dimensions comprising chord length (c), thickness (t), and span length (b). The distance between the two wings (i.e., gap distance D) varied from 0.06c to 2c. With a focus on the underlying mechanisms of LE serrations, the camber and thickness variations of the feathers were neglected, and the owl-inspired serrations on the LE of the fore wing were distributed uniformly aligning with the incoming airflow [Fig. 4-1(e)]. The hind wing had a clean LE in both the serrated and clean tandem wing models. The basic geometric parameters of the wings and serrations (Table 4-1) were identical to those employed in our previous studies [59-61, 112], which has been confirmed to capable of revealing the essential physical mechanisms associated with LE serrations. In addition, as defined in Fig. 4-1(d), the origin of the coordinate system of the computational models is located at the LE of the fore wing, with the x- and y-axes pointing in the chordwise and spanwise directions of the wings, respectively. Then, the z-axis was determined by the right-hand rule, pointing in the vertical (wall-normal) direction.

Table 4-1. Geometric parameters of tandem wings and LE serrations.

Parameter	Symbol	Size (mm)
Chord	c	30.0
Span	b	3.0
Thickness	t	0.67
Length of serrations	ls	3.0
Width of serrations	ws	0.5
Interval between serrations	ds	1.0
Gap distance between wings	D	0.06c~2c

To resolve the large-scale turbulent flows surrounding the tandem wing models with LE serrations, an H-type structured grid system was employed, as shown in Fig. 4-2. The grid elements were refined in adjacent areas of the wing surfaces [Figs. 4-2(b) and 4-2(c)]

to ensure that the transient flow information in the boundary layer could be well captured, which is in close association with the accuracy of far-field sound prediction [25, 106, 107]. For the first layer grids adjacent to the wing surfaces, the height was defined by a formula $\delta = 0.1c/\sqrt{Re}$ [59, 111], to satisfy the requirement that the dimensionless wall-normal distance is less than 1 (y plus < 1). For the low speed of owl forward flight (2.5–7.5 m/s [64]), the freestream velocity was taken to be 3 m/s, resulting in a *Re* of 6000 for a single fore or hind wing.

In addition, as illustrated in Fig. 4-2(a), the computational domain was extended 10c upstream (velocity inlet) and 20c downstream (pressure outlet) from the LE of the fore wing to ensure the full development of turbulent flows. In the spanwise directions, translational periodic boundary conditions were imposed to save computational costs. Follow our previous studies [59, 112], the *AoA*s of the tandem wings were set to 5° and 15°, as observed in owl flight, which can exhibit the low- and high-*AoA* aeroacoustic characteristics induced by LE serrations, respectively.

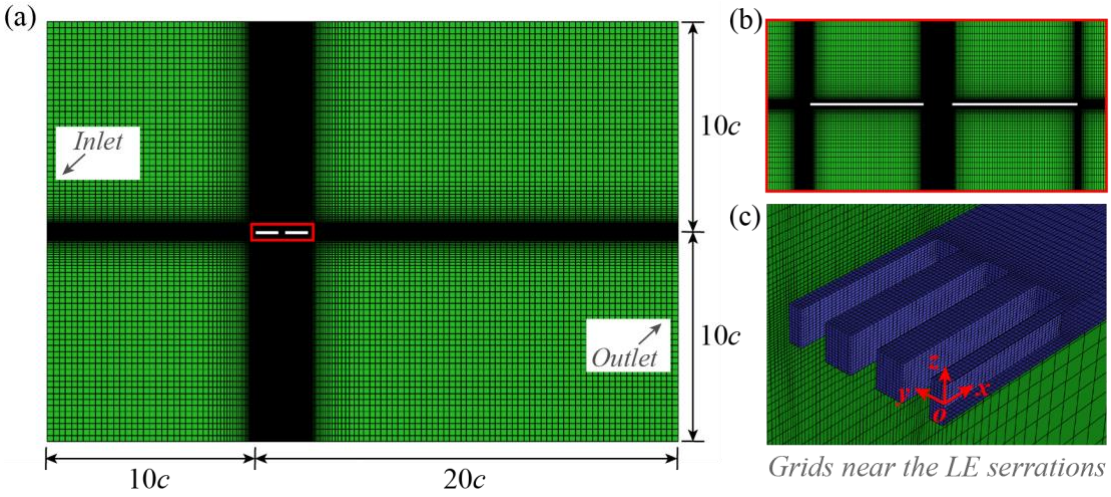

Fig. 4-2. (a) Computational domain and H-type grid system. (b) Near-field grid distributions for tandem wings. (c) Grid elements near serrated LE of fore wing.

4.2.2 Numerical settings

To resolve the transient flow and acoustic fields around the tandem wing models with and without LE serrations, following our previous study [112], we employed a loose-coupling method by combining the LES and FW-H analogy. Specifically, the LES-based simulations were performed to resolve the transient turbulent flows surrounding

the tandem wings. Then, the resolved instantaneous flow variables (e.g., surface pressure fluctuations) were utilized as inputs for the far-field acoustic prediction based on the FW-H analogy.

The LESs were implemented with the commercial CFD software ANSYS Fluent 16.0 (ANSYS, Inc.). The incompressible N–S equations were solved by the pressure-velocity coupling (SIMPLE) algorithm. The value of the subgrid-scale model constant was taken to be 0.325. The time step of the simulations was set to $\Delta t = 5 \times 10^{-5}$ s to satisfy the convergence condition by Courant–Friedrichs–Lewy (CFL) [115] required for the numerical computation (i.e., CFL number < 1). The simulations were performed for a total of 12,000 steps to ensure that the flow fields were statistically stable, and then the final 3000 steps were employed for postprocessing the flow fields and as inputs for far-field acoustic prediction.

With the instantaneous flow variables (e.g., surface pressure fluctuations) from the LESs, the transient acoustic fields of the tandem wing models with LE serrations were predicted with the FW-H equation. According to the FW-H equation [50, 51], the aerodynamic sound can be induced by quadrupole, dipole, and monopole acoustic sources. The quadrupole acoustic sources (volume integrals) are essentially turbulent noise, which is negligible at a low freestream velocity. The dipole and monopole sources (surface integrals) are formed by instantaneous pressure fluctuations and mass movements, respectively. The monopole sources were also ignored in this study because of the low velocity, so the dipole sources were the dominant acoustic sources. Then, all solid walls of the tandem wings were regarded as acoustic surfaces that emit sound.

4.2.3 Verification and validation

Verification and validation of the aeroacoustic simulations of owl-inspired wings were systematically addressed in Sec. 2.2.3. Here a grid independence analysis was conducted to further verify the reliability of the current aeroacoustic simulations of tandem wing models.

Four grid systems with different grid densities were generated for the serrated tandem wing model at a gap distance (D) of 0.2c. The CFD simulations were then performed using the four grid systems at AoA = 5° and Re = 6000. Table 4-2 compares the computed

aerodynamic coefficients among the four grid systems, including time-averaged C_l, C_d, and L/D, which have been defined in Eqs. 2-15 and 2-16.

Note that when calculating the aerodynamic coefficients for a single fore or hind wing, the reference area S is identical to the area of the upper surface of the single wing, which is model-dependent because of the serrations. In contrast, for a tandem wing model, S is the sum of the areas of the upper surfaces of the two wings.

Table 4-2. Comparison of time-averaged aerodynamic force coefficients of a serrated tandem wing model among four grid systems (*D* = 0.2c, *AoA* = 5°, *Re* = 6000).

Parameter	Coarser	Coarse	Medium (adopted)	Dense
Element number	1.71×10^6	2.16×10^6	2.47×10^6	3.95×10^6
Time-averaged C_l	0.4411	0.4599	0.4523	0.4476
Time-averaged C_d	0.0824	0.0842	0.0826	0.0812
Time-averaged L/D	5.3532	5.4630	5.4758	5.5123
$\lvert Error_{L/D} \rvert$	2.89%	0.89%	0.66%	—

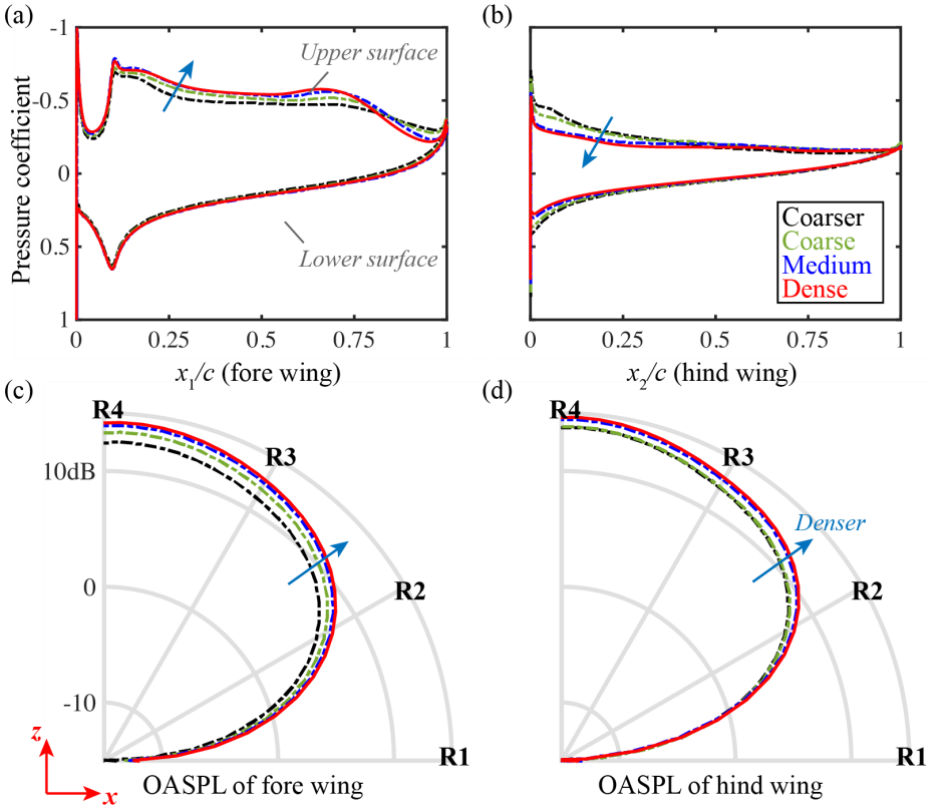

Fig. 4-3. Comparison of time-averaged pressure coefficients on (a) fore and (b) hind wing surfaces and far-field OASPLs of (c) fore and (d) hind wings among four grid systems (D = 0.2c, AoA = 5°, Re = 6000). Blue arrows show the direction with increasing grid density. Local coordinates x_1 and x_2 are measured from the LEs of fore and hind wings, respectively.

From Table 4-2, a mere marginal difference is seen of 0.66% in the L/D between the medium and dense grids. In addition, the surface-pressure coefficients of the fore [Fig. 4-3(a)] and hind [Fig. 4-3(b)] wings and the far-field OASPL distributions of the fore [Fig. 4-3(c)] and hind [Fig. 4-3(d)] wings were also compared among the four grid systems. Note that the definition of the OASPL at an acoustic receiver and the arrangement of the receivers (e.g., R1-R4) are described later in Sec. 4.3.2. As illustrated in Fig. 4-3, the aeroacoustic results calculated by the medium and dense grids are well matched. Therefore, the medium grid was adopted for all the aeroacoustic simulations in this study as a compromise between numerical accuracy and computational consumption.

4.3 Effects of LE serrations on tandem wing aeroacoustics

4.3.1 Aerodynamic performance

We first examine the LE serration effects on the aerodynamic performance of the tandem wings. As shown in Fig. 4-4, the time-averaged lift-to-drag ratios of the fore, hind, and tandem wings are compared between the clean and serrated tandem wing models at *AoA*s of 5° and 15°, respectively. At the low *AoA* of 5° [Figs. 4-4(a), 4-4(b), and 4-4(c)], with increasing *D*, the lift-to-drag ratios decrease in the fore wings but increase in the hind wings, consequently leading to a trend associated with the tandem wings that shows a decline at the smaller *D* of 0.06–0.22*c* but turns out to level off after *D* exceeds 0.22*c* [Fig. 4-4(c)]. In addition, there are noticeable discrepancies in the aerodynamic forces for the clean and serrated tandem wing models. The LE serrations of the fore wing, apparently lead to a pronounced reduction for all gap distances in the lift-to-drag ratios of the fore wing [Fig. 4-4(a)] whereas enhancing the hind wing aerodynamic performance [Fig. 4-4(b)]. As a result, the harmful effect of LE serrations on aerodynamic performance is

noticeably diminished for the tandem wings [Fig. 4-4(c)] compared to that observed in an isolated serrated wing [112]. It is worth noting that the mere twin feather-based tandem models are used here. As shown in Fig 4-1(a), owls' wings are normally composed of more feathers, thus may benefit more from the feather-feather aerodynamic interactions in producing aerodynamic forces.

For the high *AoA* of 15° [Figs. 4-4(d), 4-4(e), and 4-4(f)], as *D* increases, a similar trend is observed in the tandem wings that the lift-to-drag ratio shows a slight-down when *D* is less than 0.4*c* but then levels off after that [Fig. 4-4(f)]. Moreover, obviously the lift-to-drag ratios of the tandem wings with the fore wing LE serrations show marginal differences compared to those of the tandem wings with the clean fore wing [Figs. 4-4(d), 4-4(e), and 4-4(f)]. This is consistent with our previous findings using isolated serrated wings, where the LE serrations were reported to lower aerodynamic performance at low *AoA*s but enable achieving comparable aerodynamic performance at high *AoA*s [59, 112].

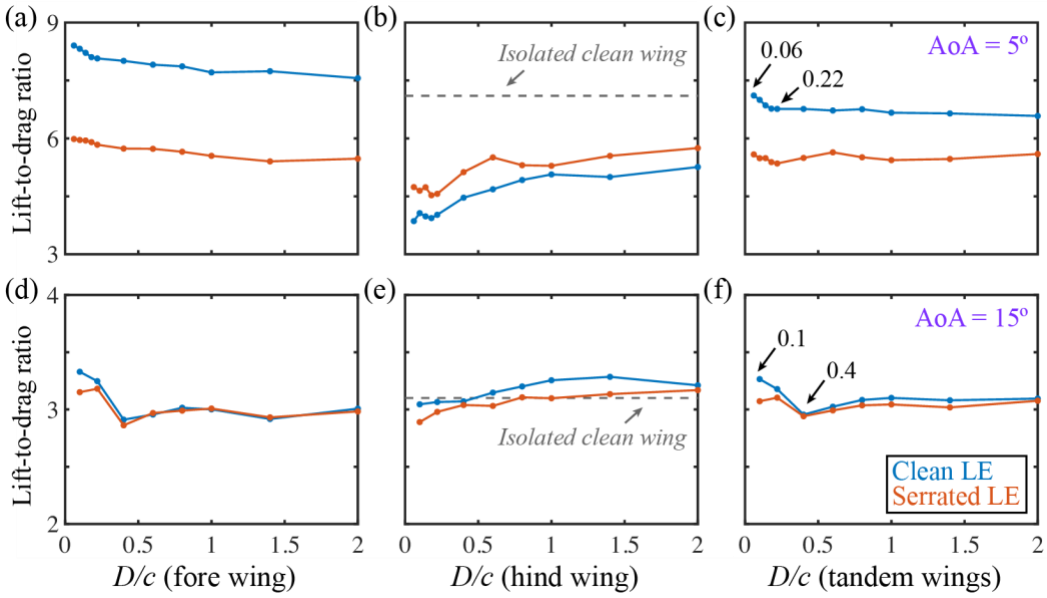

Fig. 4-4. Comparison of lift-to-drag ratios versus gap distance (*D*) between clean and serrated tandem wing models at *AoA*s of 5° (top: (a), (b), (c)) and 15° (bottom: (d), (e), (f)): fore (left: (a), (d)), hind (middle: (b), (e)), and tandem (right: (c), (f)) wings. Black dashed lines represent experimental data by Ikeda *et al*. [71] of an isolated clean wing.

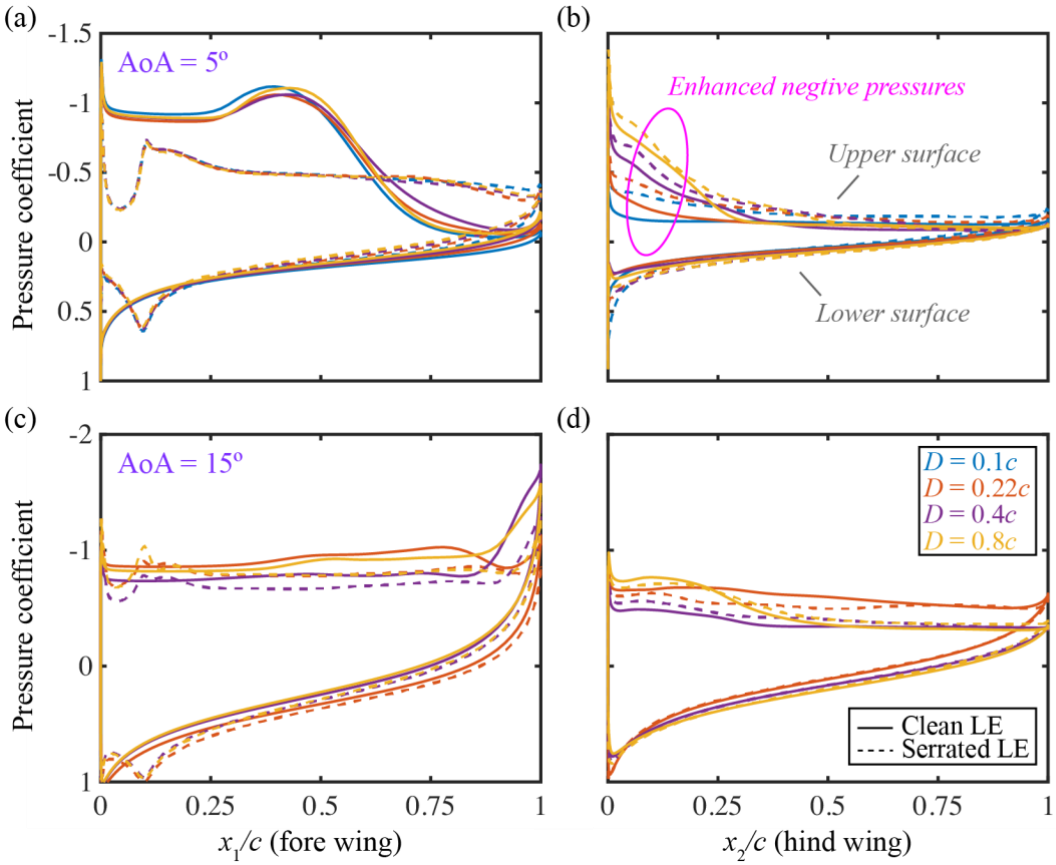

Fig. 4-5. Comparison of time-averaged pressure coefficients on fore (left: (a), (c)) and hind (right: (b), (d)) wing surfaces for clean and serrated tandem wing models at *AoA*s of 5° (top: (a), (b)) and 15° (bottom: (c), (d)).

To explore the aerodynamic mechanisms associated with the LE serration effects, the time-averaged pressure coefficients on the fore and hind wing surfaces are further compared at the low *AoA*s of 5° [Figs. 4-5(a) and 4-5(b)] and 15° [Figs. 4-5(c) and 4-5(d)], respectively. Here, the results of the clean and serrated tandem wing models at four different gap distances (i.e., D = 0.1c, 0.22c, 0.4c, and 0.8c) are chosen for comparison. The pressure difference at the fore wing LE is remarkably reduced in the serrated tandem wing model for all gap distances [Fig. 4-5(a)] owing to the presence of serrations, resulting in a pronounced decrease in the lift-to-drag ratios [Fig. 4-4(a)]. In contrast, the negative pressures at the hind wing LE are enhanced by the serrated fore wing [Fig. 4-5(b)], thus increasing the lift-to-drag ratios of the hind wing [Fig. 4-4(b)] while mitigating the

aerodynamic losses for the tandem wings [Fig. 4-4(c)]. The enhancement effect is robust as *D* increases [pink circle in Fig. 4-5(b)]. However, at the high *AoA* of 15°, the mere marginal differences in pressure coefficients between the clean and serrated tandem wings occur in the vicinity of the TE of the fore wings [Figs. 4-5(c) and 4-5(d)], supporting the results in Figs. 4-4(d), 4-4(e), and 4-4(f).

4.3.2 Acoustic characteristics

We then investigate the LE serration effect on the acoustic performance of the tandem wings by comparing the acoustic results comprising far-field OASPLs and sound pressure spectra between the clean and serrated tandem wing models. Based on the transient sound pressure fields of the tandem wings predicted by the FW-H analogy, the sound pressure spectrum at an acoustic receiver can be calculated by performing an FFT on the sound pressure time series of the receiver with a reference sound pressure of 2×10^{-5} Pa. The upper frequency of the sound spectrum, determined by the data sampling interval, is 10 kHz. Substantially, the OASPL at the receiver can be calculated through integrating over the entire frequency range of the sound spectrum (i.e., 0~10 kHz).

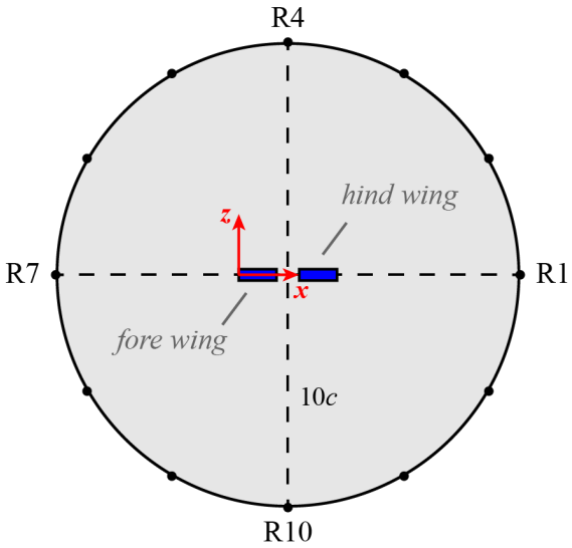

Fig. 4-6. Positions of 12 acoustic receivers (R1–R12) in *xz*-plane for tandem wing model.

Figure 4-6 illustrates the arrangement of the acoustic receivers used for the OASPL calculations. 12 uniformly distributed receivers (i.e., R1–R12) were defined in the *xz*-plane

at a distance of 10c from the center of the tandem wings (i.e., $x = c + D/2$) to capture the spatial acoustic characteristics of the tandem wings. Note that Fig. 4-6 shows an example of how to calculate the OASPL distribution for a tandem wing model. For a single fore or hind wing, the origin of the circle formed by the receivers was located at the center of the single wing.

To provide an overview of the LE serration effects on tandem wing acoustics versus the gap distance D, in Fig. 4-7 we compare the OASPLs (calculated at R4) for the fore, hind, and tandem wings between the clean and serrated tandem wing models at *AoA*s of 5° and 15°. First, at the low *AoA* of 5°, the OASPLs of the fore wing are reduced by the serrations for most gap distances [Fig. 4-7(a)]. For the hind wing, the serrated fore wing causes a slight decrease in the OASPLs at D < 0.22c whereas, with increasing D, the OASPLs of the hind wing are increased significantly [Fig. 4-7(b)]. Consequently, for the tandem wings, the OASPLs show a remarkable increase due to the serrations of the fore wing when D exceeds 0.22c [Fig. 4-7(c)]. This is supported by Bachmann *et al.* [116] that the LE serrations of owls' wing may not work properly at low *AoA*s. However, as depicted in Fig. 4-7(c), when the gap distance D is taken small, less than 0.22c, the serrations seem to facilitate the acoustic performance of the tandem wings. Given the small gap distance between owl wing feathers, owls may benefit from this mechanism when flying at low *AoA*s. Next, at the high *AoA* of 15°, it is found that the LE serrations on the fore wing can consistently reduce the OASPLs of the fore [Fig. 4-7(d)], hind [Fig. 4-7(e)], and tandem [Fig. 4-7(f)] wings in all cases compared to the clean tandem wing model, demonstrating the superior acoustic performance owing to the LE serrations. Thus, we infer that with such feather slots-based noise reduction mechanism at high *AoA*s, the LE serrations on the outermost remiges may powerfully suppress the wing-induced noise during flight. This is supported by the observations that owls normally make a hunting approach at high *AoA*s [Fig. 4-1(a)] [117].

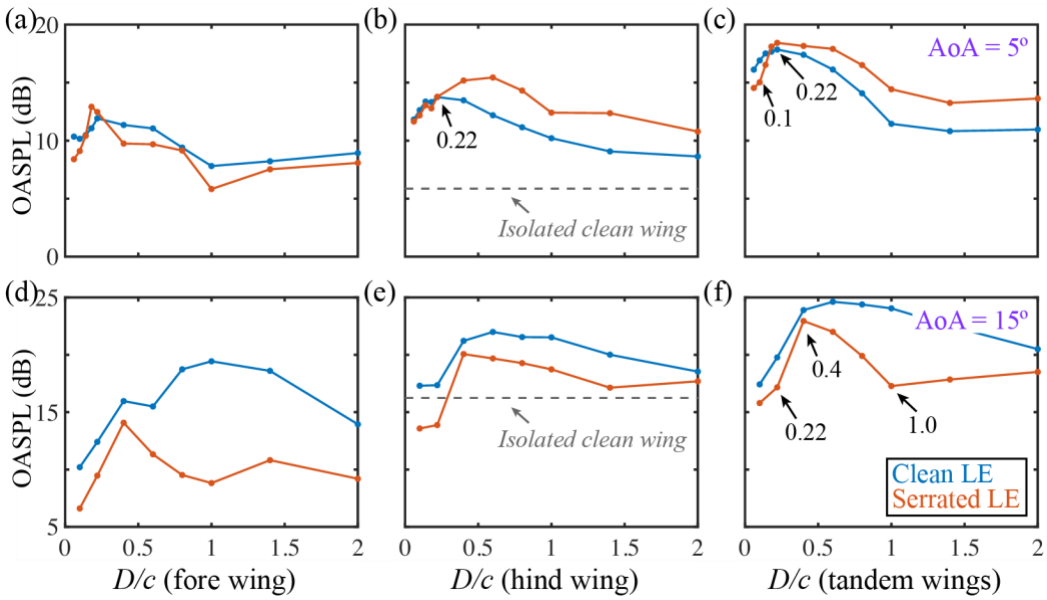

Fig. 4-7. Comparison of OASPLs at R4 between clean and serrated tandem wing models at *AoA*s of 5° (top: (a), (b), (c)) and 15° (bottom: (d), (e), (f)): fore (left: (a), (d)), hind (middle: (b), (e)), and tandem (right: (c), (f)) wings. Black dashed lines represent numerical results by Rong *et al.* [112] of an isolated clean wing.

In addition, the OASPLs of the hind wings [Figs. 4-7(b) and 4-7(e)] gradually approach the results of an isolated clean wing [112] as D increases, implying that the feather-feather (feather slots) interactions eventually disappear. Meanwhile, the aerodynamic results for the hind wings [Figs. 4-4(b) and 4-4(e)] also converge to the experimental data of an isolated clean wing [71] with increasing D, which may further validate the current aeroacoustic simulations.

Furthermore, we examine the spatial characteristics of tandem wing sound propagation by plotting the OASPL distributions in the far field for the clean and serrated tandem wing models at *AoA*s of 5° [Fig. 4-8(a)] and 15° [Fig. 4-8(b)]. Three different gap distances of $D = 0.1c$, $0.4c$, and $0.8c$ are taken into consideration here. As depicted in Fig. 4-8, the distributions of far-field OASPLs of tandem wings exhibit obvious dipole features in all cases, confirming that the near-field pressure fluctuations are the dominant sources of sound radiation. Meanwhile, the sounds induced by the tandem wings tend to propagate upward and downward, reaching maxima at R4 (in the vertical direction of wings). For the

low *AoA* of 5° [Fig. 4-8(a)], the serrated tandem wing model presents noticeably increased OASPLs compared to the clean tandem wing model, except for the model with a small *D* of 0.1*c* [blue lines in Fig. 4-8(a)]. However, for the high *AoA* of 15° [Fig. 4-8(b)], the serrated tandem wing model shows an obvious reduction of OASPLs constantly, which increases with increasing *D* from 0.1*c* to 0.8*c*, having better acoustic performance rather than low *AoA*s.

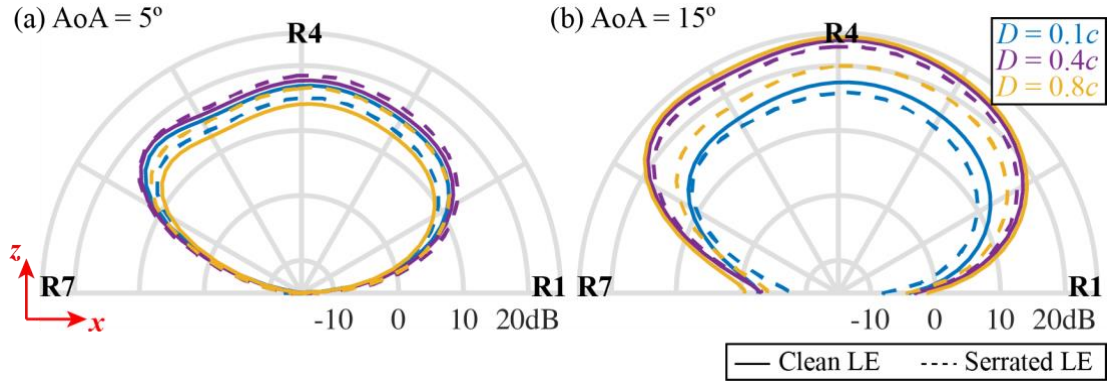

Fig. 4-8. Comparison of far-field OASPL distributions between clean and serrated tandem wing models in *xz*-plane at *AoA*s of (a) 5° and (b) 15°.

The sound pressure spectra at R4 between the clean and serrated tandem wing models is further compared in Fig. 4-9 to elucidate the LE serration effects on the spectral characteristics. At the low *AoA* of 5°, it is found that the sound pressure levels (SPL) are suppressed at mid and high frequencies (especially from 200 to 2000 Hz) for the serrated tandem wing model with a small *D* of 0.1*c* [Fig. 4-9(a)], whereas for the tandem wing model with a larger *D* of 0.4*c* or 0.8*c*, the SPLs are instead enhanced at high frequencies ($f >$ 1000 Hz) [Figs. 4-9(b) and 4-9(c)], resulting in an increase in the far-field OASPLs [Fig. 4-7(c)]. On the other hand, at the high *AoA* of 15°, the SPLs are remarkably suppressed at mid and high frequencies ($f >$ 200 Hz) by LE serrations in all cases [Figs. 4-9(d), 4-9(e), and 4-9(f)]. Thus, the far-field OASPLs are remarkedly and robustly suppressed at this *AoA* [Fig. 4-7(f)]. It seems that the LE serrations in tandem wing models benefit from different aeroacoustic mechanisms at low and high *AoA*s (which will be extensively discussed in Sec. 4.4.1 and Sec. 4.4.2, respectively, by combining the low and high *AoA* flow characteristics around the tandem wings). In addition, there are noticeable

tonal peaks in the sound spectra of the clean and serrated tandem wings at *AoA* = 15° [Figs. 4-9(d), 4-9(e), and 4-9(f)], as also observed in our previous study of an owl-inspired single wings [112]. This may be induced by the large-scale boundary layer at the blunt TE [25] and the well-known acoustic feedback loop [46].

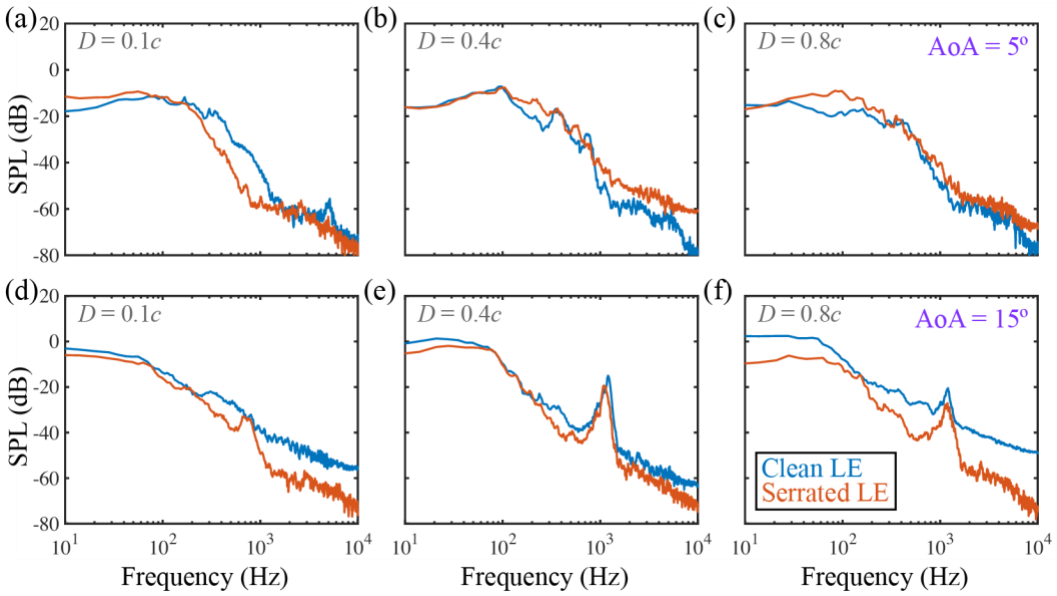

Fig. 4-9. Comparison of sound pressure spectra at R4 for clean and serrated tandem wing models with gap distances (*D*) of 0.1*c* (left), 0.4*c* (middle), and 0.8*c* (right) at *AoA*s of 5° (top) and 15° (bottom).

4.4 Aerodynamic characteristics induced by LE serrations

4.4.1 Low-AoA aerodynamic characteristics

As described above, the serration-induced acoustic performance is sensitive to the gap distance *D* between the fore and hind wings at a low *AoA* of 5° [Figs. 4-7(a), 4-7(b), and 4–7(c)]. Specifically, the LE serrations on the fore wing can reduce far-field OASPLs for tandem wings with small gap distances (e.g., 0.06–0.18*c*) but increase OASPLs for those with large gap distances (e.g., 0.4–2.0*c*). The aeroacoustic mechanisms of the fore wing LE serrations are here elucidated by visualizing the near-field flow structures, vortex dynamics, and flow fluctuations around the clean and serrated tandem wing models at a low *AoA* of 5°. The results at various gap distances of 0.1*c*, 0.14*c*, 0.22*c*, 0.4*c*, and 0.8*c* are analyzed.

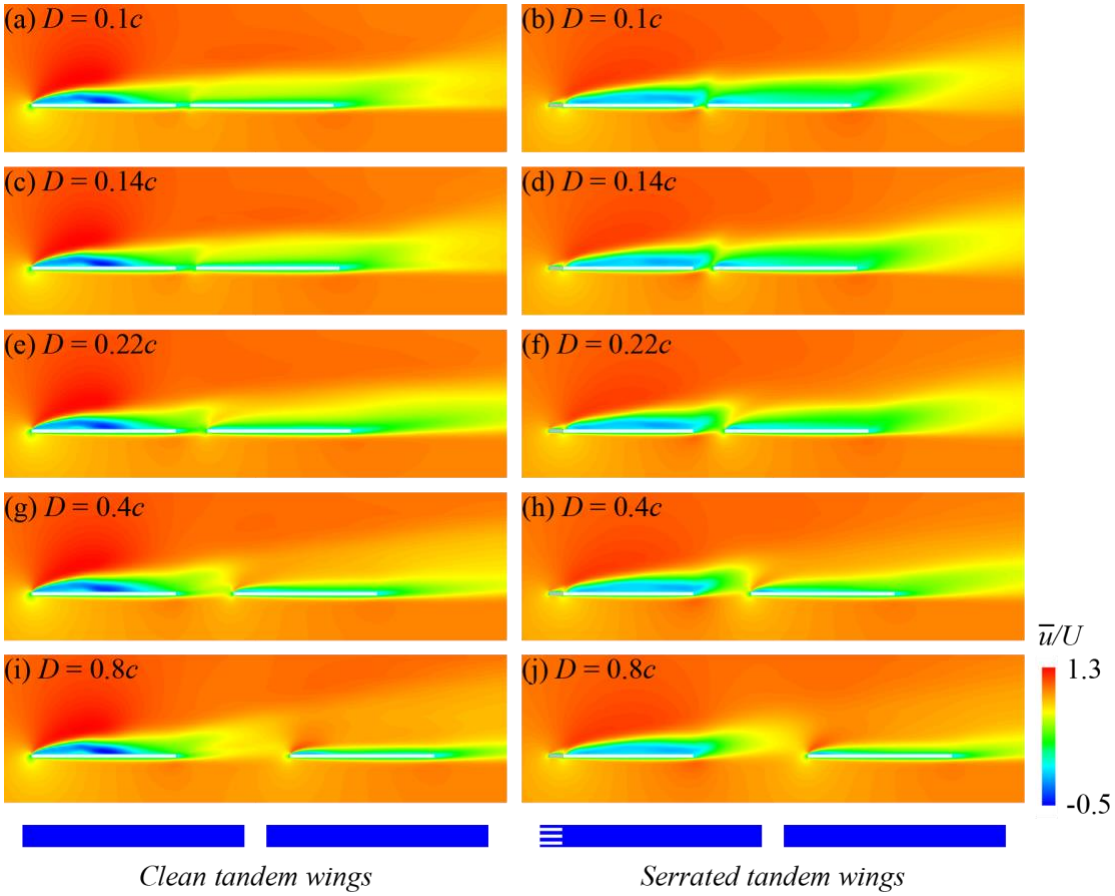

Fig. 4-10. Contours of time-averaged chordwise velocities normalized by freestream velocity U_∞ around clean (left) and serrated (right) tandem wing models at various gap distances (D) for AoA = 5°.

Figure 4-10 shows the contours of the time-averaged chordwise velocities around the clean and serrated tandem wings, which describe the main flow features surrounding the wings. In the clean tandem wing model, an obvious separation bubble can be observed at the LE of the fore wing due to the sharp LE and adverse pressure gradient [Figs. 4-10(a), 4-10(c), 4-10(e), 4-10(g), and 4-10(i)]. The phenomenon was also observed experimentally by Winzen *et al.* [64, 91, 92] and Klän *et al.* [81] using owl-inspired wing models. The separated flow subsequently reattaches to the suction surface at approximately the mid-chord and transitions to turbulence due to the KH instability [110]. When the distance D between the fore and hind wings is small (e.g., 0.1c, 0.14c), the boundary layers of the fore and hind wings congregate, merging together while the boundary layer of the hind wing seems to inherit the downstream/wake flow characteristics of the fore wing [Figs.

4-10(a) and 4-10(c)]. As *D* increases (e.g., 0.4*c*, 0.8*c*), the boundary layer of the hind wing starts to separate, forming a layer of its own, which is however remarkably influenced by the wake of the fore wing [Figs. 4-10(g) and 4-10(i)].

In contrast, the flow characteristics of the serrated tandem wings display pronounced discrepancy. The occurrence of boundary layer separation at the fore wing LE is delayed, and there is no clear reattachment point [Figs. 4-10(b), 4-10(d), 4-10(f), 4-10(h), and 4-10(j)], which is likely attributed to the vortex-broken effect by the LE serrations [59, 112]. Therefore, the suction flow characteristics of the tandem wings are significantly altered, and the aerodynamic performance is diminished due to the absence of the separation bubble [Fig. 4-5(a)]. In addition, with increasing *D*, the hind wing boundary layer likewise changes from congregate [Figs. 4-10(b) and 4-10(d)] to separate [Figs. 4-10(h) and 4-10(j)], resulting in completely different flow characteristics for the cases of small and large gap distances.

We then examine the serration effects on flow instability through investigating the velocity fluctuations (T_u) around the clean and serrated tandem wing models. Here, T_u is defined by the RMS of the fluctuating velocities ($u' = u - \bar{u}$). The RMS of u' can be obtained by processing the time series of the instantaneous velocities generated during the LESs.

As illustrated in Fig. 4-11, for the clean tandem wing model, intense velocity fluctuations are observed from the mid-chord to the wake on the suction side of the fore wing [Figs. 4-11(a), 4-11(c), 4-11(e), 4-11(g), and 4-11(i)], corresponding to the region of laminar-turbulent transition. When the gap distance *D* is small (e.g., 0.1*c*, 0.14*c*), influenced by the fore wing wake, the suction flow of the hind wing is also highly fluctuated and seems to be an extension of the fore wing wake [Figs. 4-11(a) and 4-11(c)]. As *D* increases (e.g., 0.4*c*, 0.8*c*), the fluctuations in the hind wing suction flow are reduced, and a new separated shear layer forms near the hind wing LE, which induces noticeable flow instability there [Figs. 4-11(g) and 4-11(i)]. However, in the serrated tandem wing model, benefiting from the LE serration-based passive flow control [59] (Fig. 4-10), the fore wing suction flow fluctuations are apparently suppressed [Figs. 4-11(b), 4-11(d),

4-11(f), 4-11(h), and 4-11(j)]. As a result, the fluctuations in the hind wing suction flow, which are dominated by the fore wing wake, are also reduced at small gap distances [Figs. 4-11(b) and 4-11(d)]. However, when the gap distance is large (e.g., 0.4*c*, 0.8*c*), the flow fluctuations around the hind wing are enhanced compared to the clean tandem wings, particularly in the vicinity of hind wing LE [black dashed circles in Figs. 4-11(h) and 4-11(j)]. This may be caused by the synergistic/interactive effect of the fore wing wake and the hind wing shear layer. At such a low *AoA* of 5°, the serration-induced partially slipped boundary layer [59] (Fig. 4-10) of the fore wing seems to enhance the flow instability near the LE of the hind wing.

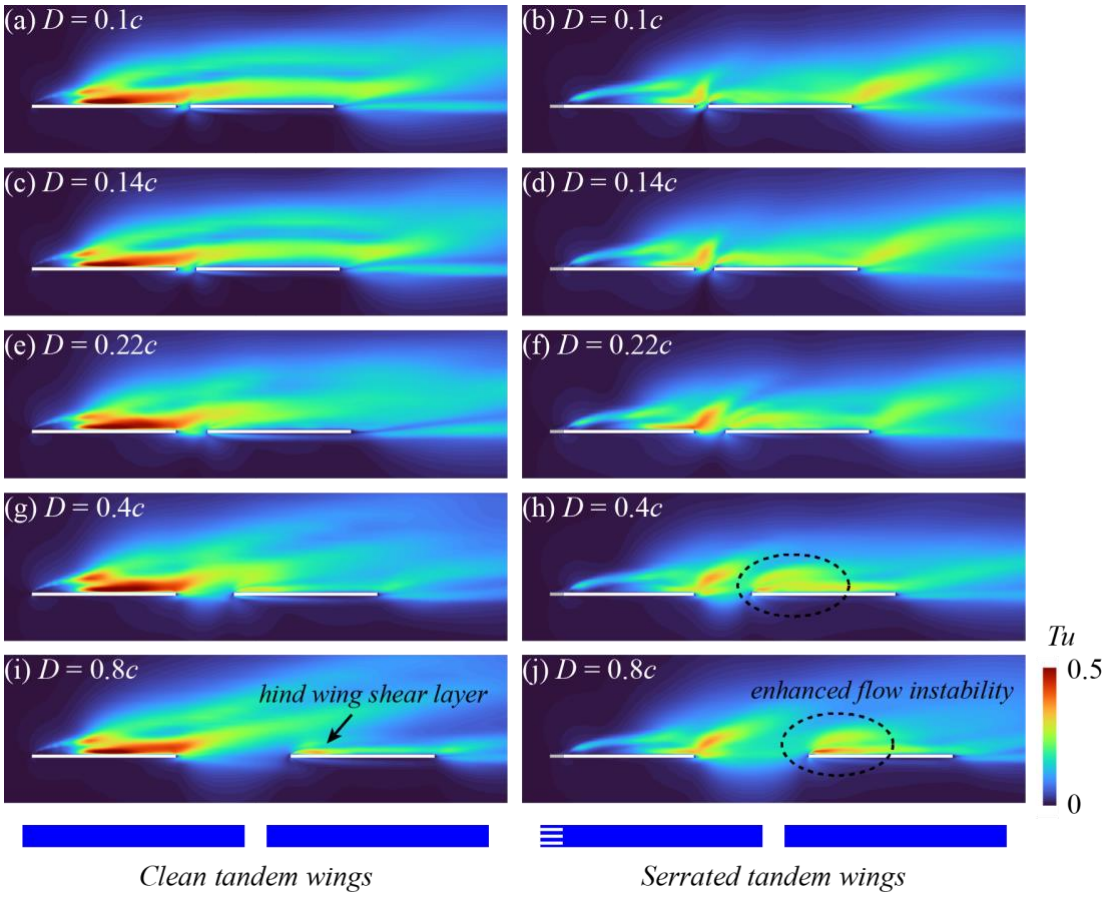

Fig. 4-11. Contours of chordwise velocity fluctuations (T_u) around clean (left) and serrated (right) tandem wing models at various gap distances (*D*) for *AoA* = 5°.

To further investigate the LE serration effects with respect to the passive control of the laminar-turbulent transition (Fig. 4-10) and flow instability (Fig. 4-11), the

distributions of T_u are compared between the clean and serrated tandem wings along 6 lines (black dashed lines in Fig. 4-12) located at $x_{n|n=1,2} =$ 0.3c, 0.6c, and 0.9c, where x_1 and x_2 are the local coordinates of the fore and hind wings, respectively.

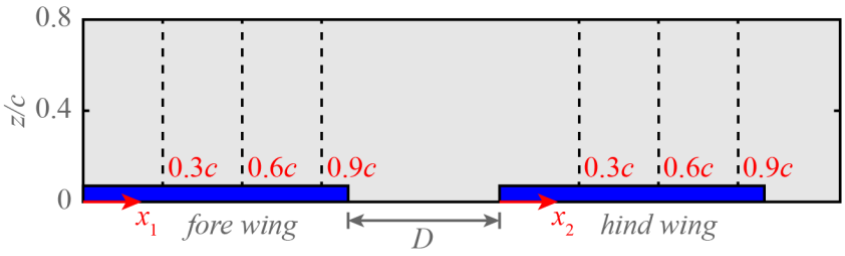

Fig. 4-12. Illustration of local coordinate systems of fore wing (x_1) and hind wing (x_2).

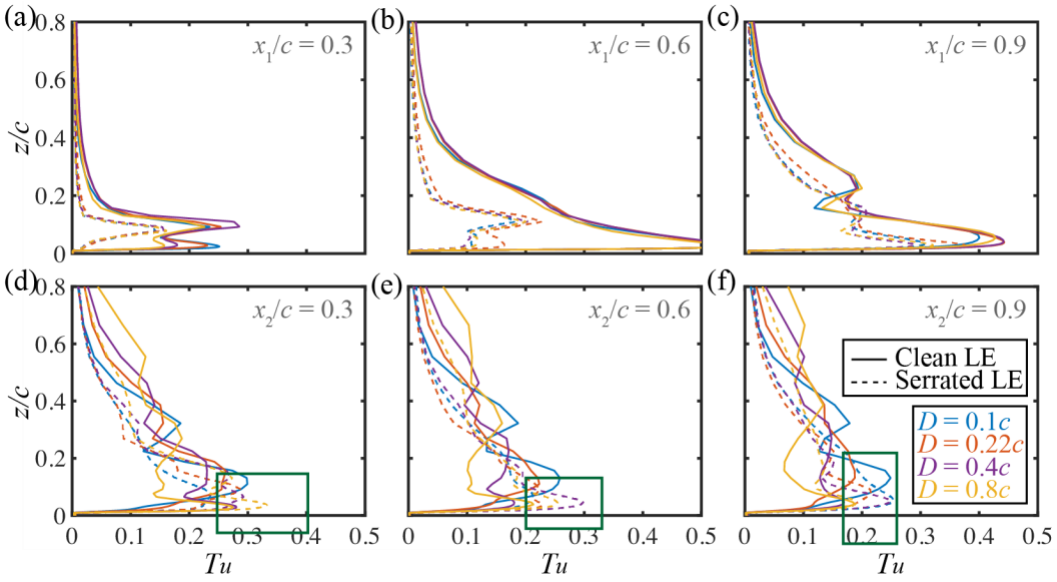

Fig. 4-13. Comparison of chordwise velocity fluctuations (T_u) at 6 positions between clean and serrated tandem wing models at *AoA* = 5°. Positions for comparison are $x_1 =$ (a) 0.3c, (b) 0.6c, and (c) 0.9c for fore wing and $x_2 =$ (d) 0.3c, (e) 0.6c, and (f) 0.9c for hind wing.

In Fig. 4-13, the results of tandem wing models with small gap distances of 0.1c and 0.22c and large gap distances of 0.4c and 0.8c are plotted. It is seen that for the fore wing [Figs. 4-13(a), 4-13(b), and 4-13(c)], the intense flow fluctuations are suppressed by the serrations throughout the upper surface in all cases, particularly in the region of mid-chord [dashed lines in Fig. 4-13(b)]. This indicates that the LE serrations can effectively alter the

laminar-turbulent transition on the fore wing upper surface and thus lead to enhanced stability of the suction flow. Whereas for the hind wing [Figs. 4-13(d), 4-13(e), and 4-13(f)], the fore wing serrations can solely suppress the near-wall fluctuations at a small D of 0.1c (green rectangles in Fig. 4-13). At a large D (e.g., 0.4c, 0.8c), the near-wall fluctuations are enhanced, resulting in a pronounced increase in the far-field OASPLs [Fig. 4-7(c)].

We then visualize the near-field vortical structures for the tandem wings with and without serrations (D = 0.1c and 0.4c) at AoA = 5° to examine the swirling features of the laminar-turbulent transition and the mechanisms of flow stabilization. Note that the two gap distances correspond to the cases of sound reduction and sound enhancement due to the serrations, respectively. The vortical structures around the tandem wings are identified by the instantaneous iso-surface of the Q criterion. The swirling features of the vortices are characterized by the chordwise vorticity.

As illustrated in Fig. 4-14, an immediate laminar boundary layer separation can be observed at the LE of the clean tandem wing model [Figs. 4-14 (a) and 4-14(c)]. The separated boundary layer then reattaches onto the upper surface at approximately the mid-chord of the fore wing, forming a separation bubble and transitioning to turbulence, substantially leading to vortex shedding. When the gap distance D is small (0.1c) [Fig. 4-14(a)], the vortices shedding from the fore wing roll over the hind wing upper surface and dominate the vortex dynamics of the hind wing. Whereas for the large D of 0.4c [Fig. 4-14(c)], those vortices coming from the fore wing (i.e., the incoming flow for the hind wing) wash directly onto the hind wing LE and interact violently with the hind wing surfaces, causing noticeable flow instability at the hind wing LE [Fig. 4-11(g)]. The serrated tandem wing model, however, effectively breaks up the large-scale vortices into small eddies at the LE of the fore wing, leading to a relatively stable suction flow without an obvious reattachment [Figs. 4-14(b) and 4-14(d)]. Due to the breakup of LE vortices, the aerodynamic performance of the tandem wings is weakened [Figs. 4-4(a) and 4-4(c)]. For the case of small D (0.1c) [Fig. 4-14(b)], the hind wing seems to inherit the mitigated vortex flow from the fore wing, hence achieving enhanced stability of suction flow [Fig. 4-11(b)]. However, for the case of large D (0.4c) [Fig. 4-14(d)], the fore wing serrations seem to intensify the interaction of the fore wing wake and hind wing LE, thus enhancing

the flow instability in the vicinity [Fig. 4-11(h)].

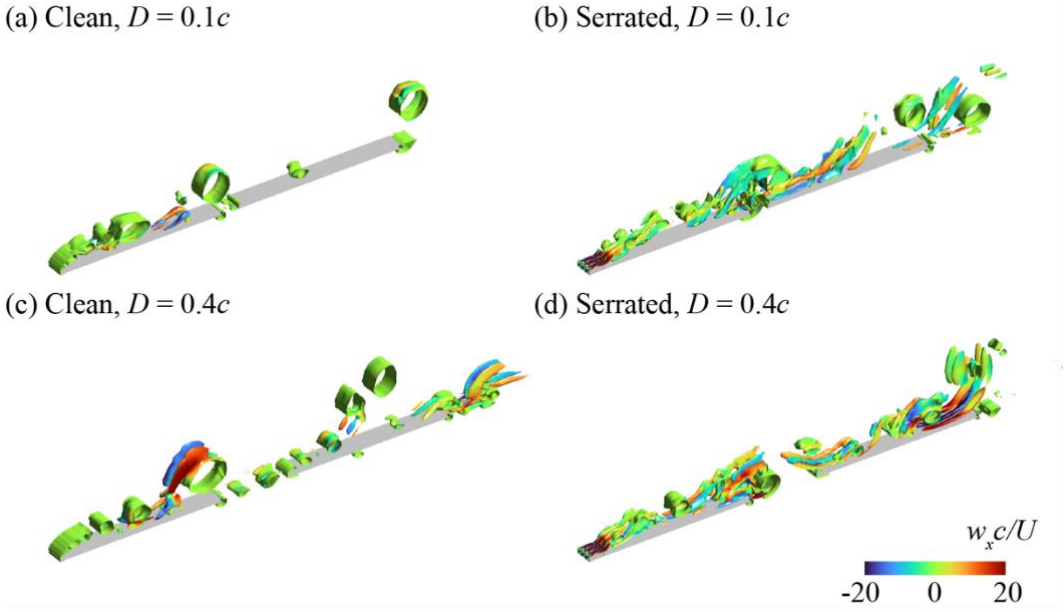

Fig. 4-14. Iso-contours of normalized Q = 25 of clean (left) and serrated (right) tandem wing models at gap distances (D) of 0.1c (top) and 0.4c (bottom) for AoA = 5° .

Given that the far-field OASPLs are in close association with the near-wall pressure fluctuations [50, 51], we visualize the fluctuations of pressures around the clean and serrated tandem wing models at AoA = 5° to evaluate the intensity of acoustic sources. Here, the pressure fluctuations are identified by the RMS of the fluctuating pressures (P'). As illustrated in Fig. 4-15, it is found that the serrations on the fore wing can remarkedly reduce pressure fluctuations over the fore wing while suppressing fluctuations over the hind wing when D is small [Figs. 4-15(b) and 4-15(d)]. However, as D increases, the fluctuations over the hind wing are gradually enhanced by the serrations (particularly at the LE of the hind wing) [Figs. 4-15 (h) and 4-15(j)], thus increasing the far-field sound [Fig. 4-7(c)].

Here we infer that there are two sound mechanisms for tandem wings at a low AoA of 5°, i.e., shear layer instability-induced fore wing flow fluctuations and vortex-LE interaction-induced hind wing fluctuations. The owl-inspired LE serrations distributed on the fore wing are effective in suppressing the fore wing flow instability by passively controlling the laminar-turbulent transition but simultaneously enhance the instability at

the hind wing LE (Fig. 4-15). The fluctuations at the hind wing LE can even be the dominant acoustic mechanism when the gap distance of the tandem wings is large [Figs. 4-15(h), 4-15(j)]. Thus, the far-field OASPLs of the tandem wings are initially reduced but then increased by the fore wing serrations as the gap distance increases from small to large [Fig. 4-7(c)].

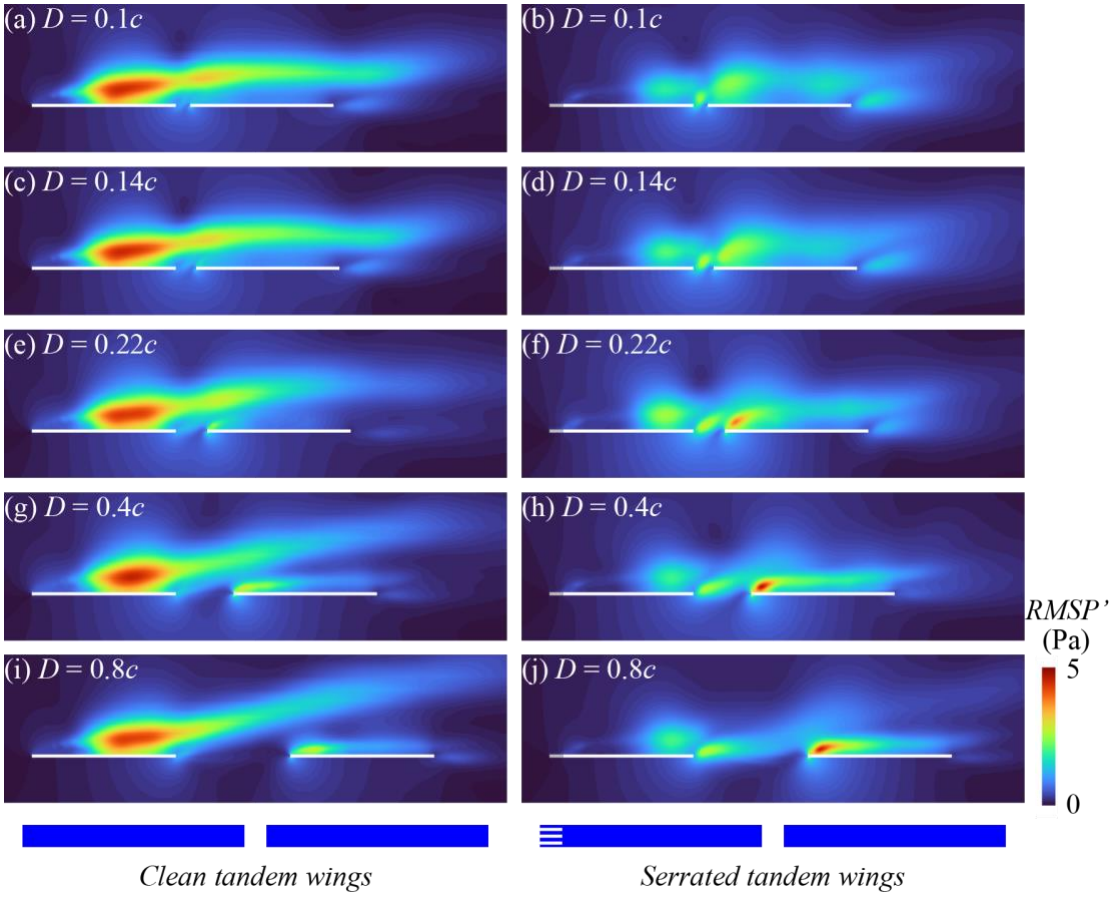

Fig. 4-15. Contours of pressure fluctuations around clean (left) and serrated (right) tandem wing models at various gap distances (*D*) for *AoA* = 5°.

4.4.2 High-AoA aerodynamic characteristics

At the high *AoA* of 15°, the fore wing serrations are observed to robustly reduce the far-field OASPLs of tandem wings [Figs. 4-7(d), 4-7(e), and 4-7(f)] while sustaining comparable aerodynamic forces compared to that of clean tandem wings [Figs. 4-4(d), 4-4(e), and 4-4(f)]. This is obviously distinguished from the characteristics at the low *AoA*

of 5°. Therefore, we further give an investigation on the mechanisms associated with LE serrations in sound reduction by visualizing the flow characteristics around the clean and serrated tandem wing models at *AoA* = 15°. The results of tandem wings with four different gap distances (0.22*c*, 0.4*c*, 0.8*c*, and 1.0*c*) are analyzed.

We first visualize the distributions of time-averaged chordwise velocities around the clean and serrated tandem wings at *AoA* = 15° (Fig. 4-16). It is found that at such a high *AoA*, the flow separation at the fore wing LE is much more pronounced (Fig. 4-16), resulting in a similar nature in the near-field flow structures for the clean and serrated tandem wings, leading to their comparable aerodynamic performance [Fig. 4-4(f)]. In addition, there is no flow reattachment for the clean and serrated tandem wings and a large-scale separated boundary layer can be observed at the hind wing TE, which may enhance the flow instability [25].

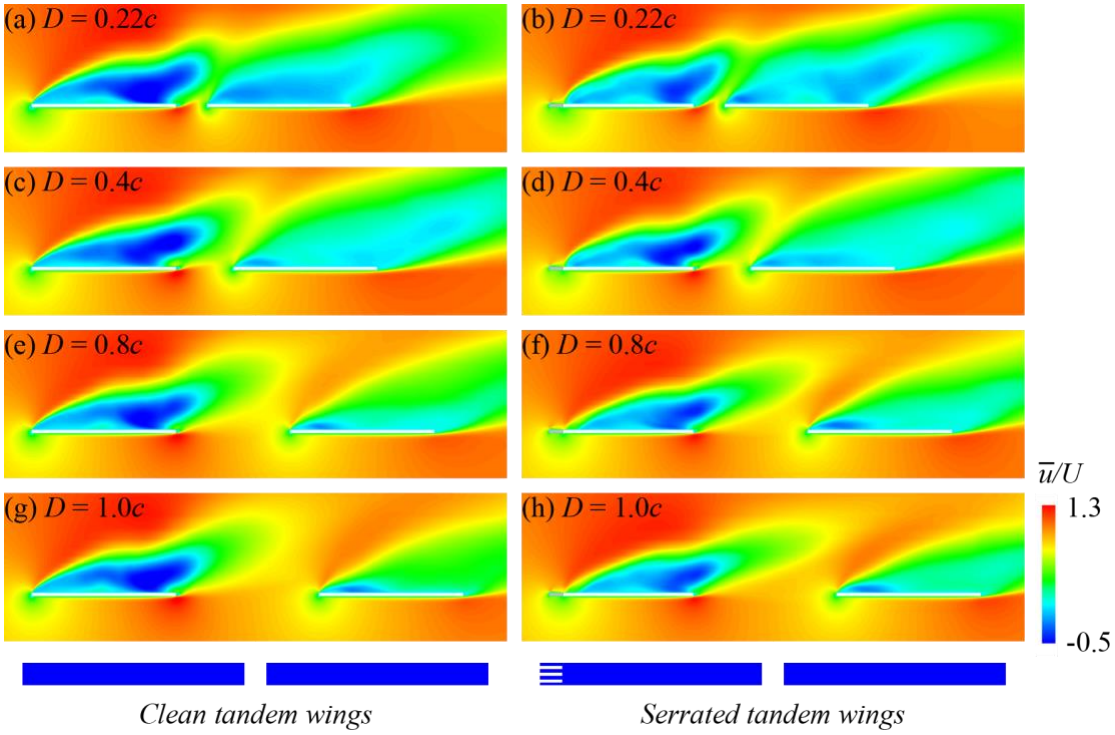

Fig. 4-16. Contours of time-averaged chordwise velocities normalized by freestream velocity U_∞ around clean (left) and serrated (right) tandem wing models at various gap distances (*D*) for *AoA* = 15°.

The fluctuations of the flow fields however remain noticeably different for the clean and serrated tandem wings. As shown in Fig. 4-17, in the clean tandem wing model,

intense fluctuations of velocities are observed at the fore wing TE due to the large-scale separated boundary layer (Fig. 4-16) [25]. The fluctuations exhibit a clear double-peak feature of distributions and are more pronounced at larger gap distances [Figs. 4-17(a), 4-17(c), 4-17(e), and 4-17(g)]. Meanwhile, as observed in the cases of low *AoA* (Fig. 4-11), intense fluctuations are induced at the hind wing LE as the gap distance increases [Figs. 4-17(e) and 4-17(g)], which are induced by the interaction of the wake of the fore wing and the suction flow of the hind wing. In the serrated tandem wing model, however, the strong fluctuations at the fore wing TE and hind wing LE are simultaneously suppressed by the serrations in all cases [Figs. 4-17(b), 4-17(d), 4-17(f), and 4-17(h)], resulting in robust sound reductions for the fore, hind, and tandem wings at the high *AoA* [Figs. 4-7(d), 4-7(e), and 4-7(f)]. This implies that at such a high *AoA*, the LE serrations seem to enable mitigating the flow interaction at the hind wing LE robustly, even with large gap distances.

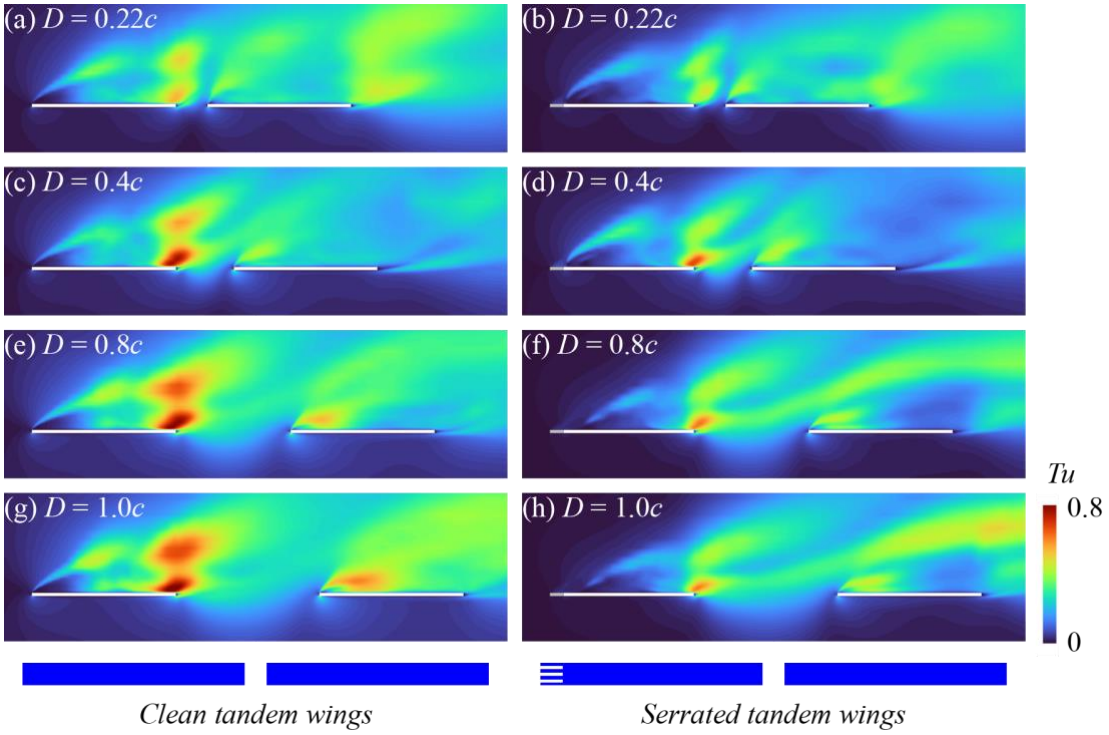

Fig. 4-17. Contours of chordwise velocity fluctuations (T_u) around clean (left) and serrated (right) tandem wing models at various gap distances (D) for *AoA* = 15°.

The velocity fluctuations of the clean and serrated tandem wing models are further plotted at the 6 positions (defined in Fig. 4-12). As seen in Fig. 4-18, for the fore wing, the

suction flow instability is remarkably suppressed by the serrations throughout the upper surface in all cases, particularly in the downstream region (i.e., from mid-chord to TE) [Figs. 4-18(a), 4-18(b), and 4-18(c)]. Meanwhile, the flow fluctuations on the hind wing surfaces are also effectively suppressed, particularly in the near-wall region [Figs. 4-18(d), 4-18(e), and 4-18(f)]. This demonstrates the robustness of the serrations in suppressing flow instability at the high *AoA*.

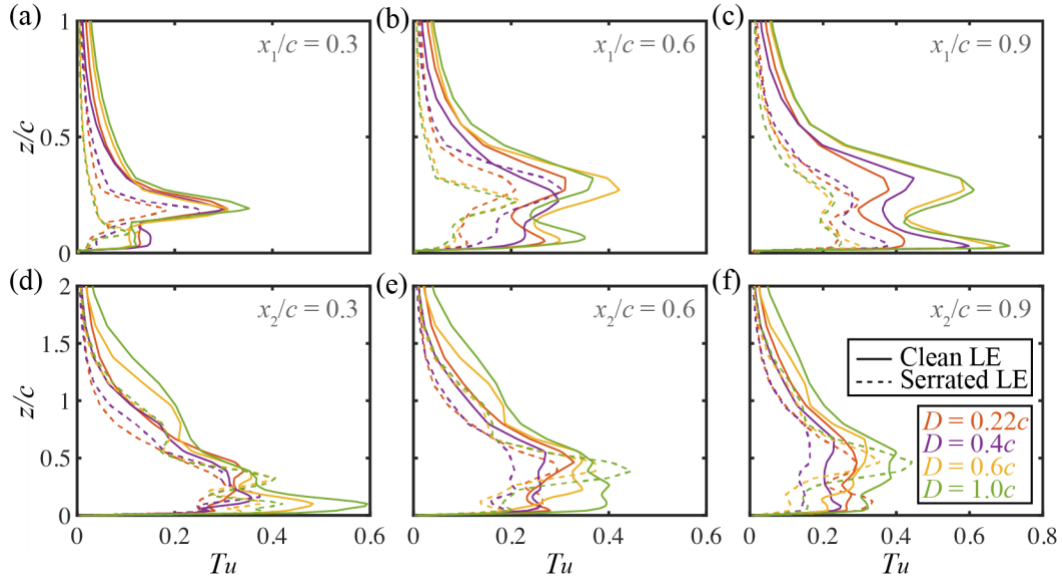

Fig. 4-18. Comparison of chordwise velocity fluctuations (T_u) at 6 positions for clean and serrated tandem wing models at *AoA* = 15°. Positions for comparison are $x_1 =$ (a) 0.3*c*, (b) 0.6*c*, and (c) 0.9*c* for fore wing and $x_2 =$ (d) 0.3*c*, (e) 0.6*c*, and (f) 0.9*c* for hind wing.

To clarify the mechanisms associated with the LE serration effects in terms of flow stabilization and sound reduction at *AoA* = 15°, the near-field vortex structures of the clean and serrated tandem wing models are shown in Fig. 4-19. At the LE of the clean fore wing [Figs. 4-19(a) and 4-19(c)], a pronounced flow separation is observed, which causes vortex shedding of the separated shear layer. The shedding vortices roll rapidly downstream and interacts with the fore wing TE vortices, inducing strong flow instability at the TE of the fore wing [Figs. 4-17(a) and 4-17(c)]. Unlike the cases at the low *AoA* (Fig. 4-14), at such a high *AoA* of 15°, the shedding vortices from the fore wing seem to avoid washing directly onto the LE of the hind wing and instead interact/merge with the vortices shedding from the hind wing LE, causing a series of vortices to roll away rapidly over the hind wing

suction surface, eventually breaking up and rolling into the tandem wing wake. On the other hand, for the serrated tandem wing model, the serrations distributed on the LE of the fore wing effectively break up the large-scale LE vortices [Figs. 4-19(b) and 4-19(d)], hence suppressing and mitigating the vortex shedding of the fore wing [59, 112]. As a consequence, both the vortex-vortex interactions near the fore wing TE and the hind wing LE are scattered and mitigated, resulting in enhanced flow stability [Fig. 4-17] and robust sound reductions [Fig. 4-7(f)].

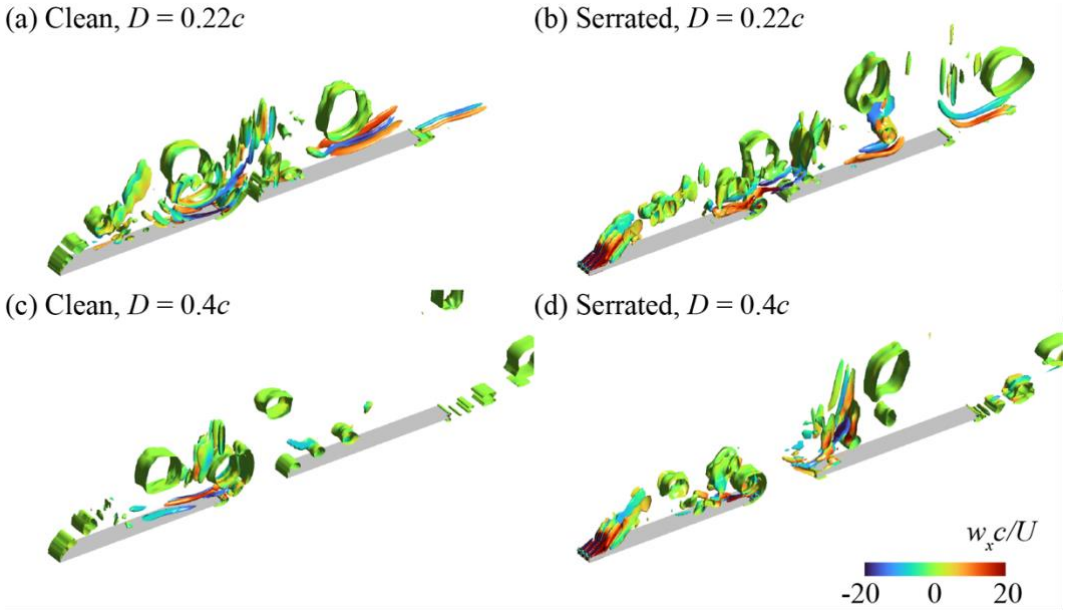

Fig. 4-19. Iso-contours of normalized Q = 25 of clean (left) and serrated (right) tandem wing models at gap distances (D) of 0.1c (top) and 0.4c (bottom) for AoA = 15°.

Figure 4-20 illustrates the pressure fluctuations surrounding the clean and serrated tandem wings at AoA = 15°. From Fig. 4-20, when D is small (e.g., 0.22c), the sound of the tandem wings is mainly induced by the intense fluctuations at the TEs of the fore and hind wings. As D increases (e.g., 0.4c, 0.8c, and 1.0c), the fluctuations at the hind wing LE gradually become intense due to the violent vortex interaction. The fluctuations at the hind wing LE are even dominant over the fore wing TE fluctuations when D is 1.0c [Figs. 4-20(g) and 4-20(h)]. However, they are both attenuated by the serrations in all cases, demonstrating the robust acoustic performance of LE serrations at the high AoA of 15° [Figs. 4-20(b), 4-20(d), 4-20(f), and 4-20(h)].

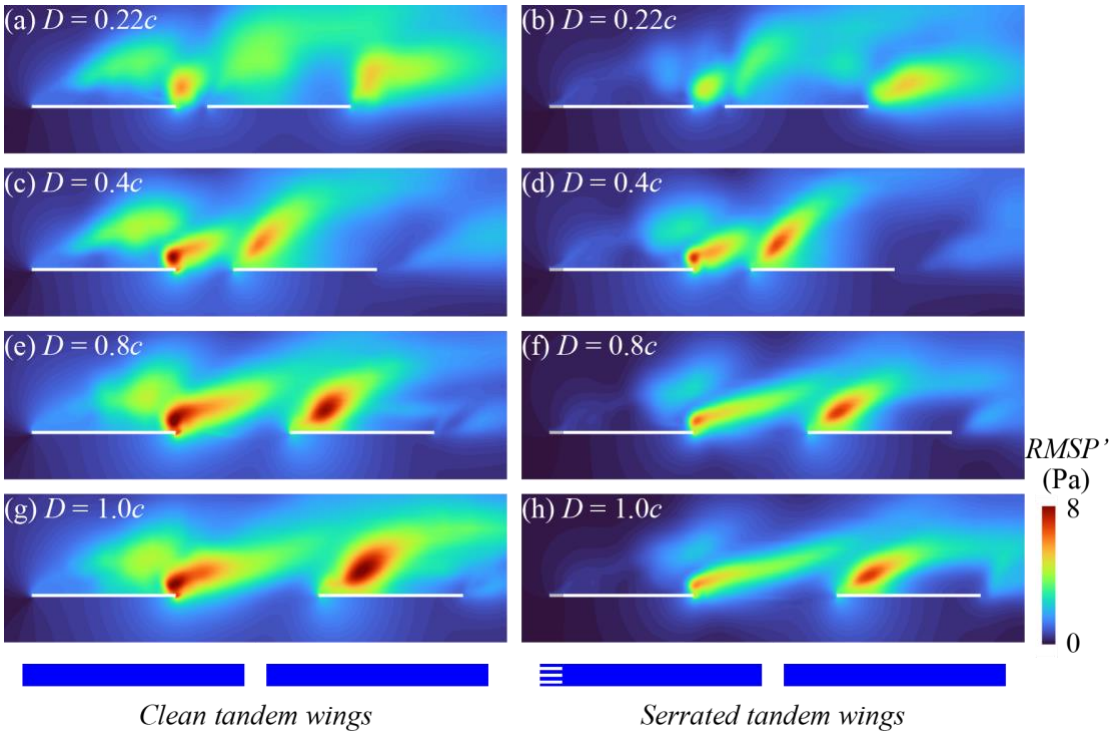

Fig. 4-20. Contours of pressure fluctuations around clean (left) and serrated (right) tandem wing models at various gap distances (D) for AoA = 15°.

4.5 Hind wing LE-serration-induced sound reduction

As described in Sec. 4.3–Sec. 4.4, the owl-inspired LE serrations of the fore wing can significantly alter the tandem wing aeroacoustics in terms of the feather-feather (feather slots) interactions. There are also LE serrations observed on other primary feathers, such as the 9th and 8th primary feathers [P9 and P8, see Fig. 4-1(b)] [24, 63]. These serrations act as hind wing LE-serrations and may be responsible for reducing the flow instability in the vicinity of the hind wing LE (Figs. 4-15 and 4-20). To gain a comprehensive understanding of the influence of this multiple LE serrations-based wing morphology in the silent flight of owls, we further constructed a tandem wing model with LE serrations on both the fore and hind wings [Fig. 4-21(a)].

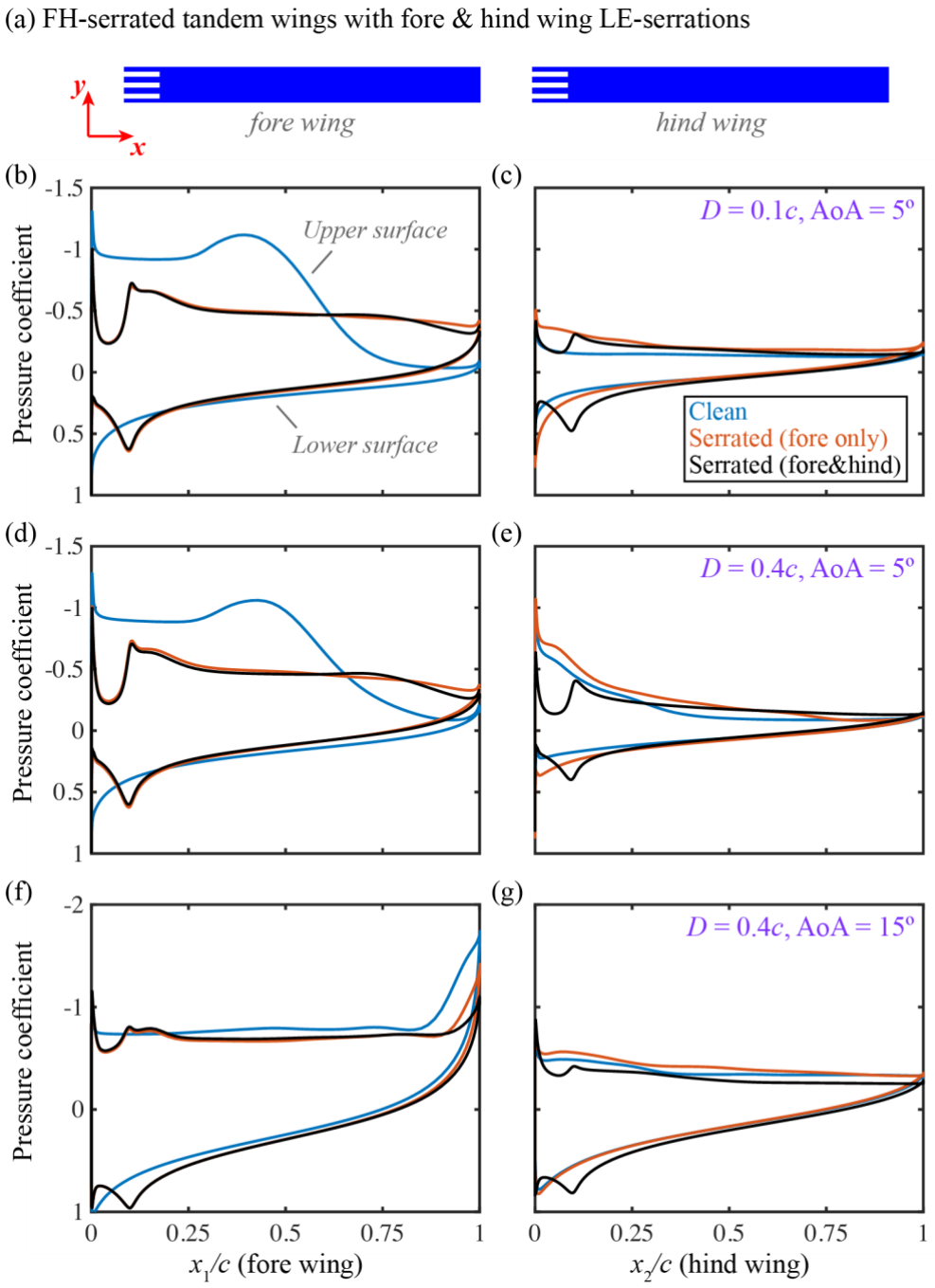

Fig. 4-21. (a) FH-serrated tandem wing model with serrations on LEs of fore and hind wings. (b)–(g) Comparison of time-averaged pressure coefficients on fore (left: (b), (d), (f)) and hind (right: (c), (e), (g)) wing surfaces for clean, serrated, and FH-serrated tandem wing models under different flow conditions: D = 0.1c and AoA = 5° (top), D = 0.4c and AoA = 5° (middle), and D = 0.4c and AoA = 15° (bottom).

For clarity, the new tandem wing model with both fore-and hind-wing LE-serrations is referred to as the FH-serrated tandem wing model [Fig. 4-21(a)]. In addition, the geometric parameters of the hind wing serrations are taken the same as those of the fore wing serrations, as described in Table 4-1. The results computed under three typical flow conditions [i.e., D = 0.1c and AoA = 5° (small gap distance and low AoA), D = 0.4c and AoA = 5° (large gap distance and low AoA), and D = 0.4c and AoA = 15° (high AoA)] are employed to investigate the aeroacoustic characteristics of the hind wing serrations.

First, the distributions of time-averaged C_p on the fore and hind wing surfaces are compared for the clean, serrated, and FH-serrated tandem wing models under the three flow conditions. As depicted in Fig. 4-21, by comparing the results of the serrated (red lines) and FH-serrated (black lines) tandem wings, we find that their pressure distributions on the fore wing surface are very close at AoAs of 5° and 15° [Figs. 4-21(b), 4-21(d), and 4-21(f)], implying that the hind wing serrations do not exert noticeable influence on the upstream flow. Whereas for the hind wing, the pressure differences at the LE are slightly reduced by the hind wing serrations in all cases [Figs. 4-21(c), 4-21(e), and 4-21(g)]. Thus, the FH-serrated tandem wing model presents similar aerodynamic performance with those of the serrated tandem wing model, i.e. which is lowered at AoA = 5° but comparable at AoA = 15° compared to the clean tandem wing model.

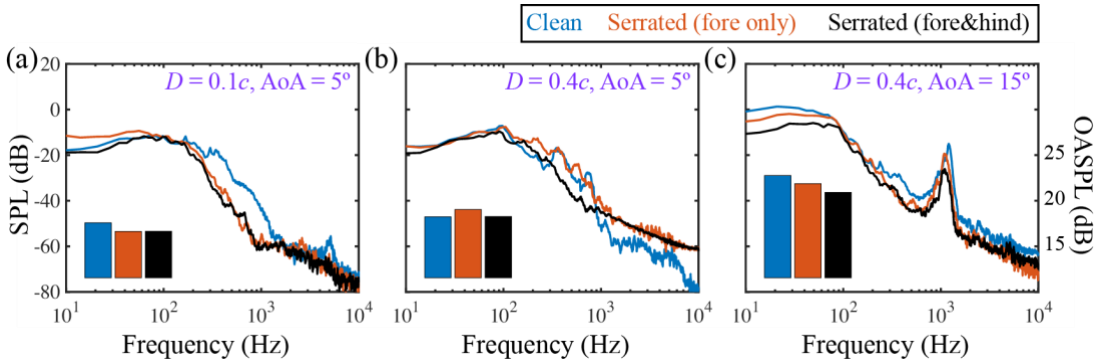

Fig. 4-22. Comparison of sound pressure spectra at R4 for clean, serrated, and FH-serrated tandem wing models at (a) D = 0.1c and AoA = 5°, (b) D = 0.4c and AoA = 5°, and (c) D = 0.4c and AoA = 15°. Bars denote OASPLs integrated over frequency range for three models.

Next, the effects of hind wing serrations on tandem wing acoustic characteristics are examined by comparing the sound pressure spectra and OASPLs among the clean, serrated,

and FH-serrated tandem wing models under the three flow conditions. As depicted in Fig. 4-22, by comparing the results between the serrated (red lines) and FH-serrated (black lines) tandem wing models, we find that the hind wing serrations exert almost no influence on the high-frequency sound ($f >$ 1000 Hz). However, at the low- and mid-frequencies (10~1000 Hz), the hind wing serrations can powerfully suppress SPLs in all cases, achieving more pronounced sound reductions compared to that of the serrated tandem wing model. Particularly, in the case of D = 0.4c and AoA = 5°, while the fore wing serrations increase the OASPLs of the tandem wings [Fig. 4-7(c)], the hind wing serrations effectively suppress the mid-frequency sound, presenting a robust sound reduction capacity [bars in Fig. 4-22(b)].

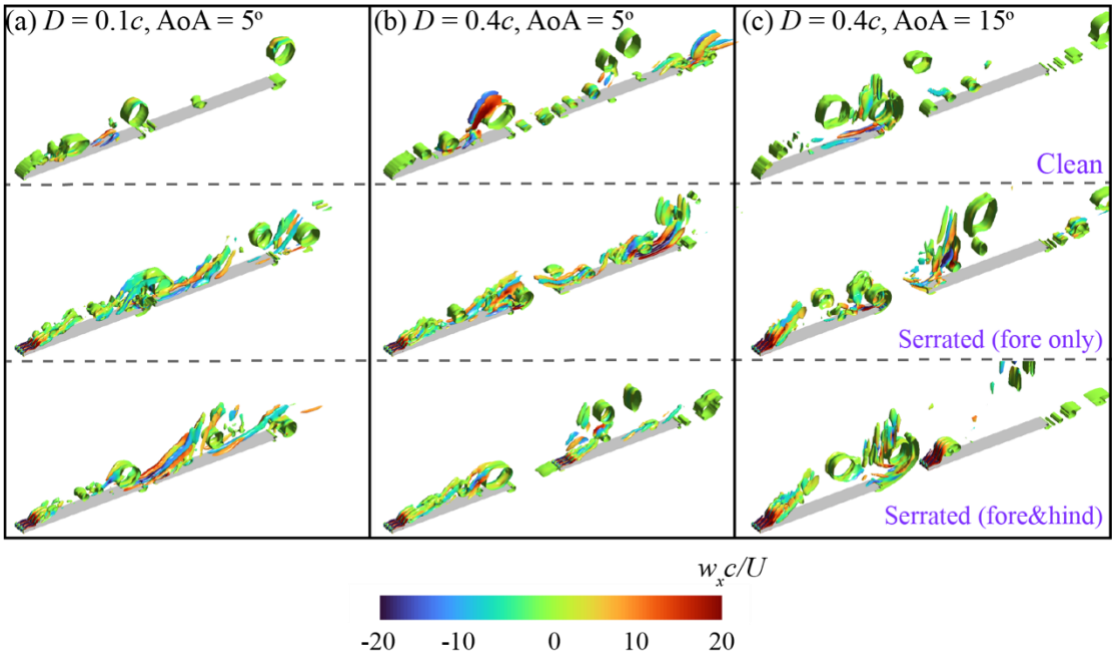

Fig. 4-23. Iso-contours of normalized Q = 25 of clean (top), serrated (middle), and FH-serrated (bottom) tandem wing models at (a) D = 0.1c and AoA = 5°, (b) D = 0.4c and AoA = 5°, and (c) D = 0.4c and AoA = 15°.

To clarify the effects of the hind wing serrations on vortex breaking and flow stabilization, we further visualized the vortical structures and pressure fluctuations surrounding the clean, serrated (fore wing only), and FH-serrated tandem wing models as illustrated in Fig. 4-23 and Fig. 4-24, respectively. As seen in Fig. 4-23(a), at D = 0.1c and

AoA = 5°, the vortex-breaking effect of the hind wing serrations is apparently a marginal, and the fore wing-induced wake dominates the flow characteristics of the hind wing, resulting in the similar flow fields for the serrated and FH-serrated tandem wing models [Fig. 4-24(a)]. Because of the fore wing serrations-induced suction flows, the serrated (fore wing only) and FH-serrated tandem wings can both achieve remarkable sound reductions compared to the clean tandem wings [Fig. 4-22(a)]. In the other two cases of $D = 0.4c$ [Figs. 4-23(b) and 4-23(c)], however, the LE serrations on the hind wing are observed capable of effectively breaking up the hind wing LE vortices, mitigating the vortex interaction in the vicinity of the hind wing LE. Consequently, the intense pressure fluctuations at the hind wing LE are suppressed significantly [Figs. 4-24(b) and 4-24(c)], leading to robust and powerful sound reductions for the FH-serrated tandem wing model [Figs. 4-22(b) and 4-22(c)].

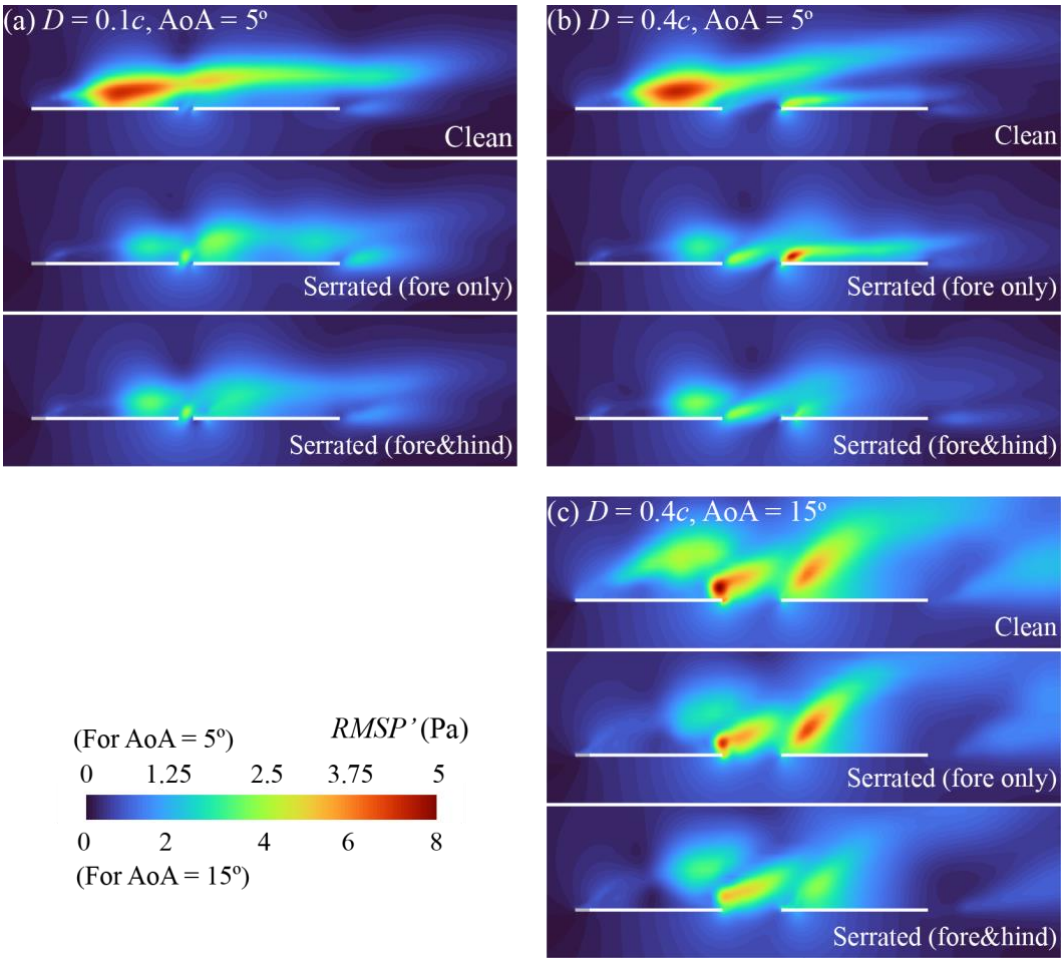

Fig. 4-24. Contours of pressure fluctuations around clean, serrated, and FH-serrated tandem wing

models at (a) $D = 0.1c$ and $AoA = 5°$, (b) $D = 0.4c$ and $AoA = 5°$, and (c) $D = 0.4c$ and $AoA = 15°$.

In summary, the LE serrations are verified to alter the aeroacoustic characteristics of the feather-feather interactions. Note that in this study we neglected the 3D effects (e.g., induced by wingtip vortex) for the sake of simplicity. An owl-inspired 3D wing model will be investigated to reveal the 3D effects of LE serrations on the feather-feather interactions. In addition, the silent flight of owls is achieved through integrating various factors comprising LE serrations, TE fringes, velvety wing surfaces, wing flexibility, highly-cambered airfoil-based cross sections [98, 101], and the feather slots, which likely work complementarily with each other [94, 112]. Thus, what are the underlying aeroacoustics mechanisms in association with a real wing of owls characterized by the combination of these morphological features may be a central while challenging problem, which will be tackled as our future task through a combination of direct PIV measurements and three-dimensional LESs.

4.6 Summary

This section presents a simulation-based study of the aeroacoustic characteristics in terms of feather-feather (feather slots) interactions, in association with tandem wing models with clean and owl-inspired serrated leading-edges. The aeroacoustic simulations were conducted by loosely coupling the LES modeling and the FW-H analogy at a low Reynolds number of 6000. The aeroacoustic analysis is focused specifically on the effects of the gap distance (D) between fore and hind wings on the tandem wing aeroacoustics. The key findings are summarized as follows:

(1) The fore wing LE serrations exert a remarkable influence on the aeroacoustic characteristics of the tandem wings: at the low AoA of 5°, with increasing gap distrance D, the far-field OASPLs of the tandem wings have a trend to initially decline at $D < 0.22c$ but then turn to increase when $D > 0.22c$; at the high AoA of 15°, a consistent and robust sound reduction is observed for all gap distances with no detrimental effect on the aerodynamic performance.

(2) With respect to the aeroacoustic mechanisms of the fore wing LE serrations at the

low *AoA* of 5°, it is verified that at small $D < 0.22c$, the LE serrations enable passively controlling the boundary layer characteristics on the fore wing upper surface, consequently enhancing the suction flow stability in association with both fore and hind wings. At larger $D > 0.22c$, the fore wing LE serrations however increase the flow instability near the hind wing LE due to the vortex-hind wing interactions, significantly increasing the far-field OASPLs.

(3) The aeroacoustic mechanisms of the fore wing LE serrations at the high *AoA* of 15° involves the break-up of the large-scale vortices and the suppression of the shed vortex intensity by the fore wing serrations, which remarkedly weakens the flow interactions near the fore wing TE and the hind wing LE, consequently enhancing the suction flow stability of the tandem wings and hence reducing the sound level.

(4) The interplay between the fore and hind wings with both LE serrated can benefit the aeroacoustic performance of the FH-serrated tandem wings: the LE serrations attached onto the hind wing can further facilitate the suppression of flow fluctuations near the hind wing LE through breaking the hind wing LE vortices, mitigating the vortex interaction, and consequently reducing the low- and mid-frequency sound. Thus, the FH-serrated tandem wings can robustly reduce sound while paying less cost on aerodynamic loss at low *AoA*s.

Our results demonstrate that the aeroacoustic interaction between fore and hind wings inspired by feathers or feather slots in owls' flight can be altered remarkedly by owl-inspired LE serrations, which is closely associated with the gap distance between the fore and hind wings. This study thus points to the potential capabilities of combining the fore and hind wing serrations in association with tandem wings to provide an effective and robust biomimetic design for low-noise fluid machinery comprising multirotor drones and wind turbines.

5 Conclusion

5.1 Summary of contributions

This thesis describes an integrated aeroacoustic study of owl-inspired wings for biomimetic design of 'silent' flights. The aeroacoustic characteristics of wing models with owl-inspired LE serrations and TE fringes were resolved by loosely coupling the LES modeling and the FW-H analogy at a low Reynolds number of 6000. The aeroacoustic analysis is focused specifically on the aeroacoustic interaction between TE fringes and LE serrations, the 3D aeroacoustic characteristics induced by TE fringes, and the LE serration effects on feather-feather (feather slots) interactions. The main contributions and findings are summarized as follows:

(1) The aeroacoustic interaction between owl-inspired LE serrations and TE fringes is revealed. Using owl-inspired (2D) LE serrated and TE fringed models, it is verified that TE fringes enable a pronounced high-frequency sound reduction at *AoA*s of 5–15° while achieving comparable aerodynamic performance to a clean model. The near-field vortex dynamics, pressure distributions, and velocity spectra reveal that TE fringes suppress flow separation and vortex shedding in the vicinity of the TE, consequently reducing local velocity fluctuations and far-field overall sound pressure levels. Furthermore, the combination of TE fringes and LE serrations enables a remarkable reduction in overall sound pressure levels at all *AoA*s, and their aeroacoustic interplay is responsible for stabilizing velocity fluctuations over the suction surface, which suppress both low- and high-frequency sound. Our results demonstrate that TE fringes are a robust sound reduction device in resolving the tradeoff between aerodynamic force production and sound reduction, while LE serrations and TE fringes complement one another as an effective noise-reducing biomimetic design.

(2) The 3D aeroacoustic characteristics and distribution effects of owl-inspired TE fringes are resolved. We constructed a clean wing model and three wing models with TE fringes that were distributed differently spanwise. The aerodynamic forces and 3D acoustic

characteristics reveal that, like the 2D results, the 3D TE fringes enable remarkable sound reduction spatially while having aerodynamic performance comparable to the clean model. Visualizations of the near-field 3D flow structures, vortex dynamics, and flow fluctuations show that TE fringes can robustly alter the 3D flow by breaking 3D TE vortices into small eddies and mitigating 3D flow fluctuations. Particularly, it is verified that TE fringes alter spanwise flows, thus dominating the 3D aeroacoustic characteristics in terms of passive flow control and flow stabilizations, whereas the fringes are inefficient in suppressing the acoustic sources induced by wingtip vortices. Moreover, the TE fringes distributed at midspan have better acoustic performance than those in the vicinity of the wingtip, indicating the importance of a spanwise distribution in enhancing aeroacoustic performance.

(3) The effects of LE serrations on feather-feather (feather slots) interaction are investigated. The aeroacoustic characteristics of a tandem wing model with owl-inspired serrations on the LEs of the fore and hind wings were resolved. The results demonstrate that serration-induced aeroacoustics are closely associated with the gap distance (D) between fore and hind wings. At a low *AoA* of 5°, as D increases, the LE serrations on the fore wing initially reduce the far-field sound pressures ($D < 0.22c$) through passively altering the laminar-turbulent transition on upper wing surfaces but turn out to increase the sound pressures remarkedly when $D > 0.22c$ due to the flow instability induced at the hind wing LE. However, at a high *AoA* of 15°, the fore wing serrations enable robust sound reductions for all gap distances through mitigating the flow instabilities near the fore wing TE and hind wing LE. Furthermore, the combination of LE serrations on fore and hind wings are verified capable of bringing nonlinear synergetic effects on the suppression of flow fluctuations and noise, which can inspire innovative biomimetic designs for low-noise multirotor drones and wind turbines.

5.2 Future work

In this thesis, the unique owl-wing morphologies—TE fringes and LE serrations are verified to play an important role in owls' silent flight through passively controlling airflows around the wings, and the novel biomimetic wings with owl-inspired

fringes/serrations can achieve remarkable sound reduction. Note that in the current work, the single/tandem feather models were simulated at a low *Re*, which is identical to the typical flight speed of an owl's forward flight, to reflect the realistic flow physics around the owl feathers during flight and thus reveal the essential aeroacoustic mechanisms of the LE serrations and TE fringes. More investigations will be conducted as our next work to further unveil the mechanisms associated with owls' silent flight and explore the engineering potential of owl-inspired wings.

(1) 3D simulations using the models of owl wings will be performed. In the current work, models of single/tandem owl feathers are employed, which have been confirmed as capable of revealing the essential mechanisms associated with the serrations/fringes observed on the LEs/TEs of owl feathers [59-61, 71]. However, owl wings are composed of multiple feathers and feather slots. How these small-scale wing morphologies (e.g., serrations and fringes) alter the aeroacoustic characteristics of an owl wing remains unclear. To further reveal the mechanisms of LE serrations and TE fringes during owl flight, 3D wing models with/without LE serrations and TE fringes based on the real geometric features (e.g., wingtip, multiple feather slots, and wavy TE) of an owl wing are being constructed. Then the effects of the LE serrations and TE fringes on owl wing aeroacoustics will be investigated extensively.

(2) The effects of velvety upper wing surface will be studied experimentally. As one of the unique wing morphologies that help owls fly silently, the velvety structure observed on the upper surface of an owl wing may also lead to passive control of the flow and noise of an owl's flight. PIV and force measurements of a real owl wing will be conducted in a low-speed wind tunnel to reveal the effects of the velvety upper surface on boundary layer characteristics, laminar-turbulent transition, and aerodynamic force production.

(3) Potential engineering applications of owl-inspired wings will be explored, while addressing the morphological effects and Reynolds number effects of the owl-inspired morphologies (e.g., serrations and fringes). In the current work, owl-inspired wings are analyzed at a low *Re* of 6000, corresponding to a typical speed of an owl's forward flight [64]. The Reynolds number effects of the LE serrations and TE fringes will be examined in our future work. Then the owl-inspired wings for industrial applications could be designed.

Achievements

Publications:

[1] Rong, J. and Liu, H. Aeroacoustic interaction between owl-inspired trailing-edge fringes and leading-edge serrations. Physics of Fluids. 2022, 34(1): 011907.

[2] Rong, J. and Liu, H. Numerical investigation of three-dimensional aeroacoustic characteristics of owl-inspired trailing-edge fringes. Journal of Bionic Engineering, 2022.

[3] Rong, J. and Liu, H. Effects of owl-inspired leading-edge serrations on tandem wing aeroacoustics. AIP Advances. 2022, 12(11): 115103.

Participated conferences:

[1] Rong, J. and Liu, H. Owl-inspired trailing-edge fringes enable a robust design for noise reduction. The Japan Society of Mechanical Engineering, 33rd Bio-Frontier Seminar, Kobe, 2022.

[2] Rong, J. and Liu, H. Effects of owl-inspired trailing-edge fringes on the three-dimensional aeroacoustic characteristics of a flat plate model. The Society of Aero Aqua Bio-Mechanisms, 8th International Symposium on Aero Aqua Bio-Mechanisms, 2022.

[3] Rong, J. and Liu, H. Owl-inspired trailing-edge fringes enable a robust and versatile biomimetic design for noise reduction. International Society of Bionic Engineering, International Bionic Innovation Competition, 2022.

[4] Rong, J. and Liu, H. Interactive effect of owl-inspired leading-edge serrations and trailing-edge fringes on aerodynamic performance and sound reduction. The Society for Experimental Biology, Annual Conference, 2021.

[5] Rong, J. and Liu, H. Effects of owl-inspired trailing-edge fringes on noise reduction and aerodynamic performance. The Japan Society of Mechanical Engineering, 31st Bio-Frontier Seminar, 2020.

Reference

[1] Gruschka, H.D., Borchers, I.U. and Coble, J.G. Aerodynamic Noise Produced by a Gliding Owl. Nature. 1971, 233(5319): 409-411.

[2] Kroeger, R.A. and Gruschka, H.D. Low Speed Aerodynamics for Ultra-quiet Flight. University of Tennessee Space Institute. 1972.

[3] Sarradj, E., Fritzsche, C. and Geyer, T. Silent Owl Flight: Bird Flyover Noise Measurements. AIAA Journal. 2011, 49(4): 769-779.

[4] Graham, R.R. The Silent Flight of Owls. The Aeronautical Journal. 1934, 38(286): 837-843.

[5] Karabasov, S., Ayton, L., Wu, X., et al. Advances in aeroacoustics research: recent developments and perspectives. Philosophical Transactions of the Royal Society A: Mathematical, Physical and Engineering Sciences. 2019, 377(2159): 20190390.

[6] Choi, H., Park, H., Sagong, W., et al. Biomimetic flow control based on morphological features of living creatures. Physics of Fluids. 2012, 24(12): 121302.

[7] Wei, Y.L., Qian, Y.J., Bian, S.Y., et al. Experimental Study of the Performance of a Propeller with Trailing-Edge Serrations. Acoustics Australia. 2021, 49(2): 305-316.

[8] Al Tlua, B. and Rocha, J. Experimental investigation of NACA-0012 airfoil instability noise with sawtooth trailing edges. Wind Engineering. 2021: 0309524X211060548.

[9] Polacsek, C., Cader, A., Buszyk, M., et al. Aeroacoustic design and broadband noise predictions of a fan stage with serrated outlet guide vanes. Physics of Fluids. 2020, 32(10): 107107.

[10] Lilley, G. A study of the silent flight of the owl. 4th AIAA/CEAS Aeroacoustics Conference. 1998.

[11] Chen, K., Liu, Q.P., Liao, G.H., et al. The Sound Suppression Characteristics of Wing Feather of Owl (Bubo bubo). Journal of Bionic Engineering. 2012, 9(2): 192-199.

[12] Wagner, H., Weger, M., Klaas, M., et al. Features of owl wings that promote silent flight. Interface Focus. 2017, 7(1): 20160078.

[13] Clark, C.J. and Jaworski, J.W. Introduction to the Symposium: Bio-Inspiration of Quiet Flight of Owls and Other Flying Animals: Recent Advances and Unanswered Questions. Integrative and Comparative Biology. 2020, 60(5): 1025-1035.

[14] Jaworski, J.W. and Peake, N. Aeroacoustics of Silent Owl Flight. Annual Review of Fluid Mechanics. 2020, 52(1): 395-420.

[15] Bachmann, T. and Wagner, H. The three-dimensional shape of serrations at barn owl wings: towards a typical natural serration as a role model for biomimetic applications.

Journal of Anatomy. 2011, 219(2): 192-202.
[16] Narayanan, S., Chaitanya, P., Haeri, S., et al. Airfoil noise reductions through leading edge serrations. Physics of Fluids. 2015, 27(2): 025109.
[17] Ayton, L.J. and Chaitanya, P. An analytical and experimental investigation of aerofoil–turbulence interaction noise for plates with spanwise-varying leading edges. Journal of Fluid Mechanics. 2019, 865: 137-168.
[18] Turner, J.M. and Kim, J.W. On the universal trends in the noise reduction due to wavy leading edges in aerofoil–vortex interaction. Journal of Fluid Mechanics. 2019, 871: 186-211.
[19] Wang, L., Liu, X.M. and Li, D. Noise reduction mechanism of airfoils with leading-edge serrations and surface ridges inspired by owl wings. Physics of Fluids. 2021, 33(1): 015123.
[20] Bachmann, T., Wagner, H. and Tropea, C. Inner vane fringes of barn owl feathers reconsidered: morphometric data and functional aspects. Journal of Anatomy. 2012, 221(1): 1-8.
[21] Zhu, W.J. and Shen, W.Z. LES tests on airfoil trailing edge serration. Journal of Physics: Conference Series. 2016, 753: 022062.
[22] Vad, J., KoscsÓ, G., Gutermuth, M., et al. Study of the Aero-Acoustic and Aerodynamic Effects of Soft Coating upon Airfoil. JSME International Journal Series C. 2006, 49(3): 648-656.
[23] Zhou, P., Zhong, S.Y. and Zhang, X. On the effect of velvet structures on trailing edge noise: experimental investigation and theoretical analysis. Journal of Fluid Mechanics. 2021, 919: A11.
[24] Bachmann, T., Klan, S., Baumgartner, W., et al. Morphometric characterisation of wing feathers of the barn owl Tyto alba pratincola and the pigeon Columba livia. Front Zool. 2007, 4: 23.
[25] Brooks, T.F. Airfoil Self-Noise and Prediction. NASA-RP-1218. 1989,
[26] Howe, M.S. Aerodynamic noise of a serrated trailing edge. Journal of Fluids and Structures. 1991, 5(1): 33-45.
[27] Howe, M.S. Noise produced by a sawtooth trailing edge. The Journal of the Acoustical Society of America. 1991, 90(1): 482-487.
[28] Azarpeyvand, M., Gruber, M. and Joseph, P. An analytical investigation of trailing edge noise reduction using novel serrations. in 19th AIAA/CEAS Aeroacoustics Conference, Berlin, Germany, Paper No. AIAA-2013-2009. 2013,
[29] Gruber, M., Joseph, P. and Azarpeyvand, M. An experimental investigation of novel trailing edge geometries on airfoil trailing edge noise reduction. in 19th AIAA/CEAS Aeroacoustics Conference, Berlin, Germany, Paper No. AIAA-2013-2011. 2013,
[30] Jones, L.E. and Sandberg, R.D. Acoustic and hydrodynamic analysis of the flow around an aerofoil with trailing-edge serrations. Journal of Fluid Mechanics. 2012, 706: 295-322.

[31] Avallone, F., Pröbsting, S. and Ragni, D. Three-dimensional flow field over a trailing-edge serration and implications on broadband noise. Physics of Fluids. 2016, 28(11): 117101.
[32] Ragni, D., Avallone, F., van der Velden, W.C.P., et al. Measurements of near-wall pressure fluctuations for trailing-edge serrations and slits. Experiments in Fluids. 2018, 60(1): 6.
[33] Avallone, F., van der Velden, W.C.P., Ragni, D., et al. Noise reduction mechanisms of sawtooth and combed-sawtooth trailing-edge serrations. Journal of Fluid Mechanics. 2018, 848: 560-591.
[34] Prigent, S.L., Buxton, O.R.H. and Bruce, P.J.K. Coherent structures shed by multiscale cut-in trailing edge serrations on lifting wings. Physics of Fluids. 2017, 29(7): 075107.
[35] Thomareis, N. and Papadakis, G. Effect of trailing edge shape on the separated flow characteristics around an airfoil at low Reynolds number: A numerical study. Physics of Fluids. 2017, 29(1): 014101.
[36] Zhou, P., Liu, Q., Zhong, S.Y., et al. A study of the effect of serration shape and flexibility on trailing edge noise. Physics of Fluids. 2020, 32: 127114.
[37] Li, D., Liu, X.M., Hu, F.J., et al. Effect of trailing-edge serrations on noise reduction in a coupled bionic aerofoil inspired by barn owls. Bioinspiration & Biomimetics. 2020, 15(1): 016009.
[38] Herr, M. and Dobrzynski, W. Experimental Investigations in Low-Noise Trailing Edge Design. AIAA Journal. 2005, 43(6): 1167-1175.
[39] Herr, M. Design Criteria for Low-Noise Trailing-Edges. 13th AIAA/CEAS Aeroacoustics Conference (28th AIAA Aeroacoustics Conference). 2007,
[40] Herr, M. A Noise Reduction Study on Flow-Permeable Trailing-Edges. 8th ONERA-DLR Aerospace Symposium (ODAS). 2007,
[41] Oerlemans, S., Fisher, M., Maeder, T., et al. Reduction of Wind Turbine Noise Using Optimized Airfoils and Trailing-Edge Serrations. AIAA Journal. 2009, 47(6): 1470-1481.
[42] Moreau, D. and Doolan, C.J. Tonal Noise from Trailing Edge Serrations at Low Reynolds Number. in 19th AIAA/CEAS Aeroacoustics Conference, Berlin, Germany, Paper No. AIAA-2013-2010. 2013,
[43] Arce León, C., Merino-Martínez, R., Ragni, D., et al. Boundary layer characterization and acoustic measurements of flow-aligned trailing edge serrations. Experiments in Fluids. 2016, 57(12): 182.
[44] Liu, X., Kamliya Jawahar, H., Azarpeyvand, M., et al. Aerodynamic Performance and Wake Development of Airfoils with Serrated Trailing-Edges. AIAA Journal. 2017, 55(11): 3669-3680.
[45] Talboys, E., Geyer, T.F. and Brücker, C. An aeroacoustic investigation into the effect of self-oscillating trailing edge flaplets. Journal of Fluids and Structures. 2019, 91:

102598.
[46] Gelot, M.B.R. and Kim, J.W. Effect of serrated trailing edges on aerofoil tonal noise. Journal of Fluid Mechanics. 2020, 904: A30.
[47] Celik, A., Mayer, Y.D. and Azarpeyvand, M. On the aeroacoustic characterization of a robust trailing-edge serration. Physics of Fluids. 2021, 33(7): 075120.
[48] Hasheminasab, S.M., Karimian, S.M.H., Noori, S., et al. Experimental investigation of the wake dynamics for a NACA0012 airfoil with a cut-in serrated trailing-edge. Physics of Fluids. 2021, 33(5): 055122.
[49] Shi, Y.J. and Kollmann, W. Wall-modeled large-eddy simulation of a trailing-edge serration–finlet configuration. AIP Advances. 2021, 11(6): 065222.
[50] Ffowcs Williams, J.E. and Hawkings, D.L. Theory relating to the noise of rotating machinery. Journal of Sound and Vibration. 1969, 10(1): 10-21.
[51] Ffowcs Williams, J.E. and Hawkings, D.L. Sound Generation by Turbulence and Surfaces in Arbitrary Motion. Philosophical Transactions of the Royal Society of London. Series A, Mathematical and Physical Sciences. 1969, 264(1151): 321-342.
[52] Zhao, M., Cao, H., Zhang, M., et al. Optimal design of aeroacoustic airfoils with owl-inspired trailing-edge serrations. Bioinspiration & Biomimetics. 2021, 16(5): 056004.
[53] Wang, L. and Liu, X.M. Aeroacoustic investigation of asymmetric oblique trailing-edge serrations enlighted by owl wings. Physics of Fluids. 2022, 34(1): 015113.
[54] Bae, Y. and Moon, Y.J. Effect of passive porous surface on the trailing-edge noise. Physics of Fluids. 2011, 23(12): 126101.
[55] Kisil, A. and Ayton, L.J. Aerodynamic noise from rigid trailing edges with finite porous extensions. Journal of Fluid Mechanics. 2018, 836: 117-144.
[56] Shi, Y. and Kollmann, W. Improved delayed detached eddy simulation of a porous wavy trailing edge. Physics of Fluids. 2021, 33(5): 055128.
[57] Teruna, C., Avallone, F., Ragni, D., et al. Numerical analysis of a 3-D printed porous trailing edge for broadband noise reduction. Journal of Fluid Mechanics. 2021, 926: A17.
[58] Turner, J.M. and Kim, J.W. Effect of spanwise domain size on direct numerical simulations of airfoil noise during flow separation and stall. Physics of Fluids. 2020, 32(6): 065103.
[59] Rao, C., Ikeda, T., Nakata, T., et al. Owl-inspired leading-edge serrations play a crucial role in aerodynamic force production and sound suppression. Bioinspiration & Biomimetics. 2017, 12(4): 046008.
[60] Rao, C. and Liu, H. Aerodynamic robustness in owl-inspired leading-edge serrations: a computational wind-gust model. Bioinspiration & Biomimetics. 2018, 13(5): 056002.
[61] Rao, C. and Liu, H. Effects of Reynolds Number and Distribution on Passive Flow

Control in Owl-Inspired Leading-Edge Serrations. Integrative and Comparative Biology. 2020, 60(5): 1135-1146.

[62] Geyer, T., Sarradj, E. and Fritzsche, C. Silent Owl Flight: Comparative Acoustic Wind Tunnel Measurements on Prepared Wings. Acta Acustica united with Acustica. 2013, 99(1): 139-153.

[63] Geyer, T.F., Claus, V.T., Hall, P.M., et al. Silent owl flight: The effect of the leading edge comb. International Journal of Aeroacoustics. 2017, 16(3): 115-134.

[64] Winzen, A., Roidl, B., Klän, S., et al. Particle-Image Velocimetry and Force Measurements of Leading-Edge Serrations on Owl-Based Wing Models. Journal of Bionic Engineering. 2014, 11(3): 423-438.

[65] Chaitanya, P., Joseph, P. and Ayton, L.J. Leading-Edge Profiles for the Reduction of Airfoil Interaction Noise. AIAA Journal. 2019, 58(3): 1118-1129.

[66] Huang, X. Theoretical model of acoustic scattering from a flat plate with serrations. Journal of Fluid Mechanics. 2017, 819: 228-257.

[67] Ayton, L.J. and Kim, J.W. An analytic solution for the noise generated by gust–aerofoil interaction for plates with serrated leading edges. Journal of Fluid Mechanics. 2018, 853: 515-536.

[68] Kamliya Jawahar, H., Showkat Ali, S.A. and Azarpeyvand, M. Serrated slat cusp for high-lift device noise reduction. Physics of Fluids. 2021, 33(1): 015107.

[69] Pérez-Torró, R. and Kim, J.W. A large-eddy simulation on a deep-stalled aerofoil with a wavy leading edge. Journal of Fluid Mechanics. 2017, 813: 23-52.

[70] Wang, Z. and Zhuang, M. Leading-edge serrations for performance improvement on a vertical-axis wind turbine at low tip-speed-ratios. Applied Energy. 2017, 208: 1184-1197.

[71] Ikeda, T., Ueda, T., Nakata, T., et al. Morphology Effects of Leading-edge Serrations on Aerodynamic Force Production: An Integrated Study Using PIV and Force Measurements. Journal of Bionic Engineering. 2018, 15(4): 661-672.

[72] Kim, J.W., Haeri, S. and Joseph, P.F. On the reduction of aerofoil–turbulence interaction noise associated with wavy leading edges. Journal of Fluid Mechanics. 2016, 792: 526-552.

[73] Turner, J.M. and Kim, J.W. Aeroacoustic source mechanisms of a wavy leading edge undergoing vortical disturbances. Journal of Fluid Mechanics. 2017, 811: 582-611.

[74] Muthuramalingam, M., Talboys, E., Wagner, H., et al. Flow turning effect and laminar control by the 3D curvature of leading edge serrations from owl wing. Bioinspiration & Biomimetics. 2020, 16(2): 026010.

[75] Wang, J., Ishibashi, K., Joto, M., et al. Aeroacoustic characteristics of owl-inspired blade designs in a mixed flow fan: effects of leading- and trailing-edge serrations. Bioinspiration & Biomimetics. 2021,

[76] Wang, J., Ishibashi, K., Ikeda, T., et al. Morphological effects of leading-edge serrations on the acoustic signatures of mixed flow fan. Physics of Fluids. 2022,

34(4): 041909.
[77] Gruber, M., Joseph, P., Polacsek, C., et al. Noise reduction using combined trailing edge and leading edge serrations in a tandem airfoil experiment. 18th AIAA/CEAS Aeroacoustics Conference (33rd AIAA Aeroacoustics Conference). 2012,
[78] Vemuri, S.H.S., Liu, X., Zang, B., et al. Leading-edge Serrations for Noise Control from Tandem Airfoil Configuration. 25th AIAA/CEAS Aeroacoustics Conference. 2019,
[79] Vemuri, S.S., Liu, X., Zang, B., et al. On the use of leading-edge serrations for noise control in a tandem airfoil configuration. Physics of Fluids. 2020, 32(7): 077102.
[80] Kopania, J. (2016). Acoustics Parameters the Wings of Various Species of Owls. In: *INTER-NOISE and NOISE-CON Congress and Conference Proceedings*: Institute of Noise Control Engineering) pp 7276-7284
[81] Klän, S., Bachmann, T., Klaas, M., et al. Experimental analysis of the flow field over a novel owl based airfoil. Experiments in Fluids. 2008, 46(5): 975-989.
[82] Ayton, L.J., Colbrook, M.J., Geyer, T.F., et al. Reducing aerofoil–turbulence interaction noise through chordwise-varying porosity. Journal of Fluid Mechanics. 2021, 906: A1.
[83] Showkat Ali, S.A., Azarpeyvand, M. and Ilário da Silva, C.R. Trailing-edge flow and noise control using porous treatments. Journal of Fluid Mechanics. 2018, 850: 83-119.
[84] Showkat Ali, S.A., Azarpeyvand, M., Szőke, M., et al. Boundary layer flow interaction with a permeable wall. Physics of Fluids. 2018, 30(8): 085111.
[85] Fink, M. and Bailey, D. Model tests of airframe noise reduction concepts. 6th Aeroacoustics Conference. 1980,
[86] Liu, X., Zhao, J. and Li, D. Noise reduction mechanism of single-arc bionic blade with wave shape leading edge coupled with serrated trailing edge. Hsi-An Chiao Tung Ta Hsueh/Journal of Xi'an Jiaotong University. 2015, 49: 1-10.
[87] Wang, M. and Liu, X. Numerical investigation of aerodynamic and acoustic characteristics of bionic airfoils inspired by bird wing. Proceedings of the Institution of Mechanical Engineers, Part G: Journal of Aerospace Engineering. 2018, 233(11): 4004-4016.
[88] Kong, D., Liang, A., Chu, J., et al. Study on Mechanism of Silent Flight of Owls. Applied Physics. 2015, 05(11): 137-146.
[89] Kondo, K., Aono, H., Nonomura, T., et al. (2013). Large-Eddy Simulations of Owl-Like Wing Under Low Reynolds Number Conditions. In: *ASME 2013 Fluids Engineering Division Summer Meeting*,
[90] Bachmann, T., Emmerlich, J., Baumgartner, W., et al. Flexural stiffness of feather shafts: geometry rules over material properties. The Journal of Experimental Biology. 2012, 215(3): 405-415.
[91] Winzen, A., Roidl, B. and Schröder, W. Particle-image velocimetry investigation of

the fluid-structure interaction mechanisms of a natural owl wing. Bioinspiration & Biomimetics. 2015, 10(5): 056009.

[92] Winzen, A., Roidl, B. and Schröder, W. Combined particle-image velocimetry and force analysis of the three-dimensional fluid–structure interaction of a natural owl wing. Bioinspiration & Biomimetics. 2016, 11(2): 026005.

[93] Afshari, A., Azarpeyvand, M., Dehghan, A.A., et al. Trailing-edge flow manipulation using streamwise finlets. Journal of Fluid Mechanics. 2019, 870: 617-650.

[94] Gao, R., Chen, K., Li, Y., et al. Investigation on aerodynamic performance of wind turbine blades coupled with airfoil and herringbone groove structure. Journal of Renewable and Sustainable Energy. 2021, 13(5): 053301.

[95] Bao, H., Song, B., Yang, W., et al. The function of the alula with different geometric parameters on the flapping wing. Physics of Fluids. 2021, 33(10): 101907.

[96] Kondo, K. Computational comparative study for design of low Reynolds number airfoil. 29th Congress of the International Council of the Aeronautical Sciences, ICAS 2014. 2014,

[97] Kondo, K., Aono, H., Nonomura, T., et al. Analysis of Owl-like Airfoil Aerodynamics at Low Reynolds Number Flow. Transactions of the Japan Society for Aeronautical and Space Sciences, Aerospace Technology Japan. 2014, 12(ists29): Tk_35-Tk_40.

[98] Aono, H., Kondo, K., Nonomura, T., et al. Aerodynamics of Owl-like Wing Model at Low Reynolds Numbers. Transactions of the Japan Society for Aeronautical and Space Sciences. 2020, 63(1): 8-17.

[99] Li, D. and Liu, X.M. Numerical study on aerodynamic performance and noise characteristic of several bionic airfoils. Journal of Engineering Thermophysics. 2015, 36: 2629-2632.

[100] Liu, X. and Liu, X. A Numerical Study of Aerodynamic Performance and Noise of a Bionic Airfoil Based on Owl Wing. Advances in Mechanical Engineering. 2015, 6

[101] Anyoji, M., Wakui, S., Hamada, D., et al. Experimental Study of Owl-Like Airfoil Aerodynamics at Low Reynolds Numbers. Journal of Flow Control, Measurement & Visualization. 2018, 06(03): 185-197.

[102] Liu, T., Kuykendoll, K., Rhew, R., et al. Avian Wing Geometry and Kinematics. AIAA Journal. 2006, 44(5): 954-963.

[103] Sunada, S., Sakaguchi, A. and Kawachi, K. Airfoil Section Characteristics at a Low Reynolds Number. Journal of Fluids Engineering. 1997, 119(1): 129-135.

[104] Sunada, S., Yasuda, T., Yasuda, K., et al. Comparison of Wing Characteristics at an Ultralow Reynolds Number. Journal of Aircraft. 2002, 39(2): 331-338.

[105] Nicoud, F. and Ducros, F. Subgrid-Scale Stress Modelling Based on the Square of the Velocity Gradient Tensor. Flow, Turbulence and Combustion. 1999, 62(3): 183-200.

[106] Lighthill, M.J. and Newman, M.H.A. On sound generated aerodynamically I. General theory. Proceedings of the Royal Society of London. Series A. Mathematical

and Physical Sciences. 1952, 211(1107): 564-587.
[107] Lighthill, M.J. On sound generated aerodynamically II. Turbulence as a source of sound. Proceedings of the Royal Society of London. Series A. Mathematical and Physical Sciences. 1954, 222(1148): 1-32.
[108] Curle, N. and Lighthill, M.J. The influence of solid boundaries upon aerodynamic sound. Proceedings of the Royal Society of London. Series A. Mathematical and Physical Sciences. 1955, 231(1187): 505-514.
[109] Garcia-Sagrado, A. and Hynes, T. Wall pressure sources near an airfoil trailing edge under turbulent boundary layers. Journal of Fluids and Structures. 2012, 30: 3-34.
[110] Yarusevych, S., Sullivan, P.E. and Kawall, J.G. Coherent structures in an airfoil boundary layer and wake at low Reynolds numbers. Physics of Fluids. 2006, 18(4): 044101.
[111] Liu, H. and Aono, H. Size effects on insect hovering aerodynamics: an integrated computational study. Bioinspiration & Biomimetics. 2009, 4(1): 015002.
[112] Rong, J. and Liu, H. Aeroacoustic interaction between owl-inspired trailing-edge fringes and leading-edge serrations. Physics of Fluids. 2022, 34(1): 011907.
[113] ANSYS Fluent: Theory Guide, Release 16.0, ANSYS, Inc., Canonsburg, PA.
[114]Lee, S., Ayton, L., Bertagnolio, F., et al. Turbulent boundary layer trailing-edge noise: Theory, computation, experiment, and application. Progress in Aerospace Sciences. 2021, 126: 100737.
[115] Courant, R., Friedrichs, K. and Lewy, H. On the Partial Difference Equations of Mathematical Physics. IBM Journal of Research and Development. 1967, 11(2): 215-234.
[116] Bachmann, T., Blazek, S., Erlinghagen, T., et al. (2012). *Nature-Inspired Fluid Mechanics: Results of the DFG Priority Programme 1207 "Nature-inspired Fluid Mechanics" 2006-2012,* ed C Tropea , & H Bleckmann (Berlin, Heidelberg: Springer Berlin Heidelberg) pp 101-117
[117] Wolf, T. and Konrath, R. Avian wing geometry and kinematics of a free-flying barn owl in flapping flight. Experiments in Fluids. 2015, 56(2): 28.